

# Politecnico di Torino

Facoltà di Ingegneria

Corso di Laurea Magistrale in Ingegneria Meccanica  
(Mechanical Engineering)

Sessione di laurea di Ottobre 2023



**Politecnico  
di Torino**

## **Numerical Study on Acoustic Phenomena in Cavities for Aero-engine Applications**

**Relatore:**

Dott. Steffen Hammer

Prof.ssa Daniela Misul

**Candidato:**

Gjoni Eglantin



*A mamma e a papà  
per non avermi mai  
tagliato le ali.*

*A mia sorella  
mia complice metà.*

*E a te  
tra duemila anni.*



# ABSTRACT

For about seventy years, noise generated by grazing flow past a cavity has been thoroughly studied. Yet, a coherent theory that describes such phenomena is missing. Lately, this phenomena started to be investigated in bleeding systems of aero-engines. The present work, within the CARE (Cavity Acoustics and Rossiter modEs) program, aims at identifying potential resonances and excitations which could lead to a failure of the components in the LPC (Low Pressure Compressor). Specifically, the purpose is to validate the experimental results derived at KTH Heat and Power Technology department. After a literature review and turbulence model study, the wind tunnel and the cavity are analyzed. Steady state simulations are carried concerning the wind tunnel, and different approaches are followed in order to match the numerical results with the experimental ones. Imposing a total pressure profile proved to be the most effective tool to match experimental data, nonetheless a more detailed analysis concerning the turbulence model is required. The velocity profile was then used for the 2D unsteady simulations, performed on the cavity section only. After defining the setup, simulations are carried over all the operating points, ranging from  $M = 0.3$  to  $M = 0.8$ . Although the use of a simplified model, a good agreement is found with the experimental results in terms of frequency. Matching the amplitude is still a difficult task, and is left as a future work, as well as 3D cavity simulations.





# Acknowledgements

I would like to start thanking my supervisor, Dr Steffen Hammer, for the advice and the direction provided in completing this work. A sincere thank you also to professor Jens Fridh, and to Dr Mattias Billson, from GKN Aerospace, for their insights and their valuable experience, without whom I probably wouldn't have made it. Thanks also to professor Misul, and her colleagues at PoliTo, for assisting me when I needed it.

Words only are not enough to thank the *terzo piano*, neither written nor spoken. The impact these years with you have had on me go beyond everyone's expectation, myself included. I'll keep it short: thanks for indirectly teaching me to be much more than I thought I could, to unveil a potential I never dared to imagine, and to dream a lot bigger than ever before. Without you, I wouldn't have been able to achieve none of the things I have achieved today, both from a professional and personal standpoint. I owe you everything, and I'll try my best to be there for you in the same way you have always been there for me. I promise. Thank you, to every single one.

A heartfelt thank you to all the people who have been with me during the wonderful year spent in Stockholm. Even though I was thousands kilometers away from home, you made me feel as if I was at home. The moments I spent with you bear profound meaning to me.

Thanks to all my colleagues, for showing patience with a stubborn like me. Together, we have dived the storms of exams, group projects and assignments, finding solace only in our shared struggles. See you at work, maybe in the future.

I would like to extend my gratitude also to all my friends from my hometown. Thank you for not forgetting me: although five years felt like an overwhelming flow of time, the string that wires our souls is as sharp as it has always been.

Lastly, thanks to my sister, Haidi, my mum, Bruna, and my father, Vullnet, whose love and support have accompanied me from the beginning to the end of this incredible journey.





# List of Tables

3.1	$\gamma = \gamma(L/D)$ . . . . .	33
6.1	Description of the relevant instruments. . . . .	57
6.2	Total temperature and pressure upstream the wind tunnel. . . . .	57
6.3	$c = c(M)$ . . . . .	58
6.4	Boundary conditions for the steady state analysis. . . . .	59
6.5	Mesh Details: part 1. . . . .	60
6.6	Mesh Details: part 2. . . . .	61
6.7	Mesh Details: part 3. Note that BL stands for <i>Bunching Law</i> . . . . .	62
6.8	Comparison between meshes- . . . . .	62
6.9	Comparison between turbulence models and experiments. . . . .	67
6.10	Comparison with previous PIV measurements [1]. . . . .	68
6.11	Boundary layer thickness $\delta_{99}$ at the measurement section as function of the inlet extension length $\Delta x_{in}$ . The operating conditions is $M = 0.5$ . . . . .	69
6.12	Boundary conditions for the steady state analysis of wind tunnel at $M = 0.3$ . . . . .	70
6.13	Boundary layer thickness $\delta_{99}$ at the measurement section as function of the outlet extension length $\Delta x_{out}$ . The operating conditions is $M = 0.5$ . . . . .	70
6.14	Comparison between simulations with different turbulence intensity at the inlet. . . . .	71
6.15	Boundary layer properties for different $\delta_{99,in}$ , with $M = 0.5$ . . . . .	73
7.1	Boundary conditions for the unsteady analysis. . . . .	77
7.2	2D Mesh Details: part 1. . . . .	80
7.3	2D Mesh Details: part 2. . . . .	81
7.4	General overview of the unsteady analysis. . . . .	82
7.5	Results of the mesh independence study: low frequency stands for the lower frequency mode measured by coarser meshes whereas high frequency stands for the higher frequency modes measured by refined meshes. . . . .	85
7.6	Comparing Numerical, Experimental and theoretical values for Rossiter mode. The coefficient $\kappa$ is 0.66. . . . .	86
7.7	Comparing different $\Delta t$ . Simulations were carried at $M = 0.7$ , with MESH-6-2D. The coefficient $\kappa$ is equal to 0.66. . . . .	89
7.8	Experimental data: frequency and amplitude for $M = 0.68$ , $M = 0.70$ and $M = 0.72$ . . . . .	89
7.9	Comparing different profiles at the inlet. Simulations were carried at $M = 0.5$ , with MESH-6-2D and $\Delta t = 1.0e - 5s$ . The coefficient $\kappa$ is equal to 0.57. . . . .	91
7.10	Experimental data: frequency and amplitude for $M = 0.549$ , $M = 0.497$ and $M = 0.451$ . . . . .	91
7.11	Results for different operating points, along with theoretical and experimental value (and relative errors). MESH-6-2D, $\Delta t = 1.0e - 5s$ , NORMAL profile and SST turbulence model. The coefficient $\kappa$ is equal to 0.57. . . . .	92
7.12	Comparison for $M = 0.6$ with higher order frequencies: Rossiter 1 # 3 indicates the third harmonics of the first Rossiter mode. . . . .	95

7.13	Comparing numerical and experimental results with the predicted value by Rossiter formula for different $\kappa$ . $\varepsilon_{num}$ stands for the relative error with respect to the numerical predicted frequency; $\varepsilon_{exp}$ stands for the relative error with respect to the measured experimental frequency. . . . .	95
7.14	All the measured frequencies (experimentally and numerically) for $M = 0.8$ . . . . .	95

# List of Figures

1.1	Real examples of cavities. . . . .	20
2.1	Schematic representation of fluid and body oscillators, with relative examples of discrete versus continuous systems. Reference for the picture:[2]. . . . .	22
2.2	Open-end interactions for discrete system (on the left) and continuous system (on the right). Reference for the picture: [2]. . . . .	23
2.3	Helmholtz resonator. Reference for the picture: [2]. . . . .	23
2.4	Helmholtz resonator: analogy with body oscillator. Reference for the picture:[3]. . . . .	23
2.5	1D standing wave patterns, for <b>closed/closed</b> , <b>open/open</b> and <b>open/closed</b> ends. Pressure variation is shown along the longitudinal coordinate $l$ (or $l_{eff}$ ). Reference for the picture:[2]. . . . .	24
2.6	Examples EIE, IIE and MIE for both fluid oscillators and body oscillators. Reference for the picture:[2]. . . . .	26
2.7	Vortex generation after a slight lateral perturbation (middle picture). Reference for the picture: [2]. . . . .	26
2.8	Effect of planar Reynolds number and Strouhal number of planar, anti-symmetric disturbances on initial amplification. Reference for the picture: [2]. . . . .	27
2.9	Overview of events during fluid-dynamic feedback. Reference for the picture: [2]. . . . .	27
2.10	(a) Phase condition for jet-flow, (b) mode switching phenomena. Reference for the picture: [2]. . . . .	28
2.11	Comparison of flow pictures and velocity spectra without (left, a) and with (right, b) the downstream impinging solid boundary. Reference for the picture: [2]. . . . .	29
2.12	Visualization of lock-in: note that a lock-in condition coincides exactly with a resonance condition for the fluid resonator. . . . .	30
3.1	Different examples of flow past cavities, categorized based on the dominating feedback. Reference for the picture: [4]. . . . .	31
3.2	Value of $b_{min}$ : $d$ indicates cavity depth, $\delta_0$ indicates the boundary layer layer thickness at separation, $Re$ indicates the Reynold number. The region above the experimental points indicates that fluid-dynamic oscillation can occur. Reference for the picture: [5]. . . . .	32
3.3	Geometrical dimensions of a rectangular cavity: $L$ and $D$ are respectively the cavity length and the cavity depth (in the third dimension, $W$ is defined as cavity width). . . . .	34
3.4	Pressure profile on the cavity floor for different $L/D$ . Reference for the picture: [6]. . . . .	34
3.5	Frequencies of period oscillations in cavities. On the left, shallow cavity; on the right, deep cavity. . . . .	35
3.6	$St = f(M)$ . Comparison between Rossiter's mode and depth-wise modes. Equation (3) in the figure indicates the modified Rossiter formula (equation 3.6), whereas equation (4) and (6) in the figure refer to the depth-wise resonance formula. Reference for the picture: [7]. . . . .	36
3.7	On the left, the Rossiter's formula is used to to fit the experimental results: for $0.4 < M < 1.2$ , equation 3.5 works fine (with $\gamma = 0.25$ and $\kappa_v = 0.57$ ). On the right, Tam & Block showed that for lower Mach ( $M < 0.4$ ) equation 3.5 (black line) doesn't properly represent the dataset. Reference for the picture: [8]. . . . .	36

3.8	PSD for different Mach numbers (geometry is fixed). Reference for the picture: [9]. . . . .	37
3.9	Roll-up of a free-shear layer. Reference for the picture:[10] . . . . .	38
3.10	From figure 3.10a to figure 3.10c, the PSD of acoustic measurements for laminar and turbulent layer; figure 3.10d shows intensity of the noise (of the peaks) for different $\delta_{99}$ . Reference for the pictures: [9]. . . . .	39
3.11	Comparison of the experimental results of Suhs [11] (refer to his work for details on geometry) and numerical simulations of Sadiq & Sabir [12]. Reference for the picture: [12]. . .	41
3.12	Shear layer mode: acoustic feedback occurs in this case. Reference for the picture: [13]. . .	42
3.13	Wake layer mode: a large vortex is shedded from the trailing edge, which will impinge on the leading edge causing vortex disruption with great mass ejection from the cavity. Reference for the picture: [13]. . . . .	43
3.14	Comparison of RANS vs LES vs DNS vs Rossiter's formula. Reference for the picture [13].	44
3.15	$\kappa_v$ coefficient over the cavity mouth. Reference for the picture: [14]. . . . .	44
4.1	Wind tunnel with cavity section. . . . .	45
4.2	Domain splitting for the steady and unsteady analysis. . . . .	46
4.3	The extrapolated velocity will be compared with the experimental measurements and then will be used as inlet boudnary condition for the cavity only. . . . .	47
4.4	Three-dimensional view of the cavity: $w$ is cavity width whereas $W$ is the wind tunnel width.	47
5.1	Graphical representation of the Reynolds decomposition. . . . .	50
5.2	Turbulent boundary layer structure. . . . .	53
5.3	Wall functions in a $\log_{10}(y^+) - u^+$ plane: the transition region for $5 < y^+ < 30$ is not properly covered by the two wall functions. Furthermore, the two laws happens to intersect at $y^+ \approx 11.06$ . Reference for the picture: [15]. . . . .	55
6.1	Wind tunnel used for steady analysis. Note that the dashed cavity is represented to state its position only, but in the simulations it is not considered. . . . .	56
6.2	Technical drawing of the front part of the wind tunnel with the cavity. . . . .	57
6.3	Corners flow prediction based on the turbulence model. Reference for the picture:[16]. . .	59
6.4	On the left, the outlet of MESH-1; on the middle, the outlet of MESH-2; on the right, the outlet of MESH-3. These three meshes represents the three different wall refinement that were adopted. . . . .	60
6.5	On the left, the stream-wise refinement of both MESH-1 and MESH-2; in the middle, the refinement of both MESH-3 and MESH-4; on the right, the stream-wise refinement of MESH-6.	61
6.6	Meshing parameters displayed in a simplified way. The square in the figure refers to the OUTLET. . . . .	62
6.7	Pressure at monitor point. . . . .	63
6.8	Total pressure profile: on the left, the overall profile with a small magnification close to the lower wall; on the right, a stretch is showed to highlight the stream-wise difference in free stream total pressure. . . . .	63
6.9	Velocity profile: on the left, the overall profile with a small magnification close to the lower wall; on the right, a stretch is showed to highlight the stream-wise difference in free stream velocity. . . . .	64
6.10	Comparison of numerical simulation with experimental results. On the left, the total pressure profile; on the right, a higher magnification. . . . .	64
6.11	From the left, velocity contour of $u$ , $v$ and $w$ . . . . .	65
6.12	Streamline in case of SST. . . . .	65
6.13	Streamline at the measurement section: from the top, $k - \varepsilon$ , RNG $k - \varepsilon$ and GEKO ( $C_{CORNER} = 1$ ). . . . .	66
6.14	Comparing turbulence models with experimental measurements (in terms of total pressure profile). . . . .	67
6.15	Inlet extension approach. . . . .	69
6.16	Magnification on the second contraction for $M = 0.3$ . . . . .	70
6.17	Outlet extension approach. . . . .	71

6.18	Comparison of total pressure profile for different cases of turbulence intensity. . . . .	71
6.19	Flow chart of the iterative procedure to follow in order to get the right boundary layer at the measurement section. . . . .	72
6.20	a) Total pressure at the inlet is constant b) Total pressure at the inlet follows a profile. . .	73
6.21	Expressing boundary layer properties as function of the inlet boundary layer thickness. . .	74
6.22	Contour plot of $v$ and $w$ component of velocity. Streamlines are overlapped. . . . .	75
7.1	Geometry of the 2D cavity section. . . . .	76
7.2	Schematic view of the boundary conditions. . . . .	77
7.3	Non-physical vorticity field at leading edge of the cavity due to non isotropic elements (aspect ratio $\sim 1$ ): the vortex roll-up is "compromised" by the error introduced by the mesh elements. . . . .	78
7.4	Different wavelengths according to the position: theoretical approach. . . . .	79
7.5	Different wavelengths according to the position: practical approach. . . . .	79
7.6	MESH-1-2D, MESH-5-2D and MESH-7-2D. . . . .	81
7.7	Monitor points location. . . . .	82
7.8	Time history of pressure at Monitor 2, for the different meshes, with $M = 0.4$ and $\Delta t = 1e - 5s$ . Only the first $30ms$ are displayed. The mean value has been subtracted from each set of data. . . . .	83
7.9	Comparing FFT with the transient phase and without it. . . . .	84
7.10	FFT for all the meshes. Details to compute the FFT are given in table 7.4. . . . .	85
7.11	Comparing coarse with fine mesh: the dashed rectangles aim at showing the difference in the dominant mode, the $\delta p$ aims at showing the difference in the average pressure amplitude. . . . .	86
7.12	Comparison of mesh independence study with Rossiter theoretical modes frequency and experiments. . . . .	87
7.13	Comparing FFT for different sampling frequency, at $M = 0.7$ . Monitor 2 is displayed. . .	89
7.14	Comparing the FFT when different velocity profiles are used. The operating condition is $M = 0.5$ and the time step that have been used is $\Delta t = 1e - 05s$ . . . . .	90
7.15	Mach3 - Vorticity contour . . . . .	93
7.16	Mach5 - Vorticity contour . . . . .	94
7.17	Some contours . . . . .	96
7.18	Some contours . . . . .	97
7.19	FFT for $M = 0.8$ : comparing the $2440Hz$ frequency with other models. . . . .	97
7.20	Real examples of cavities. . . . .	98
7.21	Comparison of experimental Strouhal number and numerical one: in black the experimental points and in magenta the numerical ones (square stands for dominant and triangle stays for secondary). . . . .	99
10.1	Pressure signal measured at the second monitor point. . . . .	104
10.2	On the left, pressure signal for Mach= 0.4 at monitor 2 position for the first 5'000 time-steps; on the right, the Fourier transform for the displayed signal. . . . .	105
10.3	On the left, pressure signal for Mach= 0.4 at monitor 2 position for 50'000 time-steps; on the right, the Fourier transform for the displayed signal (compared with the previous Fourier transform). . . . .	105

# Nomenclature

$\Delta p$	Pressure shift, used to refer to the shift between experiments and numerical results, in $Pa$
$\Delta t$	Time stepping, in $s$
$\Delta x$	Stream-wise spacing, in $m$
$\Delta x_{j,max}$	Maximum element spacing along $j$ direction
$\Delta y_1$ (or $\Delta y_{end}$ )	First (or last) element thickness along $y$ direction
$\Delta z_1$ (or $\Delta z_2$ )	First (or last) element thickness along $z$ direction
$\delta_2$	Displacement thickness, in $m$
$\delta_3$ (or $\theta$ )	Momentum thickness, in $m$
$\delta_{99}$	Boundary layer thickness, in $m$
$\epsilon$	Corrective fraction
$\gamma$	Empirical constant of Rossiter formula referring to <i>phase lag</i>
$\kappa_v$	Empirical constant of Rossiter formula referring to vortex-to-flow velocity ratio
$\lambda$	Wavelength, in $m$
$\mathbf{S}_M$	Specific volume forces, in $kg/m^3$
$\mu_t$	Turbulent viscosity, in $Pa^{-1}s^{-1}$
$\nu$	Dynamic viscosity, in $Pa \cdot s$
$\rho$	Density, in $kg/m^3$
$\tau_{ij}$ (or $\tau$ )	Stress tensor
$\epsilon$	Turbulent eddy dissipation, in $m^2/s^3$
$b_{min}$ or $L_{min}$	Minimum length required to have a Rossiter mode, in $m$
$c$	Speed of sound, in $m/s$
$f$	Frequency, in $Hz$
$f_D$	Disturbance frequency, in $Hz$
$f_o$	Dominant frequency, in $Hz$
$f_R$	Resonator's natural frequency, in $Hz$
$f_s$	Sampling frequency, in $Hz$
$h_{tot}$	Specific total enthalpy, in $J/kg$

$k$	Turbulent kinetic energy, in $m^2/s^2$
$l_{eff}$	Effective length due to open-end, in $m$
$M$	Mach number
$p$	Pressure (or static pressure), in $Pa$
$p^o$	Total pressure, in $Pa$
$p^o_\infty$	Free stream total pressure, in $Pa$
$R$	Gas constant for air, in $J/kgK$
$R_j$	Mesh stretch ratio along $j$ direction
$Re$	Reynolds number
$Re_D$	Reynolds number with respect to the cavity depth
$Re_L$	Reynolds number with respect to the cavity length
$Re_W$	Reynolds number with respect to the cavity width
$St$	Strouhal number
$T$	Static temperature, in $K$
$t$	Time, in $s$
$T^o$	Total temperature, in $K$
$u$	Velocity component along $x$ , referred also as stream-wise velocity, in $m/s$
$U_\infty$	Free stream velocity, in $m/s$
$v$	Velocity component along $y$ , in $m/s$
$V_c$	Convective velocity, or vortex velocity, in $m/s$
$w$	Velocity component along $w$ , in $m/s$
$y$	Height-wise direction
$y^+$	Non-dimensional distance from wall
$z$	Width-wise direction
CFL	Indicates the Courant-Friedrichs-Levi condition but is used (incorrectly) as Courant number
D	Cavity depth, in $m$
H	Shape factor
L	Cavity length, in $m$
L/D	Length-to-depth ratio
L/W	Length-to-width ratio
n (or N)	<b>Mode number</b>
W	Cavity width, in $m$

# Contents

<b>1</b>	<b>Introduction</b>	<b>18</b>
1.1	INTRODUCTION AND HISTORICAL NOTES . . . . .	18
1.2	STRUCTURE OF THE WORK AND OBJECTIVE . . . . .	19
<b>2</b>	<b>FLOW-INDUCED VIBRATIONS</b>	<b>21</b>
2.1	TYPES OF OSCILLATORS . . . . .	21
2.1.1	BODY OSCILLATORS . . . . .	21
2.1.2	FLUID OSCILLATORS . . . . .	21
2.2	SOURCES OF EXCITATION . . . . .	25
2.2.1	INSTABILITY-INDUCED EXCITATION (IEE) . . . . .	25
<b>3</b>	<b>CAVITY NOISE - A REVIEW</b>	<b>31</b>
3.1	SOUND FROM FLOW PAST CAVITIES . . . . .	31
3.2	PHYSICALLY SIGNIFICANT PARAMETERS . . . . .	33
3.2.1	GEOMETRICAL PARAMETERS . . . . .	33
3.2.2	MACH NUMBER . . . . .	35
3.2.3	BOUNDARY LAYER TYPE AND THICKNESS . . . . .	37
3.2.4	REYNOLDS NUMBER . . . . .	39
3.3	REVIEW ON NUMERICAL SIMULATIONS FOR CAVITY ACOUSTIC PROBLEM . . . . .	40
<b>4</b>	<b>METHODOLOGY</b>	<b>45</b>
<b>5</b>	<b>GOVERNING EQUATIONS, TURBULENCE MODELS AND CFD CONCEPTS</b>	<b>48</b>
5.1	INTRODUCTION . . . . .	48
5.2	NAVIER-STOKES EQUATIONS . . . . .	48
5.3	DIMENSIONLESS NUMBERS . . . . .	49
5.4	INTRODUCTION TO RANS TURBULENCE MODELS . . . . .	50
5.4.1	THE $k - \varepsilon$ TURBULENCE MODEL . . . . .	51
5.4.2	THE $k - \omega$ TURBULENCE MODEL . . . . .	51
5.4.3	THE SST TURBULENCE MODEL . . . . .	52
5.5	CFD CONCEPTS . . . . .	53
5.5.1	WALL-FUNCTIONS . . . . .	53
5.5.2	CFL CONDITION . . . . .	54
<b>6</b>	<b>STEADY STATE ANALYSIS</b>	<b>56</b>
6.1	INTRODUCTION . . . . .	56
6.2	PHYSICAL MODEL . . . . .	58
6.3	MESH INDEPENDENCE STUDY . . . . .	59
6.4	INFLUENCE OF THE TURBULENCE MODEL . . . . .	64
6.5	RESULTS AND DISCUSSION . . . . .	68
6.5.1	EXTENDED INLET APPROACH . . . . .	69
6.5.2	EXTENDED OUTLET APPROACH . . . . .	70
6.5.3	TURBULENCE INTENSITY APPROACH . . . . .	71
6.5.4	INLET PROFILE APPROACH . . . . .	72



<i>CONTENTS</i>	17
<b>7 UNSTEADY ANALYSIS ON A 2-DIMENSIONAL CAVITY</b>	<b>76</b>
7.1 INTRODUCTION . . . . .	76
7.2 PHYSICAL MODEL . . . . .	77
7.3 MESH INDEPENDENCE STUDY . . . . .	78
7.4 PARAMETERS AND SETUP . . . . .	88
7.4.1 TIME STEP INFLUENCE . . . . .	88
7.4.2 INLET PROFILE INFLUENCE . . . . .	90
7.5 RESULTS AND DISCUSSION . . . . .	92
7.6 CONCLUDING REMARKS . . . . .	99
<b>8 CONCLUSION</b>	<b>100</b>
<b>9 FUTURE WORK</b>	<b>101</b>
<b>10 APPENDIX A - SIGNAL ANALYSIS</b>	<b>103</b>
10.1 INTRODUCTION . . . . .	103
10.2 FOURIER ANALYSYS . . . . .	103

# Chapter 1

## Introduction

### 1.1 INTRODUCTION AND HISTORICAL NOTES

Over the past past seventy years, there has been significant interest in studying the noise produced by a flow passing a cavity due to its practical applications and theoretical implications. Coherent oscillations of the shear layer above the cavity are sustained by multiple complex feedback processes, resulting in significant radiated noise that includes both intense discrete and broadband components. Despite the relatively simple geometry that a cavity may assume, a multiplicity of complex phenomena occur all together. Those phenomena are the turbulent shear layer above the cavity, a complicated recirculation inside the cavity, turbulent boundary layers on the upstream and downstream walls, and long-wavelength acoustic fluctuations inside and outside the cavity. The theory of vortex sound has helped to clarify the interactions between acoustic and vortical modes in fluid dynamics. The difference of vortical modes, acoustic mode and their interaction will not be explained in this work. For deeper insights, see Chu & Kovsznay[17]. For the scope of this work, one should remember that vorticity in the flow, as occurs in the free shear layer, originates pressure waves at the downstream solid edge that will further excite the upstream layer.

Although lid-driven flows have been investigated for decades, focusing mainly on experimental validation of numerical scheme and influence of Reynolds number of flow pattern, research on cavity flow began in the 1940s with military companies commissioning experimental studies concerning flow over weapon bays (figure 1.1a). The main focus of the research was to understand the mechanisms that drive the flow in a weapons bay, particularly at high subsonic and supersonic speeds where deployment of stores can be difficult due to the harsh cavity environment. This can cause problems such as ejection of stores through turbulent air or damage to stores and surrounding structures due to high intensity acoustic noise. To overcome these issues, flow control devices were implemented to make the cavity environment more suitable for internal store carriage and release. This research is not exclusive to the military, as the automotive industry also studies cavity flows to reduce drag and noise in relation to sunroofs and open windows cavities (1.1d). The scope of application is expanded to include high-intensity oscillations that arise in resonant systems under grazing flow. These resonant cavities come in various shapes and forms, such as the different stages of a compressor or combustion chamber, T-junctions or closed side-branches in duct networks, excavations in air or general piping for gas transport, or steam circuits in power plants (figure 1.1c). The reason to study the acoustics behind the cavities are different depending on the field: in case of aircraft applications, cavities would represent 30% of the total drag; for ground transportation, acoustic comfort is the driving reason; for industrial application, instability in the flow in pipelines could resonate with the piping system itself, and pressure fluctuations might induce cavitation (steam circuits).

Lately, still in the aeronautics field, another application where cavity acoustics phenomena is relevant has started to receive some attention: the bleeding system of aircraft engine. Aleksentsev *et al.* [18] firstly analyzed the topic. Bleed channels are cavities located in the gas-turbine engine core and fan ducts. This application is also the driving reason of this whole work: within the CARE (Cavity Acoustics and Rossiter modEs) project, funded by **Vinnova**, in collaboration with **GKN Aerospace**, cavity acoustic phenomena is analyzed to provide with a better understanding on resonances and excitation that might arise from

this and eventually leading to a failure of the components in the Low Pressure Compressor (LPC) (see [19]).

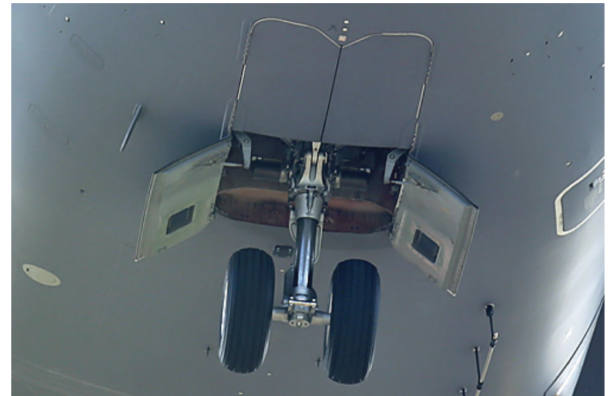
## 1.2 STRUCTURE OF THE WORK AND OBJECTIVE

This work presents a puzzle piece in the overall CARE project. The scope of the whole project is the investigation of cavity acoustics phenomena contextualized in the case of the bleeding system of an LPC. The driving reason is to push the design limits further in order to achieve a more efficient design (for instance, by improving fatigue design of compressors blade), and this is done by the reduction of the uncertainty around the estimation of the resonance points that might arise from radiated noise. In order to do so, the research needs to be move gradually from basic understanding of the phenomena supported by experiments on simplified cavities. At KTH Heat and Power Technology labs, a wind tunnel has been installed with a test section containing a symmetric cavity. Details on the experimental setup are shown in the following chapters and in the work of Hammer *et al* in [24]. Measurements have been done on a rectangular cavity with different depths: the scope of the overall research at KTH is to investigate the so-called Rossiter's mode in the low to high subsonic range ( $0.3 < M < 0.8$ ) which has not been widely discussed in the literature. The scope of this work is to validate these experimental results by means of ANSYS CFX. An effort will be done in order to establish a general framework for validation of experimental results on cavity acoustics. Turbulence models, mesh convergence study and post-processing techniques are discussed. All that in order to provide with a clear methodology for future works.

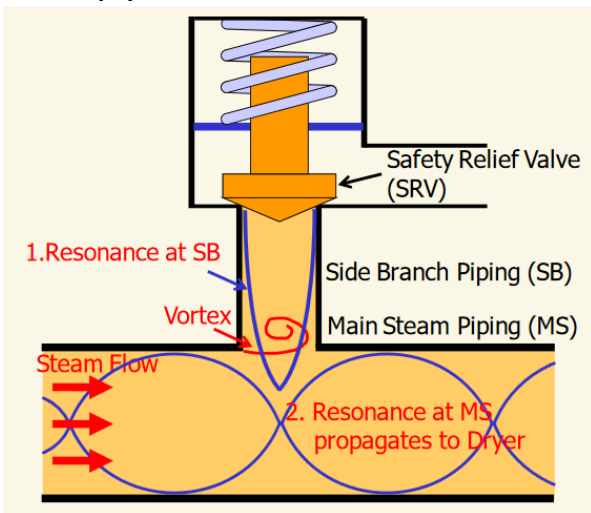
For this scope, the work is structured in several chapters. A part from the introduction, a literature review chapter is be presented in order to give a general overview on the topic, including current state-of-art and limitations. Numerical methods are also discussed, as they represent a starting point for the performed simulations. A methodology chapter will explain the approach and the procedure followed. The results and the discussion are divided in two parts: steady vs unsteady. Each part is presented and the results of each part are motivated. Finally, the conclusion and the future work is shown.



(a) Bomb bays of military aircraft. Reference for the picture: [20].



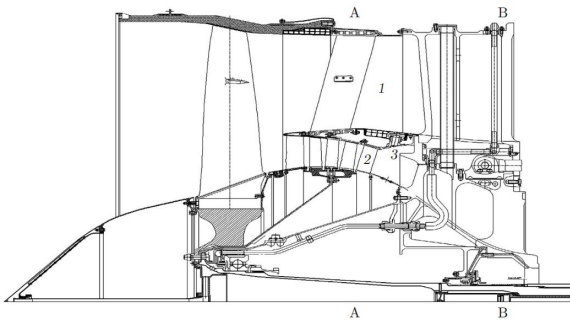
(b) Landing gear store. Reference for the picture: [21]



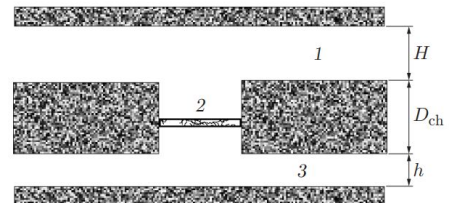
(c) Branches of steam-piping system. Reference for the picture: [22].



(d) Car's window as a cavity. Reference for the picture: [23].



(e) LPC of PS-90A engine: (1) fan duct; (2) core duct; (3) bleed channel in the middle. Reference for the picture: [18].



(f) Bleed channel in axial-radial coordinates. Reference for the picture: [18].

Figure 1.1: Examples of cavity in real life applications.

## Chapter 2

# FLOW-INDUCED VIBRATIONS

In the following chapter, an overview on flow-induced vibration is given: the fundamentals are discussed and concept as fluid oscillator are described. This chapter provides the basic knowledge required to understand the phenomena of flow past a cavity. Main references are [2, 25], to which one should resort for further and deeper insights.

### 2.1 TYPES OF OSCILLATORS

Oscillators, for the scope of this work, are every system of structures or fluids that undergo vibrations when subjected to external forces or excitations, which will move such systems away from their equilibrium position. Engineering systems possess several oscillators and several sources of excitations. Two main types of oscillators can be distinguished in turbomachines:

1. Body (*solid*) oscillators;
2. Fluid oscillators.

Another classification of these oscillators is *discrete* and *continuous* oscillators. Fluid oscillators (as well as body oscillators) can either be discrete or continuous.

#### 2.1.1 BODY OSCILLATORS

With body oscillators one refers to a system of structures, or a single structure, that can perform linear or angular movements, when excited by an external force. These structures can either be modelled as *lumped* masses, where each point of the structure displaces of the same quantity  $y$ , or as continuous systems, where each point displaces of a quantity  $y$  which is function of the position  $x$  that is being considered along the body (i.e.  $y$  refers to oscillations along  $y$  directions whereas  $x$  refers to the position along the body). Figure 2.1 (a) shows a simply lumped body oscillator, whereas figure 2.1 (b) shows a discrete body oscillator.

Acoustic waves are generated by the shear layer impingement past a cavity. Such waves can travel upstream, all the way back to compressor stages, where blades are thin, inducing an excitation into these components. The blade represents the body oscillator when its natural frequency is matched by the acoustic frequency.

#### 2.1.2 FLUID OSCILLATORS

As for the body oscillator, also fluid oscillators can be distinguished as:

1. Discrete-mass systems;
2. Distributed-mass system.

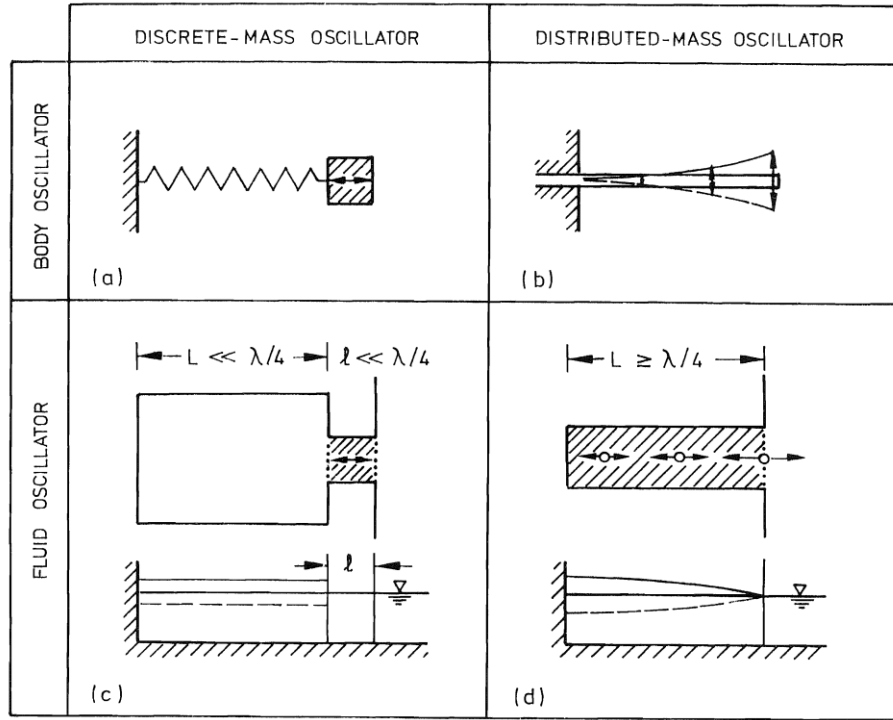


Figure 2.1: Schematic representation of fluid and body oscillators, with relative examples of discrete versus continuous systems. Reference for the picture:[2].

In discrete-mass systems ("lumped" fluid oscillators) a well defined mass of fluid oscillate in a rigid-body manner. The most famous one is the Helmholtz resonator in compressible systems: other systems can represent discrete fluid oscillator, but its not the scope of this work to go through all of them (see ref. [2]).

In distributed-mass systems, all the elements of the fluid do not oscillate as a rigid body, but each of them has its own displacement depending on the position (and on the time as well).

The distinction between discrete and continuous fluid oscillators, according to [2], can be done based on the *wavelength*  $\lambda$  of the corresponding excitation. By calling with  $c$  the *wave celerity* (speed of sound) and with  $f$  the frequency of excitation, the wavelength is defined as follows:

$$\lambda = \frac{c}{f} \quad (2.1)$$

Now, given also the largest dimension  $L$  of the body of the fluid, one can say that:

- If  $L \ll \lambda/4$ , a so-called **pumping mode** of fluid oscillation is possible;
- If  $L \geq \lambda/4$ , fluid particles no longer move in a rigid-body fashion, and formation of **standing wave** is possible.

Let's precise that in both cases, discrete and continuous, the mass oscillation does not terminate at the open ends: fluid outside these end sections takes part in the oscillation, and their effect is to introduce a dissipative action, as well as changing the frequency of excitation. Figure 2.2 shows an example of such interaction. In the literature, the effect open-end effect is considered by using a new length  $l_{eff}$  instead of  $L$ . The scope of this  $l_{eff}$  (*effective length*) is consider an extra portion of fluid at the open-ends for a more accurate estimation of the resonance-frequency of the system.

Some examples of both discrete- and continuous-mass fluid oscillators are now shown: the purpose is just to discuss some of their feature, such as frequencies and oscillating behaviour, as it will come handy when discussing the cavity case.

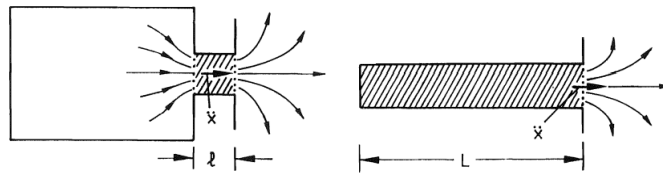


Figure 2.2: Open-end interactions for discrete system (on the left) and continuous system (on the right). Reference for the picture: [2].

**DISCRETE-MASS FLUID OSCILLATOR: HELMHOLTZ RESONATOR**

In figure 2.3 an example of a Helmholtz resonator is given. It consists of a **cavity** of length  $l$ , volume

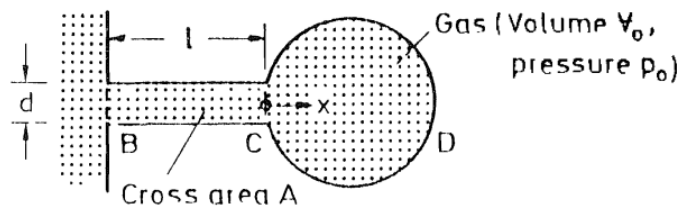


Figure 2.3: Helmholtz resonator. Reference for the picture: [2].

$V_{cavity}$  ( $V_{cavity}$  is the volume of the cavity, from point B to C) and cross section  $A_{cavity}$  linking an enclosed volume of air (indicated in figure 2.3) with gas) to the outside environment. The Helmholtz resonator that is most commonly known is the empty bottle, where a sound is produced by blowing over the top of it. A significant characteristic of such resonators is their ability to soak up acoustic energy at their resonant frequency.

It's important to understand that in the Helmholtz resonator, it's only the fluid within the cavity that is oscillating: there is an open-end fluid interaction (as depicted in figure 2.2). To have a more accurate prediction of this frequency, the  $l_{eff}$  is introduced, and is defined as:

$$l_{eff} = l + 2l' \tag{2.2}$$

In the literature can be found different ways of expressing  $l'$ : [2]. The resonant frequency of the Helmholtz resonator is expressed by equation 2.3:

$$f_R = \frac{c}{2\pi} \sqrt{\frac{A_{cavity}}{l_{eff} V_{cavity}}} \tag{2.3}$$

The analogy with the body oscillator is given by figure 2.4, where it is clear that the air enclosed in the cavity represents the lumped mass whereas the air enclosed in the bottle acts as a spring.

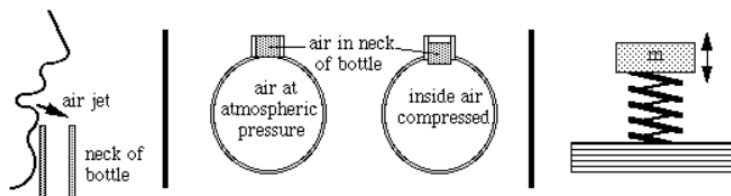


Figure 2.4: Helmholtz resonator: analogy with body oscillator. Reference for the picture:[3].

### DISTRIBUTED-MASS FLUID OSCILLATOR: HALF- AND QUARTER-WAVELENGTH

In distributed systems, this oscillation is the result of multiple wave trains, where one originates from a disturbance or excitation point and others reflect from the surrounding boundaries. As the waves move through the fluid, the fluid particles are cyclically displaced from their resting positions, causing periodic changes in fluid pressure. Note that:

- At a rigid boundary, the velocity normal to the wall is zero, and a wave is positively reflected;
- At an open end, the pressure must remain approximately equal to the outside pressure, and the wave is negatively reflected.

At the end, standing waves occur as a result of waves reflecting back on themselves. Figure 2.5 gives examples of standing waves patterns.

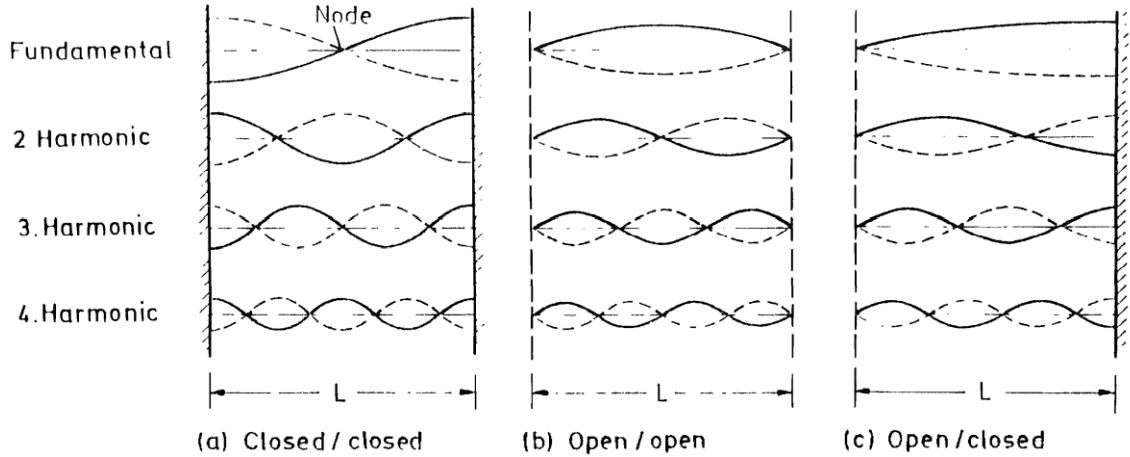


Figure 2.5: 1D standing wave patterns, for closed/closed, open/open and open/closed ends. Pressure variation is shown along the longitudinal coordinate  $l$  (or  $l_{eff}$ ). Reference for the picture:[2].

These standing waves will oscillate at their own resonance frequency. Using an improper terminology (not used in [2], but specifically designed for this manuscript in order to make things easier), the fluid oscillator that results from closed/closed ends and open/open ends will be defined as half-wavelength resonator. The main idea is that between these two types of ends, only an integer-number multiple of  $\lambda/2$  can exist. The wavelength at resonance for the half-wavelength resonator is:

$$\lambda_R = \frac{2l_{eff}}{N}, \quad N = 1, 2, 3, \dots \quad (2.4)$$

In case of open/closed ends, one has the quarter-wavelength resonator, whose resonant wavelength is given by:

$$\lambda_R = \frac{4l_{eff}}{2N-1}, \quad N = 1, 2, 3, \dots \quad (2.5)$$

Note that these are these wavelengths  $R$  describe the modes of oscillation of the fluid in one dimension: for a more deeper insight on 2D or 3D standing waves, refer to [2].



## 2.2 SOURCES OF EXCITATION

Provided a basic theoretical framework on different types of oscillator, it is important to examine the various sources of excitation that could potentially interact with them. Three types of oscillators are hereafter cited:

1. Extraneously induced excitation (EIE);
2. Instability-induced excitation (IIE);
3. Movement-induced excitation (MIE).

In *extraneously induced excitation* (EIE), the exciting force is mostly random (but one may find also some periodic ones). An example is a structure being excited by vortices shed upstream by a cylindrical structure, for instance at a certain frequency.

*Instability-induced excitation* (IIE) is due to flow instability. Differently from the other two, this is an **intrinsic property** of the analyzed system: the instability of the flow is an inherent characteristic of the flow generated by the considered structure. An example is the vortex shedding from a cylinder, or the oscillations of the shear layer past a cavity, which is exactly the case that will be discussed in this work. An important aspect of these instability-induced vibrations is the type of control exerted on the flow. This control can be:

- fluid-dynamic;
- fluid-elastic;
- fluid-resonant.

In the fluid-resonant case, relevant to the scope of this work, the excitation depends on flow and fluid-oscillator. The main feature of this control is the **amplification** of the exciting force and the establishment of "locked-in" condition, in which the exciting frequency tunes with the resonator.

*Movement-induced excitation* (MIE) is caused by fluctuating forces that result from the movements of a vibrating body or fluid oscillator. This means that the oscillations of the oscillator are self-generated. Figure 2.6 shows examples of these excitations.

The focus will hereafter move to the IIE types of excitations, since they represent the main type of excitation concerning cavities.

### 2.2.1 INSTABILITY-INDUCED EXCITATION (IIE)

As stated, the IIE are an intrinsic property of the system: due to the flow and the geometry, such excitations will always arise. Depending on the control or amplification mechanism, the excitations may focus around a specific frequency, called the **dominant frequency**  $f_o$ : the design problem is then to avoid a tuning of the resonant frequency  $f_R$  of the fluid oscillators (the main type of oscillators that are discussed in this work) with the dominant frequency  $f_o$  of excitation. Despite its apparent unlikelihood, a lock-in scenario can in fact arise: the interaction with the fluid oscillator causes an amplification of the exciting force as well as the **locking-in**, for which  $f_o = f_R$ . Interactions with non-oscillating part can also occur (stiffness approaching infinity). Depending on the type of interaction, between the flow instability and the resonator, different amplification mechanisms can occur.

By amplification mechanism one refers to the way in which instabilities are amplified. A slight lateral disturbance on a flow field will modify velocity and pressure. According to the Bernoulli theorem, this change then causes further modification to the streamline pattern in the direction of the initial perturbation. As the disturbance is amplified, it becomes asymmetric due to the mean-velocity distribution and eventually forms a concentrated region of vorticity. In a viscous fluid, this process, known as shear-layer roll-up, is either damped or leads to the formation of discrete and gradually decaying vortices or eddies. This is represented in figure 2.7.

It is important to highlight that the flow instability starts an energy-transfer from the flow to the disturbance. The success of the initial energy transfer from the mean flow to flow disturbances is influenced by factors such as geometry and flow parameters, as well as the frequency of the disturbances  $f_D$ .  $f_D$

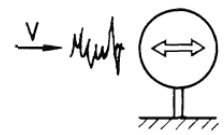


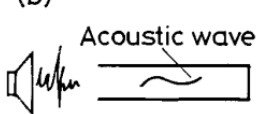

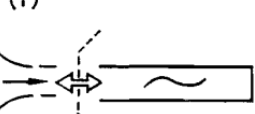
	EIE	IIE	MIE
BODY OSCILLATOR	(a)  Turbulence buffeting	(c)  Vortex shedding	(e)  Flutter
FLUID OSCILLATOR	(b)  Noise (from loudspeaker)	(d)  Impinging shear layer	(f)  Oscillating shock front

Figure 2.6: Examples EIE, IIE and MIE for both fluid oscillators and body oscillators. Reference for the picture: [2].

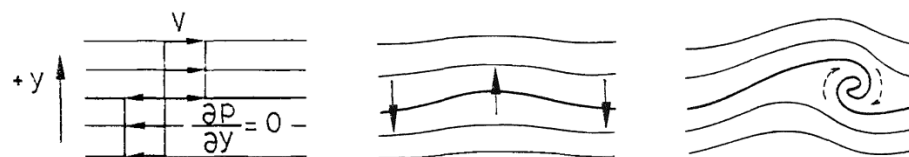


Figure 2.7: Vortex generation after a slight lateral perturbation (middle picture). Reference for the picture: [2].

represents the disturbance frequency, which is the frequency at which disturbances occur, or frequency at which disturbances are introduced into the flow.  $f_o$ , instead, is the dominant frequency, and refers to the frequency component of the flow instability that has the largest amplitude or energy, and therefore has the most influence on the behavior of the flow. All of them must be differentiated from the oscillator resonance frequency  $f_R$ , that is the frequency of resonance of the fluid (or body).

According to the **selective amplification** theory proposed by Naudascher [26], above critical flow speeds, only disturbances with  $f_D$  that falls within a certain range will be amplified: figure 2.8 shows an example of a *stability diagram* of the shear layer coming from a jet. Random excitations, coming from the environment for instance (EIE), might be amplified if within the range instability thus inducing a periodic flow oscillations. This inclination towards periodicity is not very strong unless it is reinforced by other control mechanisms in the system. One way to enhance periodicity is through fluid-dynamic feedback from a downstream edge of impingement. To originate a self-sustained instability within the flow, a feedback loop is therefore required.

Different feedback loops have been investigated in the literature ([2]). For the scope of this work, two self sustained amplification mechanism are analyzed:

1. Fluid-dynamic feedback;
2. Fluid-resonant feedback.

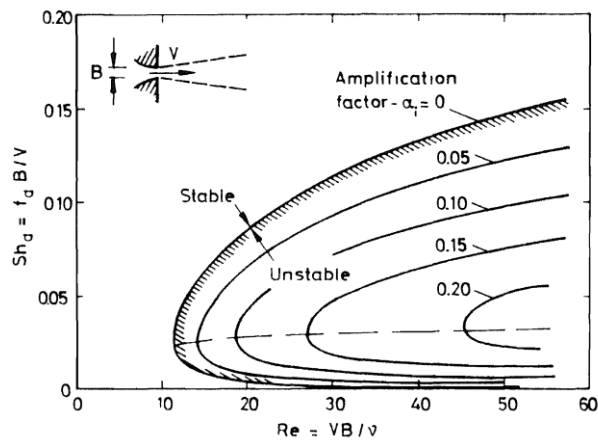


Figure 2.8: Effect of planar Reynolds number and Strouhal number of planar, anti-symmetric disturbances on initial amplification. Reference for the picture: [2].

**FLUID-DYNAMIC FEEDBACK**

When a flow comes into contact with a solid boundary or obstacle downstream, the pressure perturbations that are fed back upstream are generally much stronger than those produced by natural feedback: by acting on the origin of these flow instabilities, new flow fluctuations are triggered that are later amplified. This process, eventually, will reach a self-sustaining condition. Figure 2.9 shows schematically a sketch on how the initial flow instability (occurring at I) is interacting with the downstream solid boundary (II), creating pressure waves that travel upstream (feedback of pressure perturbations).

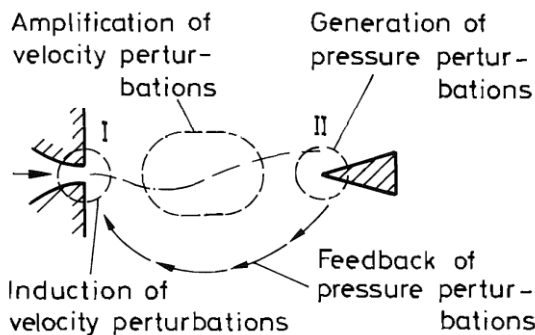


Figure 2.9: Overview of events during fluid-dynamic feedback. Reference for the picture: [2].

In order for self-sustainment to be achieved, *amplification condition* (shown in figure 2.8) and *phase condition* must hold. Given the case in figure 2.9, the phase condition imposes that the disturbances that are generated at I and are impinging at II are in phase with the pressure feedback that is generated at II and travels at I. If this condition is respected, then the dominant frequency of oscillation of the flow is given by:

$$f_o = (n + \epsilon) \frac{V_c}{L} \tag{2.6}$$

Where:  $n$  is the mode number,  $\epsilon$  is a corrective fraction ( $0 < \epsilon < 1/2$ ),  $V_c$  the convective velocity at which the perturbation is transported downstream (different from flow speed) and  $L$  the distance between jet and solid boundary. Figure 2.10 shows a schematic sketch. Still in figure 2.10, the mode switching is presented. *Mode switching* refers to a phenomenon in which the dominant frequency of a flow instability changes abruptly in response to a change in flow conditions, such as a change in the Reynolds number or the geometry of the flow. Generally, when a fluid flow becomes unstable, it typically develops into a pattern of oscillations at a characteristic frequency, the dominant frequency  $f_o$ . As the flow conditions

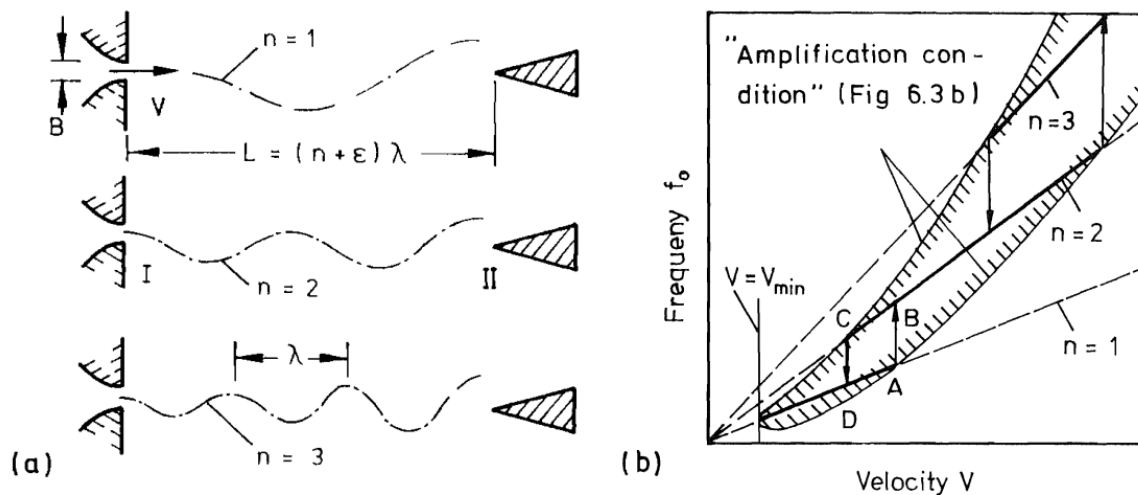


Figure 2.10: (a) Phase condition for jet-flow, (b) mode switching phenomena. Reference for the picture: [2].

change, such as the velocity or the geometry of the flow, the natural frequency of the instability may change as well. In some cases, the natural frequency may jump from one mode to another as the flow conditions pass through a critical value, resulting in a mode switch. In the case shown in figure 2.10, when velocity  $V$  surpasses point A, the flow becomes too stable to sustain first-mode oscillations. Meanwhile, the growth rate for the next possible mode increases, making it more likely that the system will transition to that mode. This is strictly related to the selective amplification: only instabilities corresponding to the second mode will now be amplified.

Figure 2.11 shows examples of two PSD (Power Spectral Density), with and without the fluid-dynamic feedback loop. The case with the feedback loop shows clearly the concept of selective amplification of certain frequencies. This is contextualized in the case of cavity acoustics, where the fluid-dynamic feedback is due to the **impinging shear layer**. The impinging shear layer theory represents, together with the fluid-resonator feedback, the major contributor of the shear layer oscillation. According to [27], in order to achieve a self-sustaining oscillations due to an unstable impinging shear layer, a chain of four events must occur:

1. Impingement of organized vorticity fluctuations upon the downstream solid edge;
2. Upstream influence due to pressure waves generated at the downstream edge;
3. Energy transfer from upstream influence to velocity fluctuations in the unstable shear layer;
4. Selective amplification of disturbances.

This chain of events has already been shown in figure 2.7. For more insights on the different mechanisms, see [27].

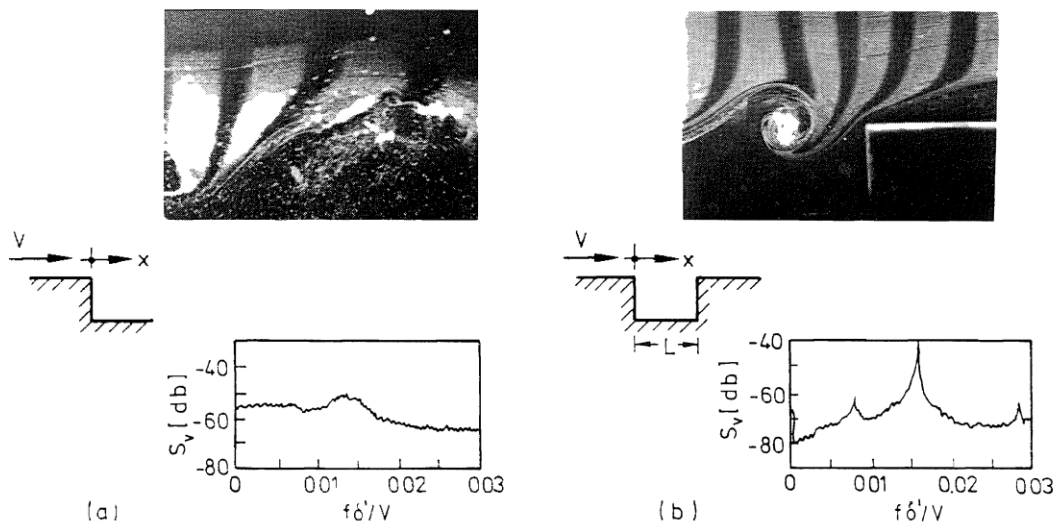


Figure 2.11: Comparison of flow pictures and velocity spectra without (left, a) and with (right, b) the downstream impinging solid boundary. Reference for the picture: [2].

### FLUID-RESONANT FEEDBACK

The feedback system can also be associated with a fluid-resonator. If one considers the cavity of figure 2.11, and neglects the pure fluid-dynamic feedback associated with upstream-travelling pressure waves, then the flow field resulting from the interaction between the shear layer and impingement edge may be governed by the fluid within the cavity that acts as a resonator. The fluid in the cavity shown in figure 2.11 can be interpreted as distributed-mass oscillator, therefore half- and quarter-wavelengths formula can be used. In the literature [28] it has been shown that the presence of either a longitudinal mode (along the length of the cavity) or transversal mode (along the depth of the cavity) occurs depending on the **Length/Width** ratio.

For fluid-resonant feedback, lock-in condition can also occur. Lock-in occurs when the natural frequency of flow oscillations becomes synchronized with the natural frequency of the resonator, resulting in a positive feedback loop that amplifies the oscillations. Mode switching can occur when the natural frequency of the flow instability shifts due to changes in flow conditions such as changes in the velocity or geometry of the flow. If the frequency of the flow oscillation moves away from the resonator's natural frequency, then the lock-in condition may be broken, leading to a decrease in the amplitude of the oscillations. However, if the frequency of the flow instability moves closer to another natural frequency of the resonator, then lock-in can occur again, leading to a new positive feedback loop and amplification of the oscillations at the new frequency. This can further trigger mode switching as the frequency of the flow instability continues to shift, and the resonator responds accordingly. The interplay between lock-in and mode switching can lead to unpredictable and complex behavior in fluid-resonator systems. Figure 2.12 shows how this lock-in is achieved.

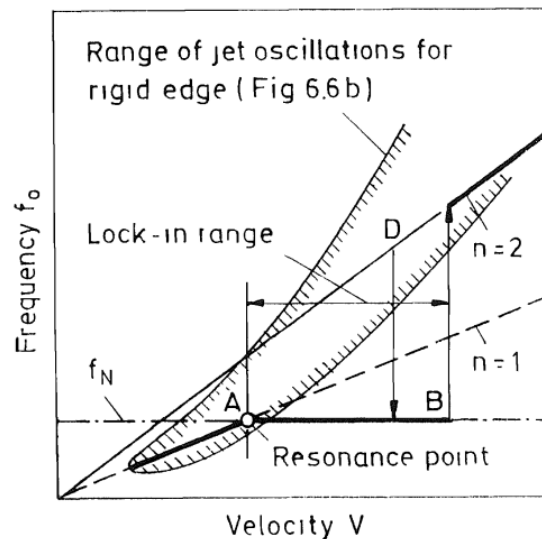


Figure 2.12: Visualization of lock-in: note that a lock-in condition coincides exactly with a resonance condition for the fluid resonator.

# Chapter 3

## CAVITY NOISE - A REVIEW

### 3.1 SOUND FROM FLOW PAST CAVITIES

The presence of a flow past a cavity leads to the emergence of acoustic tones at the natural frequencies of the cavity. These tones are triggered by the unstable shear layer located over the opening of the cavity and can be detected in both subsonic and supersonic flow scenarios, regardless of whether the cavity opening is parallel or perpendicular to the flow direction [29]. Rockwell & Naudascher [4], more than forty years ago, have gone through an extensive review of this phenomena. In their work, which represents one of the main references still today, the authors collected a long series of studies on flow past cavities with different geometrical configurations. Some of them are resumed in figure 3.1. The terminology indicated

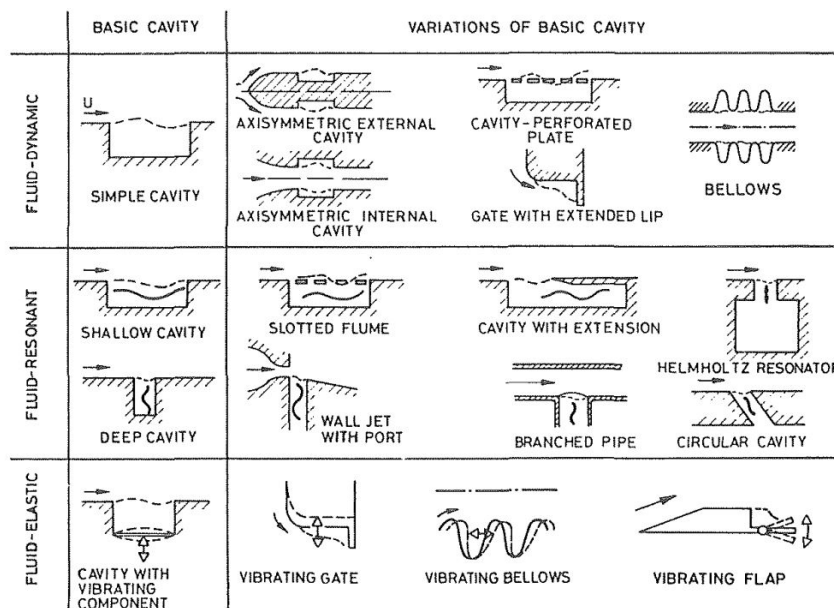


Figure 3.1: Different examples of flow past cavities, categorized based on the dominating feedback. Reference for the picture: [4].

in the figure is the same adopted in Naudascher's book [2], which has been discussed in the previous chapter. By recalling some of the concepts, self-sustaining oscillation are categorized in:

1. Fluid-dynamic (feedback);
2. Fluid-resonant (feedback);
3. Fluid-elastic (feedback).

The last one (fluid-elastic type) hasn't really been discussed: it occurs whenever the flow oscillations are coupled with the motion of solid boundaries, which is not really the case of this work (were cavity can be considered infinitely stiff).

Despite the different geometries that are presented, Rockwell & Naudascher noticed that a general framework to describe cavity noise can be established.

In practice, for a cavity, a combination of fluid-dynamic and fluid-resonant feedback occurs.

A **fluid-dynamic only** type of oscillation occurs when the ratio  $L/\lambda$ , where  $L$  is the cavity length and  $\lambda$  the acoustic wave-length, is very small ( $L \ll \lambda$ ). Selective amplification allows certain disturbances, at a certain frequency  $f_o$ , to be amplified more than others. This, coupled with the feedback of the upstream pressures, allows the shear layer to oscillate in a self-sustained way. Sarohia [5] noted that, even if the ratio  $L/\lambda$  was very small, these fluid-dynamic oscillations will not always occur. A minimum cavity length needed to be defined (according to his manuscript  $b_{min}$ ) so that for cavity lengths higher than the minimum value oscillatory behaviour could be spotted. Figure 3.2 shows the experimental results from which Sarohia derived the  $b_{min}$  (according to his notation,  $b$  indicates the cavity length). The excitation

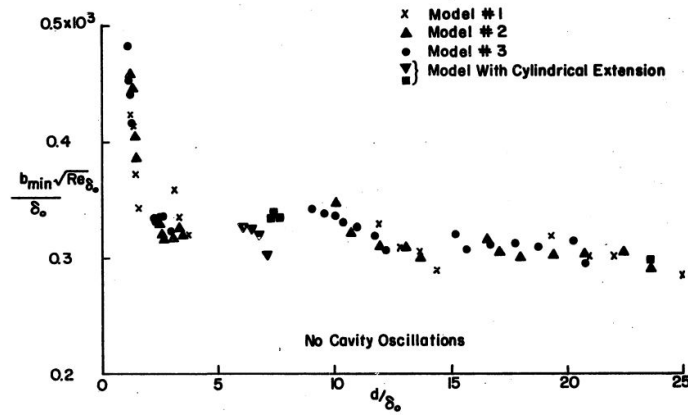


Figure 3.2: Value of  $b_{min}$ :  $d$  indicates cavity depth,  $\delta_0$  indicates the boundary layer thickness at separation,  $Re$  indicates the Reynolds number. The region above the experimental points indicates that fluid-dynamic oscillation can occur. Reference for the picture: [5].

in this case is given by the impinging shear layer at the downstream leading edge, occurring at frequency  $f_o$ . The analytical model to derive this frequency of excitation for cavities has been initially studied by Plumbee *et al* (summarized by [30]). When a vortex is shed near the upstream corner of the cavity and moves with the flow to hit the downstream corner, it creates a change in local pressure as per the Bernoulli principle. This change in pressure generates a pressure wave with the same frequency as the vortex shedding. This pressure wave propagates in all directions, including the upstream direction, thus the corner of the cavity. The model assumes that the excitation frequency is the one that meets the resonant conditions (or phase conditions, cited in the previous chapter), namely:

$$\Phi = (\phi_v - \phi_p)_{x=0} = 2\pi N \quad (3.1)$$

where  $v$  and  $p$  refer respectively to vortex and pressure, meaning that the phase difference between the generation of a vortex and the upstream pressure interacting at the upstream corner ( $x = 0$ ) is an integer multiple of  $2\pi$ , where  $N$  indicates the mode. Using the definition of wave-length, the definition of frequency and definition of Strouhal number, one has:

$$N = \frac{L}{\lambda_v} + \frac{L}{\lambda_p} \quad (3.2)$$

$$N = \frac{L f}{c_v} + \frac{L f}{c_p} \quad (3.3)$$

$$St = \frac{fL}{U} = \frac{N}{\frac{U}{c_v} + \frac{U}{c_p}} \quad (3.4)$$



Where:  $L$  is the cavity length;  $f$  refers to  $f_o$ , either the frequency at which the acoustic waves are generated or the frequency of vortex shedding (which are the same);  $c_v$  and  $c_p$  are respectively the convection speed and the speed of sound;  $U$  is the flow speed. Such formula has been finally corrected by Rossiter [31], who noticed a systematic shift in the data. He defined the ratio  $U/c_v$  as an experimental ratio to be found and the shift as  $N' = N - \gamma$ . The final formula is given by equation 3.5:

$$St = \frac{N - \gamma}{\frac{1}{\kappa_v} + M} \quad (3.5)$$

The frequency  $f_o$  are referred as vortex shedding frequencies (or frequency of acoustic waves), which nowadays are recognized as **Rossiter's mode**.

Note that the Strouhal number accounts for the cavity length  $L$ : equation 3.5 does not consider other geometrical properties of the cavity such as depth or width. Rossiter noted however that they play an important role, which is hidden behind the shift value  $\gamma$ . Based on the ration  $L/D$  (length/depth), Rossiter proposed different values for  $\gamma$ . Some results are displayed in table 3.1. Provided with the

$L/D$	$\gamma$
4	0.25
6	0.38
8	0.54
10	0.58

Table 3.1:  $\gamma = \gamma(L/D)$ .

excitation source (the vortex shedding) occurring at  $f_o$ , in case of  $L \approx \lambda$ , a **fluid-resonant only** type of oscillation can occur. Given the excitation source and its frequency, what could happen now is a tuning situation with respect to the fluid within the cavity (the resonator). In the previous chapter, some elemental resonators (discrete and distributed) were analyzed. These resonators will have a significant effect when, in the field of  $L \approx \lambda$ , the excitation frequency  $f_o$  will start to match the resonator frequency: lock-in condition might occur, and high amplitude oscillations could occur. With basic rectangular cavities, standing waves are going to occur. Later in this chapter, *shallow cavities* will be distinguished by *deep cavities*.

An important task is to define the variables that are necessary to describe properly this phenomena. The main reference for this new section is [25]: Gloerfelt discussed systematically all the variables, by dividing them in categories.

## 3.2 PHYSICALLY SIGNIFICANT PARAMETERS

### 3.2.1 GEOMETRICAL PARAMETERS

For the scope of this work, simple rectangular cavities will be discussed. Figure 3.3 introduces a new terminology that is adopted in the following chapters. The front edge is called *trailing edge* due to its similarity with an airfoil trailing edge, where the wake is formed. In the same way, the rear edge is called *leading edge* since it represents the edge where the flow impinges. Based solely on the  $L/D$  ratio, a more practical than theoretical distinction is made between **shallow cavities** and **deep cavities**: many in the literature have adopted different criteria to distinguish them. According to Sarohia [5] and other authors, shallow cavities are those cavities with a length-to-depth ratio higher than 1 ( $L/D > 1$ ), and the contrary for deep cavities ( $L/D < 1$ ). According to Gloerfelt [25], only the definition of shallow cavities changes, that considers cavity with  $L/D > 2$  as shallow, leaving an intermediate range  $1 < L/D < 2$  as a transition range not properly defined. There is a great literature behind shallow cavities, mainly because the research on cavity acoustics moved from bomb bays of aircraft's fuselage, of which the ratio  $L/D$  was higher than 2.

First of all, independently from the boundary layer type (laminar or turbulent), disturbances will always be present, provided that the minimum length  $L_{min}$  (Sarohia [5] called it  $b_{min}$ ) is reached. Changing the

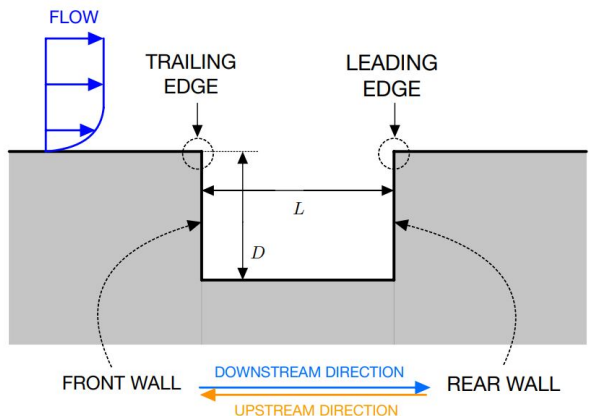


Figure 3.3: Geometrical dimensions of a rectangular cavity:  $L$  and  $D$  are respectively the cavity length and the cavity depth (in the third dimension,  $W$  is defined as cavity width).

$L/D$  ratio has a great effect on pressure distributions over the three walls of the cavity. Roshko [6] was among the first authors to describe such changes, who performed multiple measurements for different  $L/D$  ratios over the three wall. The main effect that is here reported is the pressure rise on the bottom wall of the cavity for different  $L/D$  (see figure 3.4). As it is clear, the smaller the ratio  $L/D$ , the closer the trailing and leading edge will be, thus meaning that the stagnation pressure originated by the impingement of the shear layer on the leading edge will create a pressure field that will interact almost instantaneously with the trailing edge. The higher the ratio  $L/D$ , the further the pressure rise will be located from the trailing edge. This behavior seen is indicative of the base-pressure issue, specifically related to the flow passing over a step. From figure 3.4 one can also see some examples of deep cavities ( $d/b = 1$ ) where

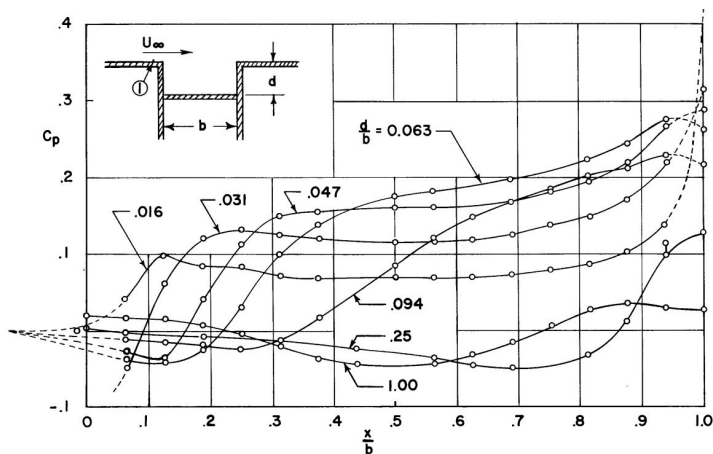


Figure 3.4: Pressure profile on the cavity floor for different  $L/D$ . Reference for the picture: [6].

a more uniform pressure profile can be found, could be related to the shear layer simply bridging over the cavity, thus leaving the pressure field within the cavity almost undisturbed. Furthermore, for deeper cavities, the pressure on the bottom (expressed in terms of pressure coefficient  $C_p$ ) is oscillating around zero: shallow cavities can create a stagnation point with significantly higher pressures. This will affect as well the magnitude of the pressure waves that are generated.

In case of shallow cavities, strong three-dimensionality effect are found, especially at the sides (over the width). Deeper cavities instead appear to have a more uniform behaviour along the width, therefore easier to be analyzed by considering their 2D evolution. Despite that, near wall effects haven't been considered in case of deep cavities: later in this work, some consideration are made on the topic due to the analyzed wind-tunnel.

The previous equation 3.5, representing the Rossiter mode, indicates the frequency at which pressure waves are generated, thus, due to the feedback condition, the frequency of vortex shedding at the trailing edge. Relation 3.5, according to [7], fails to correctly predict the Strouhal number for subsonic flows. In fact, given equation 3.5 and table 3.1, for increasing values of  $L/D$ ,  $\gamma$  increases, whereas the results presented in [7] show an inverse relation. The modified relation proposed by Block [7] is hereafter shown:

$$St = \frac{n}{\frac{1}{\kappa_v} + M \left( 1 + \frac{0.514}{L/D} \right)} \quad (3.6)$$

One of the main difference between shallow and deep cavities is in the PSD they present. Usually, when performing the Fourier Transform of a pressure signal, the different peaks spotted in the PSD are associated with different modes. Something that was noticed already by Rossiter in his work [31] was that shallow cavities would show in their PSD more than one peak, whereas deep cavities usually presented a single peak. By further elaborating the terminology adopted in this work, one defines **dominant frequency** (or **primary frequency**) the mode with the highest peak in case multiples peaks are displayed in a PSD. Figure 3.5 shows the mode switching of in case of deep and shallow cavity. Rossiter at that

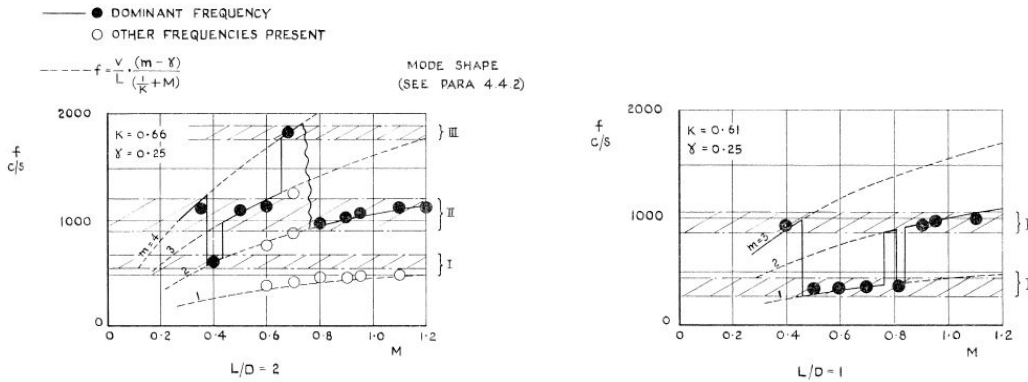


Figure 3.5: Frequencies of period oscillations in cavities. On the left, shallow cavity; on the right, deep cavity.

time didn't really understood the reason of the single peak, but he thought about the possible interaction of the vortical mode with the depth-wise resonance frequency of the cavity. This was confirmed later by Block [7], helped by the extensive work done by Pumblee *et al* [32], who discussed the interaction between the lengthwise mode (the Rossiter mode) and the depthwise mode (formula proposed by [32]). In Figure 3.6, the measured frequencies (Strouhal number) are located close to a curve that corresponds to either type of oscillation. When  $L/D$  is small, the data tends to follow the depthwise standing-wave oscillation curves, especially at lower Mach numbers ( $M = 0.1$ ) where the slope of the curves is steep. However, the data does not continuously follow the standing-wave curves but clusters around the intersection with the curves of Rossiter's mode. This interaction occurs also for shallower cavities, as seen in the case where  $L/D = 2$  where the data follows the lines of vortical-acoustic oscillation, but starts near the intersection with the standing-wave oscillation lines. The crossing in figure 3.6 represents the exact resonance condition, for which a lock-in of the excitation frequency  $f_o$  of Rossiter's mode occurs ( $f_o = f_R$ ). Oscillations are highly amplified, and it is possible to spot them clearly.

Creating a bridge between Rossiter's work and Block's one is not as easy as it might seem. Rossiter investigated specifically his modes for high subsonic regime, whereas Block analyzed the interaction of such modes with depthwise ones recurring to a new formulation, applied in the low subsonic regime. Still today, a coherent and comprehensive description of the two modes and their interaction for all Mach cannot really be found.

### 3.2.2 MACH NUMBER

The geometry of the cavity is not the only subject playing a role in determining the cavity acoustics phenomena. Flow properties are very important to the cause: Mach number, Reynolds number and

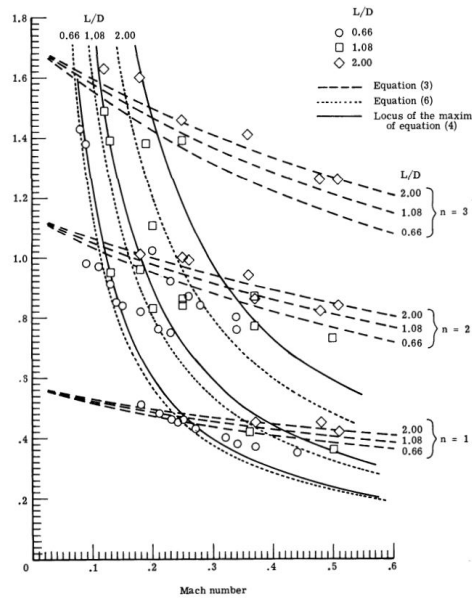


Figure 3.6:  $St = f(M)$ . Comparison between Rossiter’s mode and depth-wise modes. Equation (3) in the figure indicates the modified Rossiter formula (equation 3.6), whereas equation (4) and (6) in the figure refer to the depth-wise resonance formula. Reference for the picture: [7].

boundary layer thickness are extremely important factors that are affecting both the frequency and, most importantly, the amplitude of the oscillations, which can be captured only when performing a PSD.

For what concerns the **Mach number**, it certainly affects the frequency, as it can be seen from Rossiter’s formula (equation 3.5). The Strouhal number, for increasing Mach, decreases, however the frequency increases as Mach increases, assuming the same speed of sound. This further justifies the feedback mechanism in the sense that if the frequency did not change, then the cavity would be passive, and some resonances would be triggered in an unjustifiable way only for some specific frequencies. A ”trigger” condition is always present when concerning cavity acoustic, and occurs whenever the vortical feedback tunes with a resonant frequency of a cavity. However, having  $St = St(M)$  leads to a vortical feedback function of the Mach number, ultimately allowing the tuning. According to Tam & Block [33], Rossiter’s formula doesn’t really succeed in estimating the frequencies. It better suits the Mach numbers in the range  $0.4 < M < 1.2$ : for lower Mach, the formula fails. Figure 3.7 shows this graphically. For

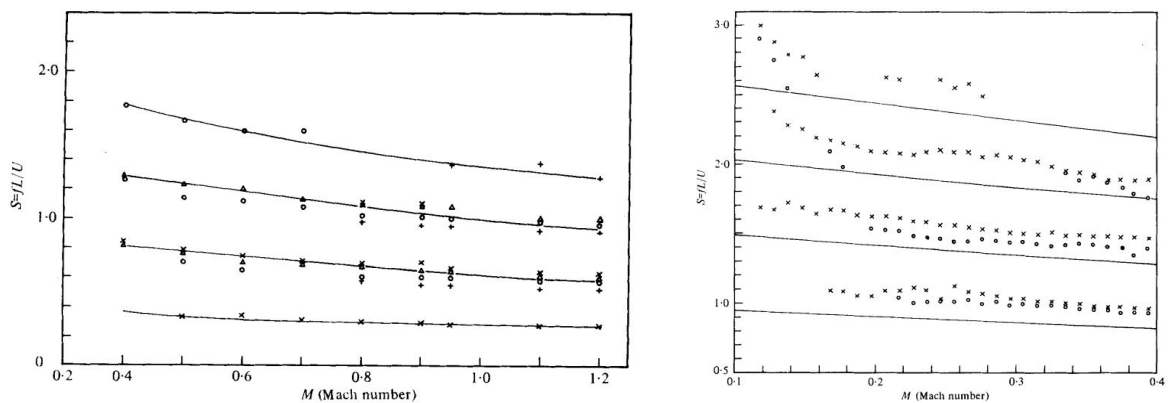


Figure 3.7: On the left, the Rossiter’s formula is used to fit the experimental results: for  $0.4 < M < 1.2$ , equation 3.5 works fine (with  $\gamma = 0.25$  and  $\kappa_v = 0.57$ ). On the right, Tam & Block showed that for lower Mach ( $M < 0.4$ ) equation 3.5 (black line) doesn’t properly represent the dataset. Reference for the picture: [8].

higher Mach, mainly supersonic, the formula also failed to predict the Strouhal number. For this reason, a modified formula was proposed by Heller *et al* [8]. The formula, known as *modified Rossiter's equation*, is hereafter given:

$$St = \frac{N - \gamma}{\frac{1}{K_v} + \frac{M}{\sqrt{1 + \frac{\gamma-1}{2} M^2}}} \quad (3.7)$$

Despite their effect on the frequency, other effects can be found on the amplitude of the acoustic waves. Ahuja & Mendoza [9], reported in their extensive work the impact of different Mach numbers on the noise level. The results are shown in figure 3.8: From figure 3.8, clearly its visible that an increase of Mach

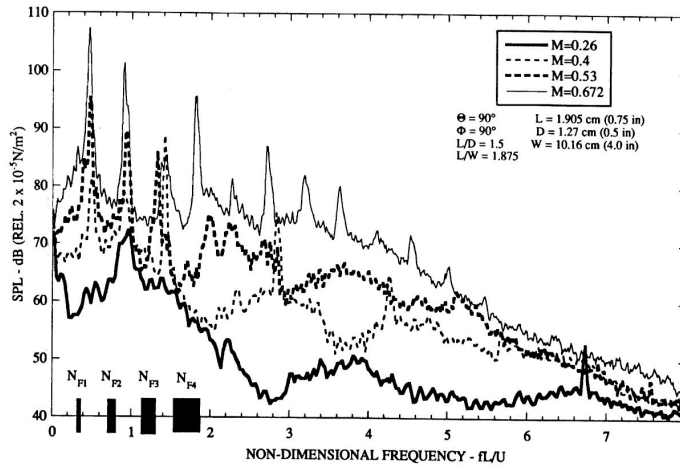


Figure 3.8: PSD for different Mach numbers (geometry is fixed). Reference for the picture: [9].

generates an overall increase of the noise level. More specifically:

- Increasing the Mach increases the peak amplitude of both the Rossiter's mode and the cavity resonance modes (the peaks);
- Increasing Mach increases the overall broadband noise level (doubling the Mach increases the noise of almost 30dB).

Something else that occurs with increasing Mach is an increase of drag force. For this reason, when flying at high Mach values, eventual cavities in the fuselage of an aircraft could bring unexpected problems. Ahuja & Mendoza noticed that usually only the second and the third mode would be dominant ones.

For very high Mach numbers, according to Block[7], it's not always possible to see a mode. This is related to the minimum length that was derived by Sarohia [5]: it is also function of the Reynolds number. An interesting point of view offered by Block [7] is based on some observations in figure 3.6. As mentioned, in figure 3.6, Rossiter's mode and depth-wise resonances are displayed for different Mach. The curves are function of Mach, and for each Mach the relative expression gives the value of frequency for which one could expect the maximum amplitude in a PSD, at a given Mach. Therefore, the crossing between the two curves, corresponding to Rossiter and depth modes, identifies a specific Mach number for which both Rossiter's mode and depth-wise mode oscillate at the same frequency, allowing lock-in and cavity resonance. The takeaway is that the tuning of acoustic feedback and cavity resonance is only function of the Mach.

### 3.2.3 BOUNDARY LAYER TYPE AND THICKNESS

The thickness of the incoming boundary layer plays a decisive role when it comes to mode selection, related to the selective amplification. Gharib & Roshko were the first to understand the importance of the boundary layer. Instead of sticking exactly to the boundary layer thickness, defines in the literature

of boundary layer as  $\delta_{99}$ , the **momentum thickness**  $\delta_2$  was used, defined according to equation 3.8 hereafter shown:

$$\delta_2 = \int_0^{\infty} \frac{u}{U_{\infty}} \left( 1 - \frac{u}{U_{\infty}} \right) dy \quad (3.8)$$

This parameter was usually investigated in terms of the dimensionless factor  $L/\delta_2$ , with  $L$  being cavity length. The importance of this coefficient is related to minimum length  $L_{min}$  derived by Sarohia. The reason is that below this critical length value,  $L_{min}$ , the roll-up of the free-shear layer is not possible. A roll-up mechanism is displayed in figure 3.9 here below: Depending on how the shear layer will roll

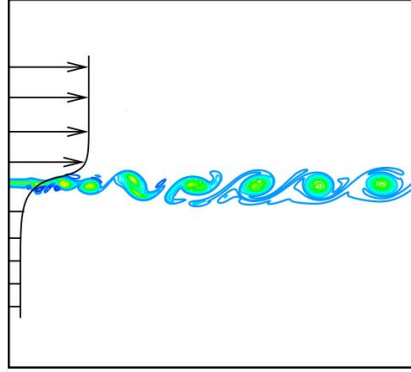


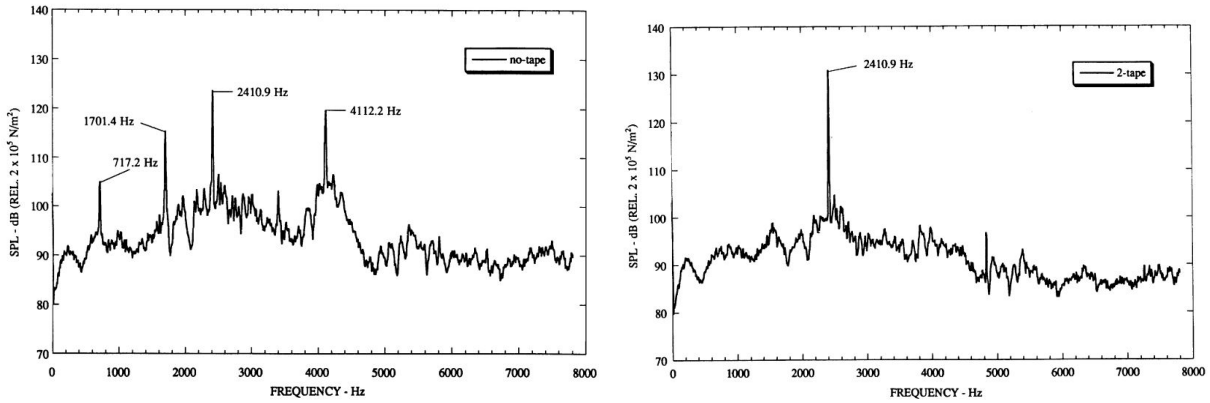
Figure 3.9: Roll-up of a free-shear layer. Reference for the picture:[10]

up and how many vortices will be generated, one specific Rossiter mode will be excited. The growth of the instability in a shear layer is well described in [34]. Here, the main focus evolves on the influence of the boundary layer on the amplitude of the vortical modes. Typically, previous studies [35, 8] have been accomplished by slowly increasing the mean flow velocity and observing changes in cavity vortical modes as the flow transitions from laminar to transitional to turbulent states. Some studies have involved starting with a laminar boundary layer and then tripping it to become turbulent. However, it is challenging to isolate the effect of the boundary layer type (i.e., laminar or turbulent) and the thickness of a given type of boundary layer. Krishnamurty [35] found from his experiments that, in every scenario tested at a certain Mach number, the emitted sound was less intense when a turbulent boundary layer was present before the gap compared to a laminar layer. When the boundary layer was laminar, the resonant frequencies were quite visible from the PSD as sparks. On the other hand, when the boundary layer was turbulent, the PSD appeared dispersed, as white noise. He found that in case of turbulent boundary layer, the phenomena was stronger (thus, the sound emitted was louder). Ahuja & Mendoza [9] reached the same conclusion. A more detailed discussion was presented in their work, including not only the difference on the boundary layer types but also providing measurements on the boundary layer thickness  $\delta_{99}$ . Ahuja & Mendoza were able to thicken the boundary layer by simply introducing some backward facing steps placed just upstream the cavity trailing edge (upstream edge) to induce turbulence. Figure 3.10 shows a comparison of three PSD, each of which derived with different types of boundary layer.

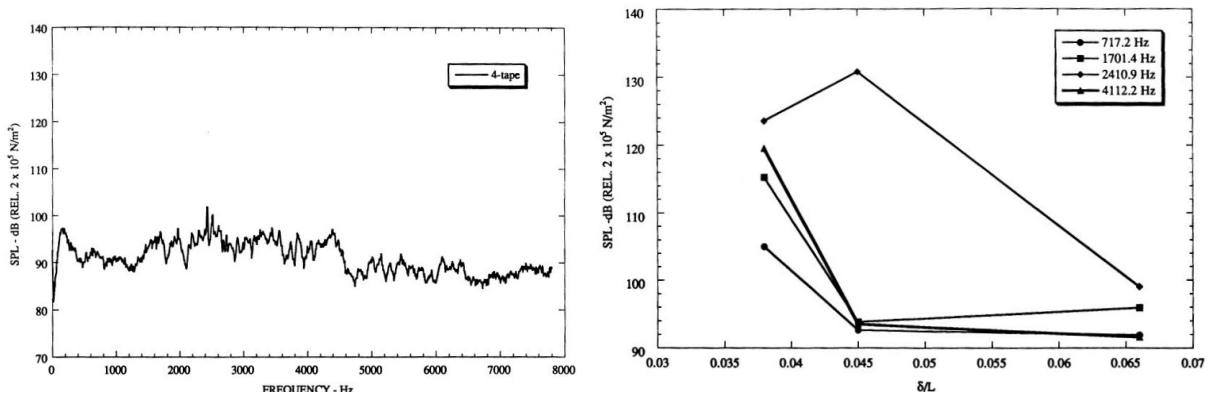
The concluding remarks of Ahuja & Mendoza were that not only a thicker boundary layer tends to eliminate most of cavity's modes, but such modes are also reduced to the broadband level (by a consistent reduction of the noise).

An interesting review is presented by Grace *et al* [36]. She and her colleagues resumed the current knowledge on the influence of the boundary layer and momentum thickness, respectively  $\delta_{99}$  and  $\delta_2$ . They mention also how the results before discussed by Ahuja & Mendoza fails when applied to water flow past cavities (Ahuja & Mendoza utilize air in their experiments). According to Grace's review, in order to have vortical modes:

- In the **laminar case**, one needs to have:
  - $80 < L/\delta_2 < 155$ , according to Gharib & Roshko [37];
  - $L/\delta_2 < 100$ , according to Sarohia [5] (an upper limit), and at the same time  $L/\delta_{99} \cdot Re_{\delta}^{1/2} > 290$



(a) PSD of acoustics measurements with laminar boundary layer (no tape means no turbulator to disturb the flow). (b) PSD of acoustics measurements with a slightly turbulent boundary layer (2-tape means that two steps were used to induce turbulence).



(c) PSD of acoustics measurements with a strong turbulent boundary layer (4-tape means that four steps were used to induce turbulence). (d) Amplitude (in terms of  $dB$ ) of the acoustic measurements of the peaks as a function of the boundary layer thickness.  $\delta$  refers to  $\delta_{99}$ .

Figure 3.10: From figure 3.10a to figure 3.10c, the PSD of acoustic measurements for laminar and turbulent layer; figure 3.10d shows intensity of the noise (of the peaks) for different  $\delta_{99}$ . Reference for the pictures: [9].

- In the **turbulent case**, one needs to have:

$$- \delta_{99}/L < 0.0666, \text{ according to Ahuja \& Mendoza [9].}$$

For a deeper insight, refer to Grace's work [36].

### 3.2.4 REYNOLDS NUMBER

Usually, in the literature, two different Reynolds number are used. The first one is  $Re_L$  refers to length  $L$  of the cavity. Usually authors refer to that number simply as  $Re$ , and it's expression is given below in equation 3.9:

$$Re_L = U_\infty \frac{L}{\nu} \quad (3.9)$$

The second Reynolds number  $Re_\delta$  uses as reference length the thickness of boundary layer. It's expression is given in equation 3.10:

$$Re_\delta = U_\infty \frac{\delta}{\nu} \quad (3.10)$$

The values of  $Re_L$  are much higher than  $Re_\delta$ , related to the difference between cavity length (from few hundred millimeters up to several meters) and boundary layer thickness (usually few millimeters).

The relevance of the Reynolds number for this applications is related to the thickness of the boundary layer. High Reynolds number are associated with thicker boundary layers. Low Reynolds number are instead associated with laminar/transitional boundary layers. This is not always the case though: even in case of low Reynolds number, one can have very turbulent and thick boundary layer by placing some turbulators just upstream the cavity.

In general, results from the literature [9, 35] show that high Reynolds number flows are characterized by both broadband noise and self-sustained oscillations. High Reynolds are also associated with small eddy scales, that could reorganize themselves through a coalescence process: the Rossiter modes may then exist in more than one state, jumping between different modes as the coalescence gives different results.

At low Reynolds number, the process of selection of the mode is more sensitive to the exact value of the Reynolds (sensitivity that is lost at high Reynolds exactly because multiple modes can be excited simultaneously).

### 3.3 REVIEW ON NUMERICAL SIMULATIONS FOR CAVITY ACOUSTIC PROBLEM

Research on cavity flow has largely relied on wind-tunnel testing to produce data. However, recent developments have seen wind-tunnel data being used to validate results obtained through Computational Fluid Dynamics (CFD) simulations. While the cost of wind-tunnel testing is a key driver behind the increased use of CFD, there are additional benefits to be gained once the CFD solution has been validated. Wind-tunnel data acquired through traditional methods, such as Kulite pressure transducers, provide high temporal resolution but low spatial resolution. On the other hand, more recent and costly methods, such as Particle Image Velocimetry (PIV) or Laser Doppler Anemometry (LDA), offer high spatial resolution but low temporal resolution. CFD, however, offers the advantage of providing high levels of both spatial and temporal resolution. Direct Numerical Simulation (DNS) is the most straightforward approach to solving the Navier-Stokes equations, but it requires a fine grid and a small timestep in order to fully resolve the turbulent scales. An attempt was tried by Gloerfelt *et al* [38] back in 2001. A cavity with an aspect ratio ( $L/D$ ) of 2 was analyzed with a free-stream Mach value of 0.7. Although the very good results in accordance to Rossiter's formula, the computations were very strict in terms of requirements: for a 5mm long cavity, a stream-wise space step of  $3\mu\text{m}$  was used, with a  $y^+$  of 0.8. The main problems concerns the CFL number which, in order to be less than 1, imposed a time step of  $6.06 \cdot 10^{-9}$ , which increased the computational effort tremendously. The purpose of the CFL number is explained in the following chapters. Given the current limitations of computational resources, DNS has limited application to the problem of cavity flow. To obtain results for high Reynolds number flows within realistic time scales, alternative methods such as Reynolds-Averaged Navier-Stokes (RANS), Large-Eddy Simulation (LES), and Hybrid RANS/LES (such as DES) are employed, all of which incorporate some form of turbulence modelling.

Back in the 90's, with the development of first CFD codes, URANS simulations were initially performed. The first problem that researcher faced was the choice of the turbulence model. To this day, a lot of research is still ongoing on the best choice for the parameters to be used, since results coming from the simulations exhibits a strong and very sensitive dependence on the turbulence model adopted. According to Gloerfelt [25], the numerical solution happens to be strongly sensitive on the turbulence model. The very first turbulence models to be where the Cebeci-Smith and Baldwin-Lomax, according to Lawson & Barakos. Solutions obtained from the Cebeci-Smith didn't showed any self-sustained oscillation despite giving a fairly reasonable pressure field, whereas Baldwin-Lomax model tended to over-predict the pressure on the downstream wall but were able to capture up to the second Rossiter mode. These first simulations involved both deep cavities and shallow ones.

With new advances made in CFD, new turbulence models were adopted, such as the *two-equations turbulence models*:  $k - \varepsilon$  and  $k - \omega$ . URANS, as described in [39], tend to give good approximations of larger scales associated with the firsts vortical modes, but fails at capturing higher modes (higher frequencies) and broadband. Moreover, depending on viscosity values, dissipation may damp extremely fast any flow oscillation, therefore making it hard to capture the shear layer oscillations and the vortex roll-up. In the literature, generally speaking,  $k - \omega$  and *SST* models are preferred over  $k - \varepsilon$  since the former are able



to correctly predict flow separation. Sadiq & Sabir in their work [12] compare the experimental results of Suhs [11] with different numerical results derived with different turbulence models. The comparison is shown in figure 3.11, which shows the Sound Pressure Level (SPL), defined as:

$$SPL = 20 \log_{10} \left( \frac{p_{rms}}{p_{ref}} \right) \quad (3.11)$$

With  $p_{ref} = 2 \cdot 10^{-5} Pa$ . According to figure 3.11, SST method is the one giving fairly good results, mainly

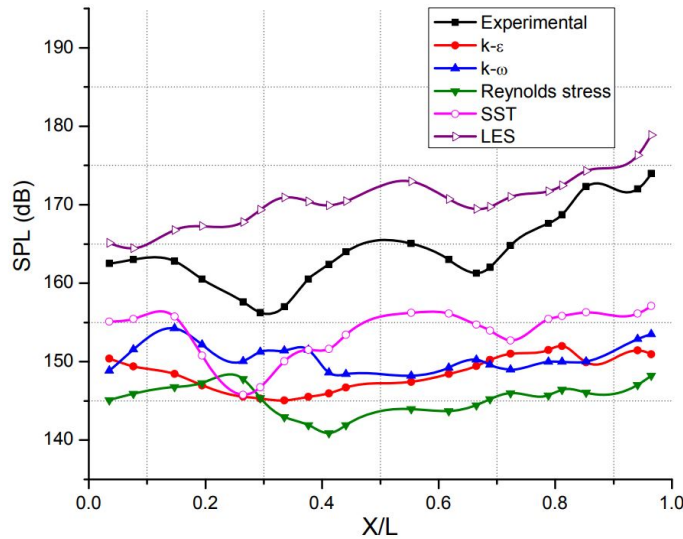


Figure 3.11: Comparison of the experimental results of Suhs [11] (refer to his work for details on geometry) and numerical simulations of Sadiq & Sabir [12]. Reference for the picture: [12].

concerning the path of the curve. One of the issues with this turbulence model, however, as the same authors discuss in their work [12], is the strong dependence of the result on the coefficients of the SST turbulence models. An interesting result of URANS simulations is the distinction between wake mode and shear layer modes at different Mach values. For instance, Mesbah & Majidi [13] analyzed different Mach values, ranging from 0.2 to 0.7, with a cavity aspect ratio of 4, keeping the same depth-Reynolds number and  $L/\theta_0$  value. The authors used SST turbulence model, and the results were compared with previous DNS and LES results from previous authors (see their paper for specific references). A precise prediction of the shear layer mode for  $M = 0.2$  and the wake mode for  $M \geq 0.4$  was achieved, whereas for  $M = 0.3$  a wake mode was detected, with the DNS instead showing a mix between the two modes. Note, that shear layer mode is the already known Rossiter's mode, whereas the wake mode is characterized by the shedding of a large vortex, similar to the one that occurs in flow past bluff bodies. Figure 3.12 presents some vorticity contours and pressure contours of the flow for the shear layer mode and figure 3.13 for the wake mode.

They noted that an increase of Mach number by 0.1 magnifies the amplitude of the dominant mode by 11dB. Furthermore, for the wake mode, they noted that the corresponding Strouhal number  $St (= 0.26)$  was barely affected by the Mach number, therefore their conclusion was that the acoustic feedback was absent for the wake mode, in agreement with previous studies. Figure 3.14 shows a comparison of the Strouhal numbers for different Mach, for URANS (their work, using SST), LES and DNS (according to previous authors): good agreement could be found with previous authors, although they don't really match the values proposed by Rossiter.

One of the possible reason for a non-proper agreement with numerical values of the Rossiter's formula or experimental results lies also in two empirical coefficients of Rossiter's model. If one re-calls the expression, of equation 3.5, two empirical coefficients appears:  $\gamma$ , which is the time lag (dimensionless) between the disturbance shedded at the trailing edge and the generation of the acoustic wave, and  $\kappa_v$ , which is the ratio between propagation speed of vortices and free-stream velocities. Liliedahl *et al* [14]

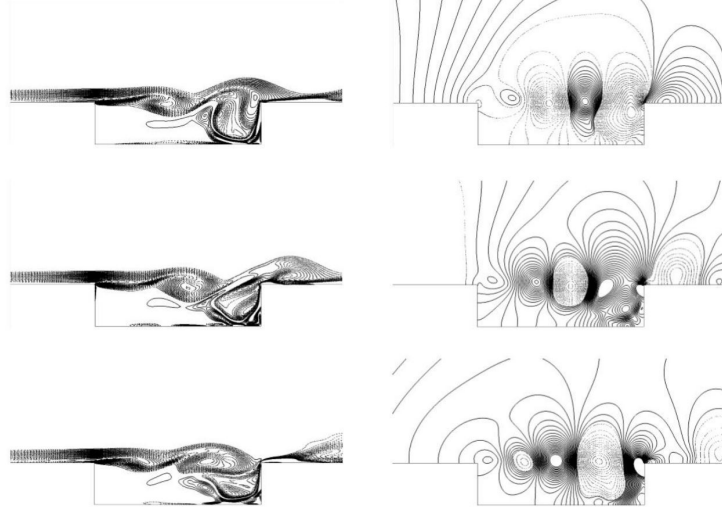


Figure 3.12: Shear layer mode: acoustic feedback occurs in this case. Reference for the picture: [13].

tried to compute  $\kappa_v$  numerically and noted that after replacing the  $\kappa$  with their computed values, a good agreement between numerical and experimental results was found. Computations were based on pressure contours, such as the one shown in figure 3.12 and 3.13. The reason they based the computation on the pressure value was because the core of the vortices that were shedded from the trailing edge are associated with lower pressures: therefore, by keeping track of the pressure change along the cavity mouth, a velocity-profile was depicted for a vortex. The result is shown in figure 3.15.

An average value was chosen for  $\kappa_v$ .

Previously, it was discussed the very low time-step used by Gloerfelt in his simulation ([38]). Although it seems extremely low, the most used values used in the literature are usually  $10^{-6}s$ , and sometime also  $10^{-7}s$ . The main reason for such small steps is related to the  $y^+$  used. In order to have a resolved boundary layer, a  $y^+$  of around 1 is required. According to Shieh & Morris [15], to achieve this, the thickness of the first element of the mesh starting from the wall must be  $0.0002D$ , with  $D$  being the cavity depth. Finally, to be compliant with low Courant number, a proper time-step must be chosen. It has to be pointed out that Navier-Stokes equations are non-linear elliptic equations, therefore the CFL conditions doesn't really apply: still, it is a good measure to avoid error amplification. Shieh & Morris noted that a low value of  $y^+$  imposes low value in the final  $\Delta t$ . Therefore, in their work [15], they adopted a  $y^+$  of around 50, so that a wall function could be applied and a coarser time-step could be used. The simple Spalart-Allarmas turbulence model was used, and the result were compared with a parallel simulation in which a finer mesh was used and an Hybrid RANS/DES turbulence model was adopted. The analyzed Mach number was of 0.6. The results of both simulations didn't matched the numerical values of the Rossiter's model. Therefore, the coefficient  $\kappa_v$  was tuned, this time by simply looking at different vorticity contours in time. Once the  $\kappa_v$  coefficient was computed, good agreement with the Rossiter formula was found.

Shieh & Morris were also among the first to start 3D simulations for cavity flows. The main drawback when it comes to 3D simulations is the computational cost: meshes can get even twenty times bigger (in terms of number of elements), therefore making transient computations very time-demanding.

Nowadays, as experiments and DNS approaches become more affordable, ad-hoc coefficients could be derived and a regression model can be used to cover wide ranges of operating conditions and geometry influence.

As a consequence of the high cost of DNS and the inadequacy of URANS in predicting small turbulent scales in the cavity accurately, alternative methods have emerged in the literature. The underlying principle of LES is to capture the larger, energy-containing eddies on the grid while using a sub-grid scale model to simulate the smaller, more isotropic scales. However, difficulties persist in resolving the turbulent stresses close to the walls, as the computational resources required are comparable to those of DNS. Therefore, many computations use a reduced Reynolds number, as with cavity flow simulations

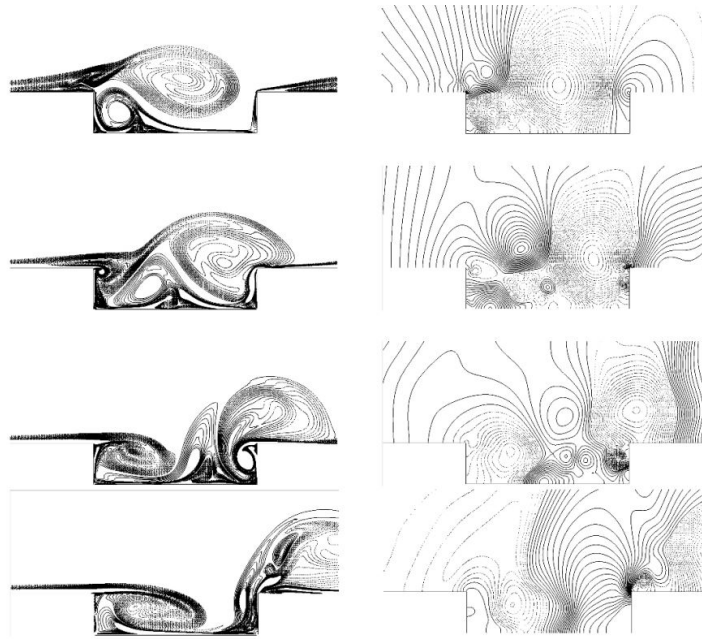


Figure 3.13: Wake layer mode: a large vortex is shedded from the trailing edge, which will impinge on the leading edge causing vortex disruption with great mass ejection from the cavity. Reference for the picture: [13].

utilizing DNS. Similar to other numerical approaches, various sub-grid models have been developed for LES. The most commonly used models are variants of the Smagorinsky model, but it has a major drawback in describing the scale reduction that occurs near the solid walls. Thus, many computations add an empirical wall law near solid boundaries, enabling the use of relatively coarse grids in close proximity to the walls. Another emerging approach gaining traction is Implicit LES (ILES). Other than modified LES models, an efficient alternative are hybrid RANS-LES methods. Arunajatesan & Sinha discuss in their work [40] the advantages associated with such method. They start from the realization that the flow within the cavity is much more complex than the upstream flow: the dynamics of the flow within the cavity are dominated by non-linear pressure fluctuations and resonant acoustic waves, which have significant effects on the dynamic loads acting on the store. In terms of modeling, the flow field contains enclosed regions that necessitate the use of LES techniques, as for the shear layer located above the cavity; however, the remaining part of the aircraft (in their work [40]), as well as the upstream boundary layer, may be adequately modeled using RANS methods. As mentioned by Gloerfelt [25], progress in the numerical simulations rely on the comparison with experimental data. This comparison will allow to define a proper choice of coefficients to be employed in the turbulence models. Numerous studies have been done to shed light on this topic, although a generalization and overall operating framework is still missing.

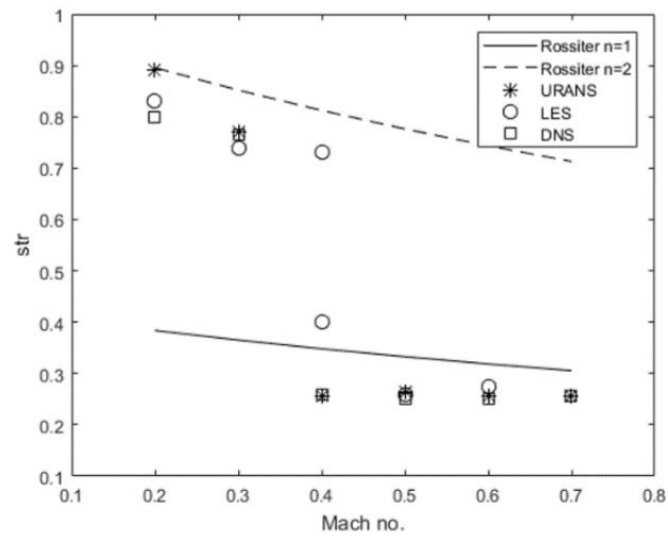


Figure 3.14: Comparison of RANS vs LES vs DNS vs Rossiter's formula. Reference for the picture [13].

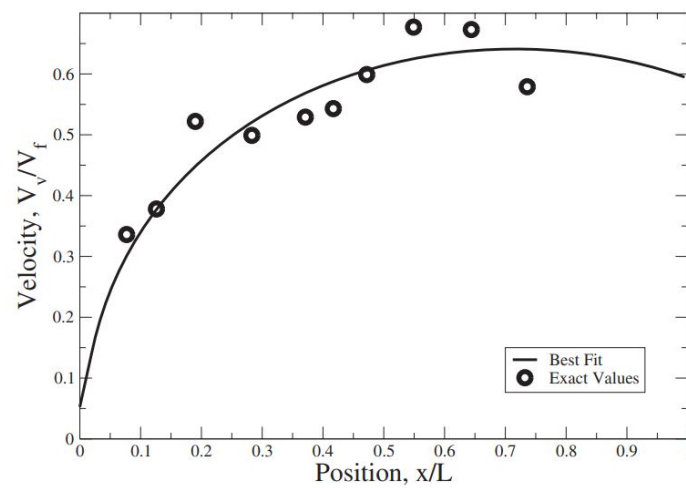


Figure 3.15:  $\kappa_v$  coefficient over the cavity mouth. Reference for the picture: [14].

## Chapter 4

# METHODOLOGY

As stated in the introduction, the objective is the validation of the experimental measurements derived by Hammer *et al* [24] on a rectangular cavity with adjustable depth, inserted in a wind tunnel. Description of the wind tunnel and of the instrumentation are given in Hammer's work, as well as in further chapters.

The numerical validation process aims at deriving an unsteady simulation by means of **ANSYS CFX**, using proper initial and boundary conditions, and extrapolating the pressure fluctuations at some specific points (the monitor points), similar to the measurement locations during the experimental testing. These pressure fluctuations are post-processed with **Matlab**. Fourier analysis is carried to derive the main frequencies responsible for pressure fluctuations. If those frequencies are coherent with the measured ones, the validation process ends successfully. Limitations on the model are discussed eventually, together with the chosen parameters for the simulations.

This validation process is distinguished in two blocks:

1. Steady State simulations of the wind tunnel;
2. Unsteady simulations of the cavity;

In figure 4.1 a scheme of the wind tunnel with the cavity section is showed. Since the unsteady measure-



Figure 4.1: Wind tunnel with cavity section.

ments is demanding both in terms of time and memory, it's necessary to reduce the domain, if possible, shortening as much as possible the length of the simulation. One way of doing so is by defining two different domains which will be respectively employed in the steady and unsteady part:

1. The first domain, used for the *steady analysis*, consists in the **wind tunnel only**, without the cavity;
2. The second domain, used for the *unsteady analysis*, consists in the **cavity section**, without the whole wind tunnel.

See figure 4.2 to see the two domains. The first block aims at analyzing the wind tunnel only (see figure

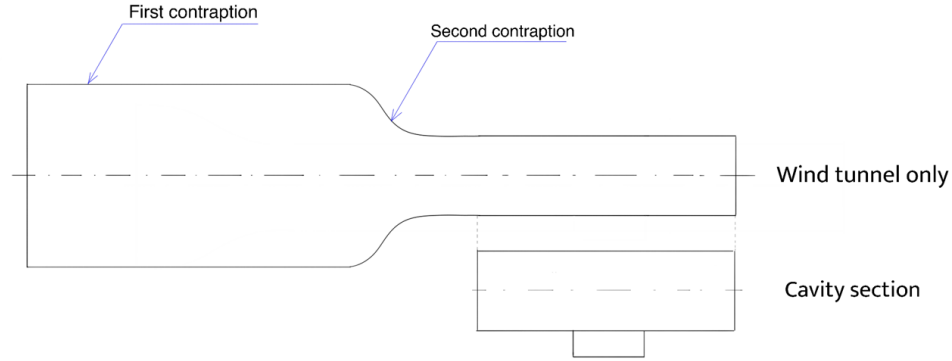


Figure 4.2: Domain splitting for the steady and unsteady analysis.

4.2). A mesh independence study is performed with different meshes of the wind tunnel which aims at defining the operative mesh that will be used afterwards for all operating points. The parameter chosen to validate the mesh independence study is the total pressure profile at a specific location. The mesh independence study is carried at  $M = 0.5$ . In the process, one assumption is made: the outlet pressure  $p_{out}$  downstream the wind tunnel (including a shallow cavity) is known, but it will be used as outlet boundary condition for the wind tunnel only. This implicitly assumes that the cavity hasn't any impact on the  $p_{out}$ . From a theoretical point of view, such assumption is wrong since the cavity is adding a concentrated loss, therefore the  $p_{out}$  that is used in the wind tunnel only should be a bit higher; from a practical point of view, that loss is almost negligible. After the mesh independence study is completed, some methods to match the numerical profile with the experimental one are implemented. Note that the discussion in the whole chapter is done for  $M = 0.5$ . After the comparison, the velocity profile that was used to validate the measurements is extrapolated and serves as a starting point for the unsteady part. In fact, for the unsteady analysis of block two, the numerical extracted velocity profile is used as inlet boundary condition for the cavity section. Figure 4.3 shows schematically the process. Note that the drawings might seem two-dimensional, but the actual problem is three-dimensional since the cavity has a width that is smaller than the width of the whole wind tunnel. Figure 4.4 points this difference. Despite the three-dimensionality of the problem, a 2D case is considered by neglecting the width of the cavity and of the wind tunnel. The purpose of the 2D analysis is to choose the correct turbulence model, to define a correct procedure to effectively mesh the domain with good accuracy on the frequency prediction, and to see in first place if the CFD code is able to capture such frequencies.

The mesh independence study is carried out for the 2D case where simulations takes normally much less time. The operating point that is used for this study is  $M = 0.4$ . After the mesh independence study, a small discussion follows aiming at defining additional parameters (i.e. time step). Finally, once the setup is defined, simulations are carried for all operating points and compared with experimental results from Hammer [24].

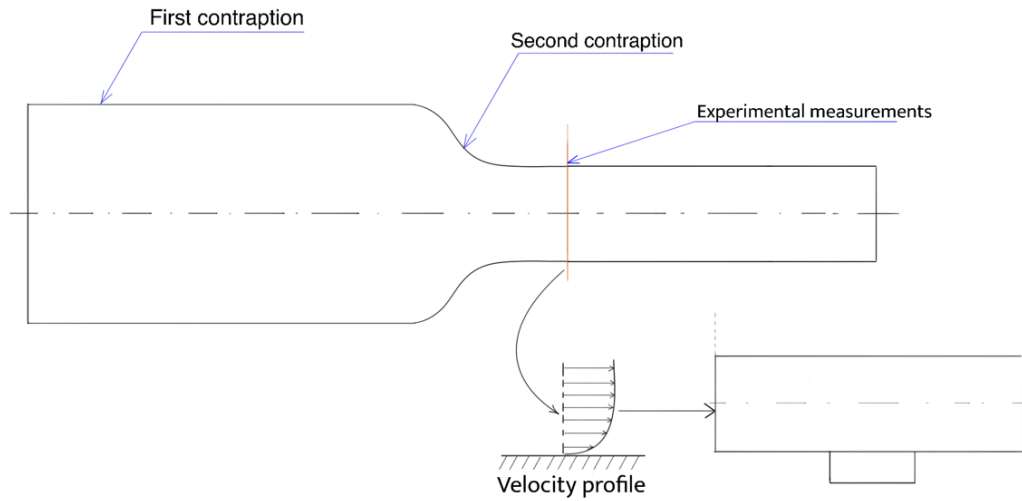


Figure 4.3: The extrapolated velocity will be compared with the experimental measurements and then will be used as inlet boundary condition for the cavity only.

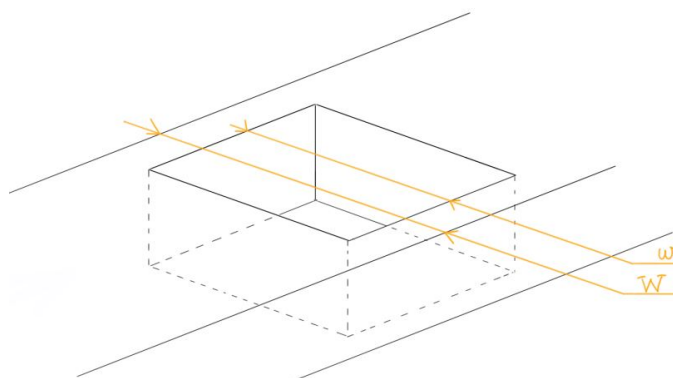


Figure 4.4: Three-dimensional view of the cavity:  $w$  is cavity width whereas  $W$  is the wind tunnel width.

## Chapter 5

# GOVERNING EQUATIONS, TURBULENCE MODELS AND CFD CONCEPTS

### 5.1 INTRODUCTION

Due to the large range of Mach numbers that needs to be covered, the high Reynolds numbers ( $\sim 10^6$ ), the large vortex shedding with oscillations of the order of the cavity depth and the extremely high frequencies that we are looking for [24], aiming for a DNS is just out of discussion, especially considering that no in-house software is used and the ANSYS commercial software does not include DNS type of solution. Therefore, one should resort to different turbulence models, either URANS, LES or hybrid models.

The following section presents the theoretical foundation of fluid mechanics, starting from the Navier-Stokes equations, passing through some general definition of the dimensionless numbers, and finally arriving at the description of the different turbulence models: the reader must refer to the references [41, 42, 43, 44, 45, 46] for a detailed discussion on their derivation and their implementation on commercial software.

### 5.2 NAVIER-STOKES EQUATIONS

To derive the Rossiter's mode numerically, the Navier-Stokes equations needs to be solved. Chu & Kovasznay [47] showed that the compressible NS (Navier-Stokes) equations are able to capture three modes: *vortical*, *acoustic* (the one we are interested in) and *entropy* modes (the latter being associated with thermodynamics effects). Therefore, by solving the compressible NS equations, and by properly monitoring some points of the domain, the acoustic feedback of the Rossiter's mode can be highlighted by watching at the pressure field. The afore-mentioned Navier-Stokes equations consists of a set of four equations, namely the **continuity equation** (equation 5.1) and **momentum equation** in each dimension (equation 5.2), as hereafter displayed:

$$\frac{\partial \rho}{\partial t} + \nabla \cdot (\rho \mathbf{u}) = 0 \quad (5.1)$$

$$\frac{\partial(\rho \mathbf{u})}{\partial t} + \nabla \cdot (\rho \mathbf{u} \times \mathbf{u}) = -\nabla p + \nabla \cdot \tau + \mathbf{S}_M \quad (5.2)$$

Where the  $\nabla$  operator denotes the gradient, whereas  $\nabla \cdot$  the divergence. In the momentum equations, a vectorial equation,  $\mathbf{S}_M$  indicates volume forces, whereas  $\tau$  denotes the stress tensor, defined as:

$$\tau = \mu \left( \nabla \mathbf{u} + (\nabla \mathbf{u})^T - \frac{2}{3} \delta \nabla \cdot \mathbf{u} \right) \quad (5.3)$$



The above set of four scalar equations cannot be solved, since five unknowns appear (pressure, density and three components of velocity). Therefore, additional equations are required. A new variable equation is introduced, the **energy equation**:

$$\frac{\partial \rho h_{tot}}{\partial t} - \frac{\partial p}{\partial t} + \nabla \cdot (\rho \mathbf{u} h_{tot}) = \nabla \cdot (\lambda \nabla T) + \nabla \cdot (\mathbf{u} \cdot \boldsymbol{\tau}) + \mathbf{u} \cdot \mathbf{S}_M + S_E \quad (5.4)$$

where  $\lambda$  is the thermal conductivity of the fluid and  $S_E$  energy sources within the domain. Note that the energy equation is just adding a new variable, the temperature. The problem is not closed yet, since there are six variables ( $p, \rho, u, v, w, T$ ) but only five equations. The final equation is given by the fluid model that one considers. For the purpose of this work, the **ideal gas** simplification will be assumed. Ideal gasses follow equation 5.5:

$$p = \rho R T \quad (5.5)$$

With  $R$  being the gas constant (for air  $R = 287 \frac{J}{kgK}$ ). Now the full set of equations is known, which takes also the name of **Navier-Stokes-Fourier** equations, since the energy equation considers the heat formulation of Fourier.

In the literature it is well-known that the NS equations can be simplified into the incompressible NS equations for flow cases with  $Mach < 0.3$ , which neglects the compressibility effects. This is not the case of this work, where the operating range goes from  $0.3 < M < 0.8$ . It's worthy to mention though that still in the literature some cavity acoustic cases have been analyzed using incompressible assumptions, mainly applied in low-subsonic regime.

For the scope of this work, volume forces and energy sources will be neglected ( $\mathbf{S}_M$  and  $S_E$  negligible).

### 5.3 DIMENSIONLESS NUMBERS

In the review chapter, the Reynolds number  $Re$  has already been mentioned multiple times. In a classic way, the Reynolds number is defined as:

$$Re = u \frac{L}{\nu} \quad (5.6)$$

With  $u$  and  $L$  being the *characteristic* velocity and length of the system and  $\nu$  the dynamic viscosity. In case of a flow within a pipe, the characteristic length is the diameter  $D$ , but in case of the cavity different Reynolds have been introduced in the literature. The first, and the most used, is the length-Reynolds number  $Re_L$ , referring to the length  $L$  of the cavity. It is defined as:

$$Re_L = U \frac{L}{\nu} = c M \frac{L}{\nu} \quad (5.7)$$

where  $c$  is the free-stream speed of sound (locally it might change due to compressibility effects) and  $M$  is the free-stream Mach number.

With depth-Reynolds number  $Re_D$  one refers to the cavity depth  $D$ , defined as:

$$Re_D = c M \frac{D}{\nu} \quad (5.8)$$

With width-Reynolds number  $Re_W$  one refers to the cavity width  $W$ , defined as:

$$Re_W = c M \frac{W}{\nu} \quad (5.9)$$

Finally, another definition of the Reynolds number refer to the momentum thickness, already defined in equation 3.8, and referred with  $Re_\theta$  (in the literature  $\theta$  is mostly used to indicate  $\delta_2$ ), and defined as:

$$Re_\theta = c M \frac{\theta}{\nu} \quad (5.10)$$

Note that often the values of  $Re_\theta$  are several order lower than the others: while  $Re_L$  is usually around  $10^6$ ,  $Re_\theta$  evolves around  $10^3$ . The definitions are conventional, and they are mostly used by authors to compare their experimental and numerical results. This means that they cannot be really used to

distinguish laminar or turbulent regime, since their values can be very low (for instance if the cavity length  $L$  is very low) but the incoming boundary layer can be highly turbulent. Their definition serves mostly to investigate the SPL under different Reynolds value.

Another dimensionless number, already mentioned numerous times, is the Mach number  $M$ . It is defined as:

$$M = \frac{U}{c} \quad (5.11)$$

With  $U$  being the flow-speed (in our cases it will mostly be the free-stream speed) and  $c$  the speed of sound. The latter is computed according to:

$$c = \sqrt{\gamma RT} \quad (5.12)$$

With  $T$  being the static temperature (expressed in  $K$ ),  $\gamma$  being the ratio between specific heat at constant pressure  $c_p$  and specific heat at constant volume  $c_v$  (for ideal gas,  $\gamma = 1.4$ ) and  $R$  being the gas constant.

## 5.4 INTRODUCTION TO RANS TURBULENCE MODELS

RANS (or URANS for unsteady simulations) are based on Reynolds decomposition:

$$\mathbf{u}(\mathbf{x}, t) = \bar{\mathbf{u}}(\mathbf{x}) + \mathbf{u}'(\mathbf{x}, t) \quad (5.13)$$

Where  $\mathbf{u}(\mathbf{x}, t)$  is the velocity at position  $\mathbf{x}$  of the domain (say  $\Omega$ ) at time  $t$ ,  $\bar{\mathbf{u}}(\mathbf{x})$  is the averaged velocity over time and  $\mathbf{u}'(\mathbf{x}, t)$  is the velocity fluctuation with respect to the mean  $\bar{\mathbf{u}}$ . Figure 5.1 graphically schematizes the three terms. The purpose of the RANS is to evaluate the the mean properties of the flow

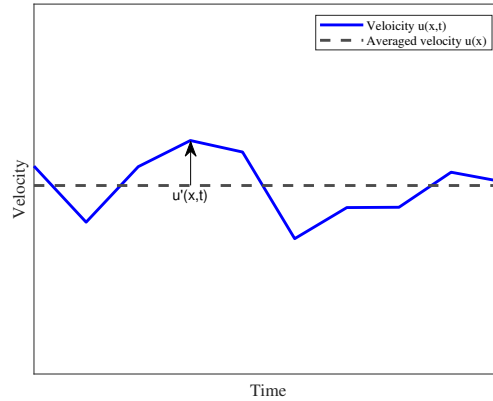


Figure 5.1: Graphical representation of the Reynolds decomposition.

instead of time history. Considering a point  $\mathbf{x}$  in the domain, with RANS turbulence models one has the averaged velocity over a certain time period  $T$ , which is much larger than the period of fluctuations of velocities, say  $T'$ . Being  $T \gg T'$ , flow perturbations are not going to be resolved in RANS. This is a key-point for URANS, and its worthy to be mentioned now: higher harmonics of the Rossiter mode are considered to rise from small eddies scales. Therefore, one might expect that by using URANS (Unsteady RANS) such modes will not be properly captured, no matter the mesh.

By applying the Reynolds decomposition into the continuity and momentum equation given in eqns. 5.1 and 5.2 and by doing some extra manipulations (see reference [41]), the averaged Navier-Stokes equations are obtained, shown in equation 5.14 and 5.15: note that the bar indicating the averaging was dropped and the vector sign is indicated with subscript  $i, j$ , referring to Einstein's vectorial notation.

$$\frac{\partial \rho}{\partial t} + \frac{\partial}{\partial x_j} (\rho U_j) = 0 \quad (5.14)$$

$$\frac{\partial \rho U_j}{\partial t} + \frac{\partial}{\partial x_j} (\rho U_i U_j) = -\frac{\partial p}{\partial x_i} + \frac{\partial}{\partial x_j} (\tau_{ij} - \rho \overline{u'_i u'_j}) \quad (5.15)$$

The averaging process of the Navier-Stokes equations introduces the term  $\overline{\rho u'_i u'_j}$  called the Reynold Stress Tensor. One of the way to express the Reynold Stress Tensor is according to Boussineq assumption, according to which the stresses are expressed as function of velocity gradients through the so-called **eddy viscosity** (or turbulent viscosity)  $\mu_t$ . The relation is given in equation 5.16:

$$-\overline{\rho u'_i u'_j} = \mu_t \left( \frac{\partial U_i}{\partial x_j} + \frac{\partial U_j}{\partial x_i} \right) - \frac{2}{3} \delta_{ij} \left( \rho k + \mu_t \frac{\partial U_k}{\partial x_k} \right) \quad (5.16)$$

Where  $k$  represents the *turbulent kinetic energy*, also expressed as:

$$k = \frac{1}{2} \overline{u'^2} \quad (5.17)$$

The different RANS turbulence models evolve around the definition of the eddy viscosity  $\mu_t$ .

### 5.4.1 THE $k - \varepsilon$ TURBULENCE MODEL

The  $k - \varepsilon$  turbulence model was one of the first two-equation turbulence model introduced. It's termed in that way since it is based on two transport equations: one for the turbulent kinetic energy and one for the **turbulent energy dissipation**  $\varepsilon$ , which is the rate of dissipation of the kinetic turbulent energy  $k$ . The two equations to be solved are:

$$\frac{\partial k}{\partial t} + \frac{\partial}{\partial x_j} (\rho U_j k) = \frac{\partial}{\partial x_j} \left[ \left( \mu + \frac{\mu_t}{\sigma_k} \right) \frac{\partial k}{\partial x_j} \right] + P_k - \rho \varepsilon + P_{kb} \quad (5.18)$$

$$\frac{\partial \varepsilon}{\partial t} + \frac{\partial}{\partial x_j} (\rho U_j \varepsilon) = \frac{\partial}{\partial x_j} \left[ \left( \mu + \frac{\mu_t}{\sigma_\varepsilon} \right) \frac{\partial \varepsilon}{\partial x_j} \right] + \frac{\varepsilon}{k} (C_{\varepsilon 1} P_k - C_{\varepsilon 2} \rho \varepsilon + C_{\varepsilon 1} P_{\varepsilon b}) \quad (5.19)$$

This is how the two equations are implemented in ANSYS, that's why different terms appear in the two equations to account for other effects.  $C_{\varepsilon 1}$ ,  $C_{\varepsilon 2}$ ,  $\sigma_k$  and  $\sigma_\varepsilon$  are constants.

$P_k$  is the turbulence production due to viscous forces, defined hereafter:

$$P_k = \mu_t \left( \frac{\partial U_i}{\partial x_j} + \frac{\partial U_j}{\partial x_i} \right) \frac{\partial U_j}{\partial x_j} - \frac{2}{3} \frac{\partial U_k}{\partial x_k} \left( 3\mu_t \frac{\partial U_k}{\partial x_k} + \rho k \right) \quad (5.20)$$

$P_{\varepsilon b}$  and  $P_{kb}$  are the buoyancy terms included in ANSYS CFX. Refer to the references to see their formulation [46].

In the  $k - \varepsilon$  turbulence model, only the turbulent kinetic energy  $k$  is explicitly derived, whereas the other scale-defining equation for  $\varepsilon$  is *modelled* in analogy to the  $k$ -equation using dimensional arguments. This of course leads to a non-rigorous definition for  $\varepsilon$  since some terms could be missing in the exact transport equation for  $\varepsilon$ . This can be noticed as well when one tries to derive the  $k - \varepsilon$  equation from the  $k - \omega$  equation (see later), which leads to the introduction of an additional term.

When adopting to refined meshes, the  $k - \varepsilon$  model, in order to resolve also the viscous sub-layer, needs some **damping functions**, which are applied to the  $C_{\varepsilon 1}$  and  $C_{\varepsilon 2}$  coefficients. Such damping functions are functions of the Turbulent Reynolds number  $Re_\tau = \rho k^2 / \mu \varepsilon$ . Even though these damping functions could provide a good resolution of the viscous sub-layer in any flow,  $k - \varepsilon$  model is not among the most used models. The main reason being that the  $k - \varepsilon$  is not really able to predict the separation points in flow with adverse pressure gradients, such as diffusers. Other models have been developed to solve this problem, such as the  $k - \omega$  turbulence model.

### 5.4.2 THE $k - \omega$ TURBULENCE MODEL

The  $k - \omega$  model provides a superior wall treatment, correctly predicting separation points, therefore overcoming the issue of the  $k - \varepsilon$  model.

$\omega$  is called the turbulent frequency, and it can be expressed as function of  $k$  and  $\varepsilon$ , according to:

$$\omega = \frac{\varepsilon}{C_\mu k} \quad (5.21)$$

With  $C_\mu = 0.09$  [46].

The transport equation for  $k$  is the same as the one shown in equation 5.20, provided that  $\varepsilon$  is expressed according to equation 5.21. The  $\omega$  transport equation is instead the following:

$$\frac{\partial \rho \omega}{\partial t} + \frac{\partial}{\partial x_j} (\rho U_j \omega) = \frac{\partial}{\partial x_j} \left[ \left( \mu + \frac{\mu_t}{\sigma_\omega} \right) \frac{\partial \omega}{\partial x_j} \right] + \alpha \frac{\omega}{k} P_k - \beta \rho \omega^2 P_{\omega b} \quad (5.22)$$

This turbulence model is also called the Wilcox  $k - \omega$  turbulence model. Despite the great improvement for the wall treatment, there is a limitation with this model which is referred in the literature as *free-stream dependence*. Basically, depending on the boundary conditions of  $\omega$  at the inlet, the results of the simulations might change a lot even by small changes of the boundary conditions. This is something that one wants to avoid. Such issue (free-stream dependence) is instead not a problem for the  $k - \varepsilon$  model. The idea that arose to overcome also this problem was a blend between  $k - \varepsilon$  and  $k - \omega$  models. The result is the SST turbulence model.

### 5.4.3 THE SST TURBULENCE MODEL

The basic idea behind the SST is to blend  $k - \omega$  turbulence model, to have a better wall treatment, with the  $k - \varepsilon$  model, to avoid the free-stream dependence. Basically, it's a hybrid model that applies  $k - \omega$  close to the wall,  $k - \varepsilon$  far from the walls and a blend of both of them in the transition.

The transport equation for  $\omega$  was derived by simple analogy with  $\varepsilon$  and dimensional arguments: despite  $\omega$  and  $\varepsilon$  being linked through equation 5.21, since their respective transport equations were derived separately and independently, when trying to derive one transport equation (say  $\omega$ ) starting from the other (say  $\varepsilon$ ), an additional term appears, that makes the two transport equation different.

More precisely, if one takes the  $\omega$  definition in equation 5.21 and substitutes that into the transport equation for  $\varepsilon$  in equation 5.19, the result is the following:

$$\frac{\partial \rho \omega}{\partial t} + \frac{\partial}{\partial x_j} (\rho U_j \omega) = \frac{\partial}{\partial x_j} \left[ \left( \mu + \frac{\mu_t}{\sigma_{\omega 2}} \right) \frac{\partial \omega}{\partial x_j} \right] + \underline{2\rho \frac{1}{\sigma_{\omega 2} \omega} \frac{\partial k}{\partial x_j} \frac{\partial \omega}{\partial x_j}} + \alpha_2 \frac{\omega}{k} P_k - \beta_2 \rho \omega^2 P_{\omega b} \quad (5.23)$$

The additional term is the one underscored in equation 5.23. Therefore, this term represents the difference between  $k - \varepsilon$  and  $k - \omega$ . The blending is achieved through a coefficient  $(1 - F_1)$ , with  $0 \leq F_1 \leq 1$  that premultiplies the underlined term and all the coefficients ( $\sigma_{\omega 2}$ ,  $\alpha_2$  and  $\beta_2$ ). The result is hereafter given:

$$\frac{\partial \rho \omega}{\partial t} + \frac{\partial}{\partial x_j} (\rho U_j \omega) = \frac{\partial}{\partial x_j} \left[ \left( \mu + \frac{\mu_t}{\sigma_{\omega 3}} \right) \frac{\partial \omega}{\partial x_j} \right] + 2(1 - F_1) \rho \frac{1}{\sigma_{\omega 2} \omega} \frac{\partial k}{\partial x_j} \frac{\partial \omega}{\partial x_j} + \alpha_3 \frac{\omega}{k} P_k - \beta_3 \rho \omega^2 P_{\omega b} \quad (5.24)$$

With the coefficients  $\alpha_3$ ,  $\beta_3$  and  $\sigma_{\omega 3}$  being defined as:

$$\phi_3 = F_1 \phi + (1 - F_1) \phi_2 \quad (5.25)$$

where  $\phi_3$  denotes the generic coefficient in the modified  $\omega$  transport equation shown in equation 5.24,  $\phi$  refers to the coefficient of the  $\omega$  transport equation (eqn. 5.22) and  $\phi_2$  represents the coefficient of the  $\varepsilon$  transport equation (eqn. 5.23): note that equation 5.23 starts from the  $\varepsilon$  transport equation, therefore the coefficients with subscript 2 refer to the  $\varepsilon$ .

From equation 5.25, it is clear that:

- if  $F_1 = 0$ , the  $k - \varepsilon$  model applies;
- if  $F_1 = 1$ , the  $k - \omega$  model holds;
- if  $0 < F < 1$ , a blend between  $k - \omega$  and  $k - \varepsilon$  is achieved.

Note that  $F_1$  is a scalar quantity: it assumes different values according to our position on the grid. To have a superior wall treatment ( $k - \omega$ ), this value is going to ve 0 close to walls, whereas 1 far from them (exactly to reduce the free stream dependence).

The turbulence model explained so far is called **Baseline k -  $\omega$**  model. It differs from the SST turbulence model slightly. In fact, the BSL  $k - \omega$  over-predicts wall shear stresses. That's why a *viscosity limiter* is

required, to prevent a turbulence build-up on stagnation region. The SST model defines the turbulent viscosity  $\mu_t$  as:

$$\mu_t = \frac{a_1 \rho k}{\max(a_1 \omega, S F_2)} \quad (5.26)$$

with  $a_1$  being a constant,  $F_2$  a scalar quantity (defined similarly to  $F_1$ ), and  $S$  being the magnitude of the shear strain. To this day, SST proved to be very reliable in a different series of cases: for this reason, it is employed in the steady simulations.

## 5.5 CFD CONCEPTS

The Navier-Stokes equations and the turbulence models needs to be solved, being non-linear, 3D, elliptic equations, they don't admit an explicit solution, unless for very specific flow cases under some assumptions. The only way to solve such equations is numerically. To do so, the NS equations must be discretized both in space and time. Different discretization schemes can be used depending on the order of accuracy one is searching for and depending on the computational resources. The discretization process relies on the mesh generation phase. The meshing phase consists in the discretization of the physical domain through hexagonal, quads or triangular elements: the equations are discretized on the nodes of the mesh in order to derive a system of equations that is afterwards solved iteratively. Depending on the refinement level of the mesh, solutions could be quite different. For this reason, a mesh convergence study is often required to guarantee that the solution that one has is no longer dependent on the mesh size. After validating the mesh, different simulations are performed and the results are critically analyzed to seek for eventual flaws in the model and in its setup.

For the scope of this work, two basic concept of CFD are discussed, namely the wall-functions and the CFL condition.

### 5.5.1 WALL-FUNCTIONS

The turbulent boundary layer can be mainly divided into three regions (see figure 5.2) [48]:

- A *log-log layer*, characterized by a wide range of turbulent scales, where the Reynolds number is high, meaning that the flow is dominated by inertial forces;
- A *buffer layer*, where the inertial forces are of the same order of viscous forces;
- A *viscous layer* (also referred as viscous sublayer), dominated by small turbulent scales which are dissipated due to high viscous forces.

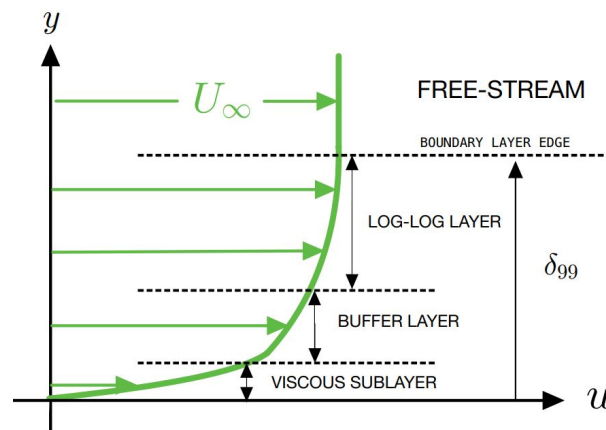


Figure 5.2: Turbulent boundary layer structure.

Being most engineering flow turbulent, to properly resolve the entire boundary layer a great refinement in terms of mesh is required close to the wall in order to capture the high gradient of velocity. This

increases of course the computational cost, which sometimes could be prohibitive. A dimensionless value is introduced to explain this, which is  $y^+$ . It is defined as:

$$y^+ = \frac{\Delta y_p}{\nu} \sqrt{\frac{\tau_w}{\rho}} \quad (5.27)$$

with:  $\Delta y_p$  being the distance between the solid boundary and the center of the first cell in the wall-normal direction and  $\tau_w$  the wall shear stress. The latter is defined as:

$$\tau_w = \mu \left. \frac{\partial u}{\partial y} \right|_{y=0} \quad (5.28)$$

The  $y^+$  tells how far the first cell center is from the solid wall: high value of  $y^+$  means that the first element is coarse, therefore that the boundary layer will not be completely resolved; low value of  $y^+$  means having a thin first element, thus a fully-resolved boundary layer. For instance the SST turbulence models requires a  $y^+ \approx 1$  to fully resolve the boundary layer.

As mentioned, high refinement makes the simulation last longer since more cells needs to be solved, and this sometimes isn't really possible. Therefore, one resorts to **wall-functions**: they are empirical relations that relate the velocity at the first cell to the  $y^+$ .

Before talking of the wall-functions, let's introduce the **near wall velocity**  $u^+$ , defined as:

$$u^+ = \frac{U_t}{u_\tau} \quad (5.29)$$

where  $U_t$  is the known velocity tangent to the wall at the distance  $\Delta y_p$ .

The wall-functions relates  $u^+ = u^+(y^+)$ , and there are different functions depending in which region of the turbulent boundary layer the first cell  $\Delta y_p$  falls in. The purpose of the wall-functions is to compute the correct boundary layer through these empirical relations without requiring the highly refined meshes.

There are different wall-functions depending on the value of  $y^+$ :

- If  $0 < y^+ < 5$ , then it means that  $\Delta y_p$  lies within the viscous sublayer, and that the following linear wall function applies:

$$u^+ = y^+ \quad (5.30)$$

- If  $y^+ > 30$ , then  $\Delta y_p$  lies within the log-log region, and that the wall function is the following:

$$u^+ = \frac{1}{\kappa} \ln(y^+) + C \quad (5.31)$$

with  $\kappa = 0.41$  (Von Karman's constant) and  $C$  being a log-layer constant, function of wall roughness.

- If  $5 < y^+ < 30$ , then the buffer layer is interested.

Note that in the last case of the buffer layer, even though there is a single wall functions that spans over the whole range of  $y^+$  covering also viscous sublayer and log-log region with a single function, the literature doesn't really recommend to end up in that region since wall functions are not so accurate there. The two laws are shown in figure 5.3:

### 5.5.2 CFL CONDITION

If one considers a linear, 1D, advection equation, as the one shown hereafter:

$$\frac{\partial u}{\partial t} + a \frac{\partial u}{\partial x} = 0 \quad (5.32)$$

Then, when applying an explicit time-stepping scheme, such as an explicit Euler scheme, in order to have a stable solution some considerations must be done on the time step  $\Delta t$ . For the aforementioned problem, the CFL condition must hold, which states that:

$$CFL = a \frac{\Delta t}{\Delta x} \leq 1 \rightarrow \Delta t \leq \frac{\Delta x}{a} \quad (5.33)$$

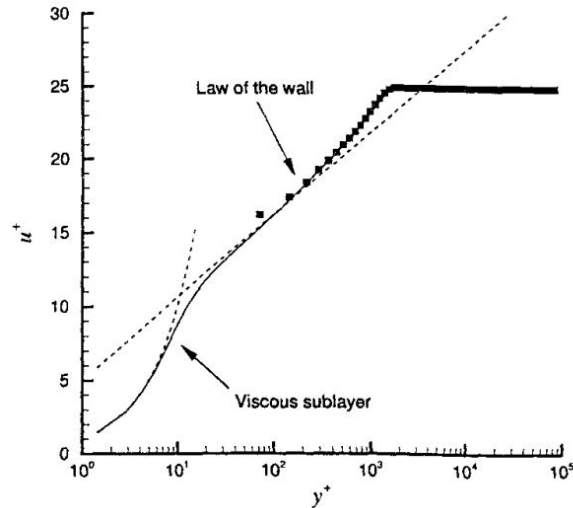


Figure 5.3: Wall functions in a  $\log_{10}(y^+) - u^+$  plane: the transition region for  $5 < y^+ < 30$  is not properly covered by the two wall functions. Furthermore, the two laws happens to intersect at  $y^+ \approx 11.06$ . Reference for the picture: [15].

Implicit time stepping schemes are instead unconditionally stable, which means that the solution will be stable for every time step  $\Delta t$ .

When it comes to the NS equations instead, one has 3D, elliptic, non-linear differential equations: although the CFL condition will be completely different from the one shown in equation 5.33, a similar formula will be used to estimate the CFL number locally in the domain. The modified formula will be the following:

$$\Delta t \leq \frac{\Delta x_{min}}{u} \cdot (1 \div 10) \quad (5.34)$$

Where the last term indicates that we are willing to accept higher values of CFL, up to 10: note that 10 as CFL for the linear 1D advection equation would bring unstable solution, but for the Navier-Stokes equations a CFL of 10 is generally accepted since, as mentioned, the non-linearity are strong and equation 5.33 doesn't really hold. Finally, having very strict condition on the CFL number would mean having a very low time step which makes computations much heavier for the same total time of simulation. Such section, though, serves more as a theoretical background: since ANSYS CFX implements implicit time-stepping, no constraints are limiting the  $\Delta t$ .

# Chapter 6

## STEADY STATE ANALYSIS

### 6.1 INTRODUCTION

As discussed in the methodology chapter, and as showed in figure 4.3, the wind tunnel is here considered without the cavity. The reason is to extract the velocity profile that is going to be used afterwards in the cavity section to perform the unsteady analysis. Figure 6.1 shows the wind tunnel with the two contraptions and the reference of frame (note the removed cavity dashed in gray). Figure 6.2 shows a

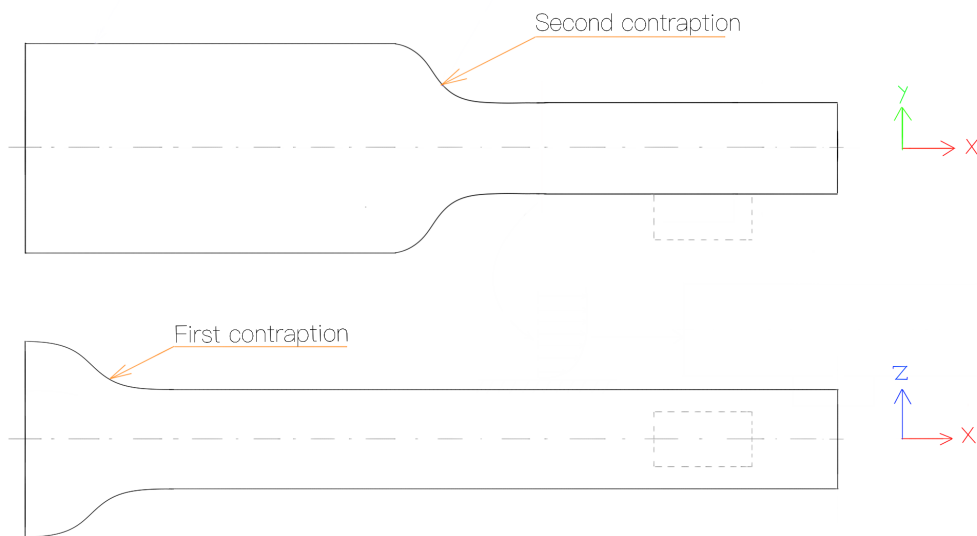


Figure 6.1: Wind tunnel used for steady analysis. Note that the dashed cavity is represented to state its position only, but in the simulations it is not considered.

more detailed view of the front part of the wind tunnel (excluding the first contraction) with the cavity section. The numbers are used to highlight the instrumentation used for the pressure measurements.



3	3 hole probe	Pitot tube.
5,6,7	PL11, PL12, PL13	Pressure taps at the wind tunnel bottom wall, just upstream the cavity.
12	PL3	Pressure taps at the end of the wind tunnel, mid-span, bottom wall.

Table 6.1: Description of the relevant instruments.

$T^o$ [K]	$p^o$ [kPa]
303	116.67

Table 6.2: Total temperature and pressure upstream the wind tunnel.

Although many pressure transducers are used, the one that are of interest for this work are mentioned in table 6.1. From table 6.1:

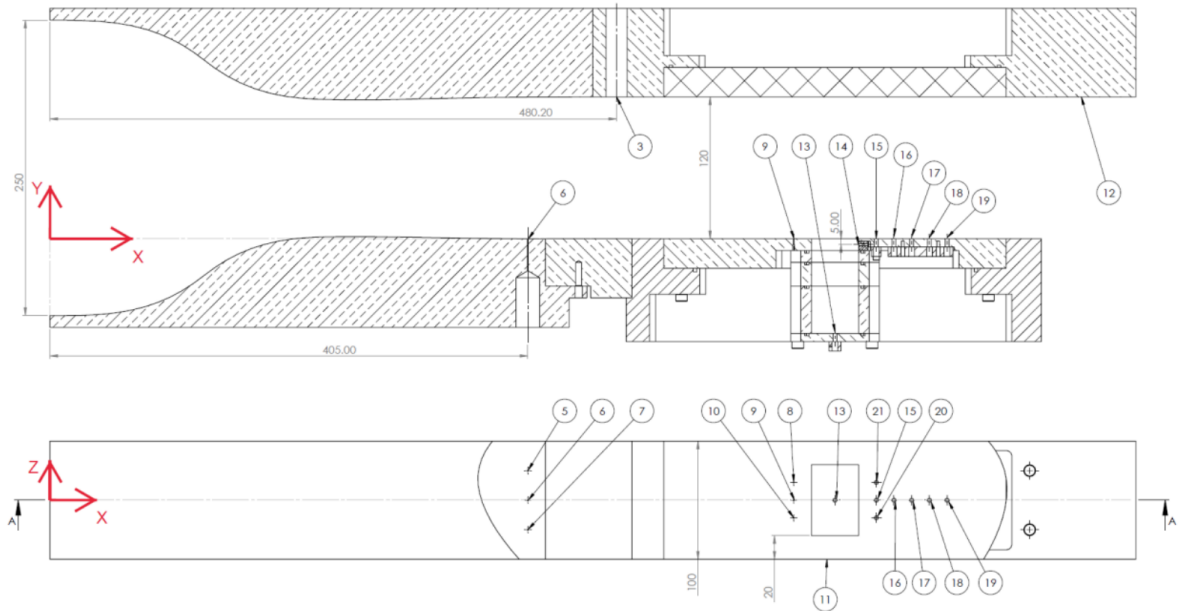


Figure 6.2: Technical drawing of the front part of the wind tunnel with the cavity.

- The Pitot tube is used for the total pressure profile measurements, of which the measurements are going to be compared with the numerical results for validation;
- The Static pressure taps upstream the cavity are measuring a static pressure, another measurement that can be used for comparison with numerical results;
- The pressure taps downstream the wind tunnel (PL3) provides the static pressure which is going to be used as outlet boundary condition for the setup.

Upstream the wind tunnel, total pressure and total temperature measurements are performed. These values are constant for all the operating points, meaning that when moving from  $M = 0.3$  to  $M = 0.8$ , the outlet static pressure is changing, as well as the speed of sound within the wind tunnel. Table 6.2 shows the two values: Given that the quantities are constant in time, then one has that the static temperature downstream the cavity (assuming adiabatic and inviscid wall), is:

$$T_{out} = \frac{T^o}{1 + \frac{\gamma-1}{\gamma} M^2} \quad (6.1)$$

$M$	$c$ [m/s]
0.3	345.8
0.4	343.5
0.5	340.5
0.6	337.0
0.7	333.0
0.8	328.5

Table 6.3:  $c = c(M)$ 

Where  $\gamma = 1.4$  for air and  $M$  is the Mach number. The speed of sound at the outlet of the wind tunnel is computed as:

$$c = \sqrt{\gamma RT_{out}} \quad (6.2)$$

According to equation 6.2, a table of speed of sound can be derived for different Mach numbers. The results are displayed in table 6.3. Although this table is now introduced, it will find application in the transient part.

The following chapter is structured in the following way: firstly, the chosen models and the boundary conditions are explained; secondly, the mesh convergence study is shown in which an operative mesh is defined; lastly, the results are compared with the experimental results will be discussed.

## 6.2 PHYSICAL MODEL

The governing equations necessary to solve the problem are the Navier-Stokes-Fourier (NSF) equations that have already been introduced in the previous chapter, in which one accounts for the enthalpy so to compute the temperature field as well. The equation of state to for the closure problem is given by the ideal gas equation, already showed in equation 5.5. As already known, the CFD equations will not be solved directly (DNS) but turbulence models will be adopted. The choice of the turbulence model is delicate: although adverse pressure gradients are missing, suggesting that a simple  $k - \varepsilon$  could be employed, a careful wall-treatment should be included. The reason for that is strictly related to the rectangular shape of the wind tunnel, where **corner flows** could develop. The corner vortices within rectangular channels typically exhibit a configuration of counter-rotating structures, whereby one vortex is generated close to the outer wall, traversing towards the inner wall, while the other vortex materializes near the inner wall, progressing towards the outer wall. Consequently, these vortices establish an intricate flow pattern and exert substantial influence over the spatial distribution of velocities and shear stresses within the channel. Figure 6.3 shows an example in which:

- In the left figure, the turbulence model is not able to capture the corner flows;
- In the center figure, the turbulence model is able to capture corners flow but not accurately in terms of position;
- In the right figure, the turbulence model is able to capture corners flow accurately (the right figure refers to a DNS).

For the purpose of this work, the following turbulence models have been tested:

1.  $k - \varepsilon$ , mostly for comparison;
2. RNG  $k - \varepsilon$ , suggested from the literature;
3. SST, since its the most used turbulence model and we aim at validating its application also for the given wind tunnel;
4. *GEKO*, a turbulence model developed at ANSYS which considers corner flows thanks to *corner correction coefficient*  $C_{CORNER}$ .

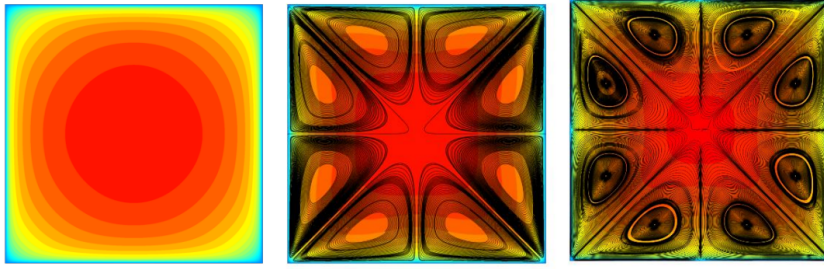


Figure 6.3: Corners flow prediction based on the turbulence model. Reference for the picture:[16].

Location	Type	Further details
Inlet	$p^o = 116.67 [kPa]$ $T^o = 303 [K]$	Turbulence intensity of 0.5% and 2mm length scale [49]
Outlet	$p = 109.1 [kPa]$	Static pressure all over the outlet
Walls	No-slip	Adiabatic walls

Table 6.4: Boundary conditions for the steady state analysis.

The choice of the turbulence model will come after the mesh independence, for which only SST is employed. Basically, for the mesh convergence study only the SST turbulence model is used with  $M = 0.5$  and, once the operating mesh is defined, only then the turbulence model will be defined. After such comparison, the definitive turbulence model is adopted with the operating mesh at all operating points.

The sets of CFD equations so far represents an elliptic problem. Therefore, boundary conditions must be ensured all over the domain. Given the setup already known, the boundary conditions are given in table 6.4: Note that the outlet pressure is given by the PL3 pressure tap shown in the experimental setup of figure 6.1 and mentioned in table 6.1: note that since the pressure tap is close to the wall, it is measuring a static pressure from the boundary layer (where velocities are negligible). The turbulence intensity is known to be lower than 1% from literature [49].

## 6.3 MESH INDEPENDENCE STUDY

Now, the mesh independence study is carried. As already stated, the SST turbulence model is used and all meshes are tested for  $M = 0.5$ . There are two main concerns when it comes to the meshing of the wind tunnel:

1. Isotropic cells;
2. Small value of  $y^+$  ( $< 5$ )

The reason for the isotropic cells is related to the corner flows. Isotropic cells (Aspect ratio  $\approx 1$ ) allows to carefully identify these flow patterns without much stretching, allowing for precise identification of their position. From the literature [50], these secondary flows seems to be related to gradients in the Reynolds Stresses: thus, highly stretched or skewed elements would provide not precise results. Still, as will be shown later, the magnitude (in terms of velocity) of these secondary flows will be relatively low and in this work we are not really interested in the exact position of these secondary flows therefore allowing to use a some more-skewed cells.

The small  $y^+$  is related to the boundary layer. Having small values of  $y^+$  allows to resort to a wall-resolving approach: the boundary layer close to the wall is fully resolved, including the viscous sub-layer. This is very important especially when moving afterwards to the unsteady analysis. When solving the unsteady case of the cavity, a  $y^+ < 5$  is suggested at the bottom wall of the cavity so that the separation of the boundary layer over the cavity and its transition to shear layer can be accurately predicted. By the moment that the velocity profile at the inlet of the cavity section is imposed as a boundary condition, to have a velocity profile resolved up to the viscous sub-layer one needs to solve the wind tunnel using

a proper  $y^+$ . In this way, the velocity profile that will be exported will be solved down to the viscous sub-layer, and the correct velocity profile will later be imported.

For the meshing, ICEM CFD is used. Different meshes were generated, all of which structured multi-block. The reason for a structured mesh relies mainly on the fact that the geometry is fairly simple and a good mesh can be achieved without that much of an effort. Moreover, convergence study is preferred on structured meshes. The meshes are:

- MESH-1, a very coarse mesh, which represents a first attempt;
- MESH-2, which uses a wall function with very high value of  $y^+$ , but same stream-wise refinement of MESH-1;
- MESH-3, refined along the stream-wise direction by halving the uniform spacing  $\Delta x$  but keeps the same wall-treatment of MESH-2;
- MESH-4, which improves significantly the near-wall refinement going this time for a fully resolved boundary layer with a  $y^+$  lying within the viscous sub-layer, but adopting the same stream-wise refinement of mesh MESH-3;
- MESH-5, same wall treatment of MESH-4 but halves the stream-wise refinement of MESH-3;
- MESH-6, same wall treatment of MESH-4 but halves the stream-wise refinement of MESH-5.

The difference in near-wall treatment refinement MESH-1, MESH-2 and MESH-4 are displayed in figure 6.4. Figure 6.5 shows the two differences in the stream-wise refinements. For further details, check table 6.5,

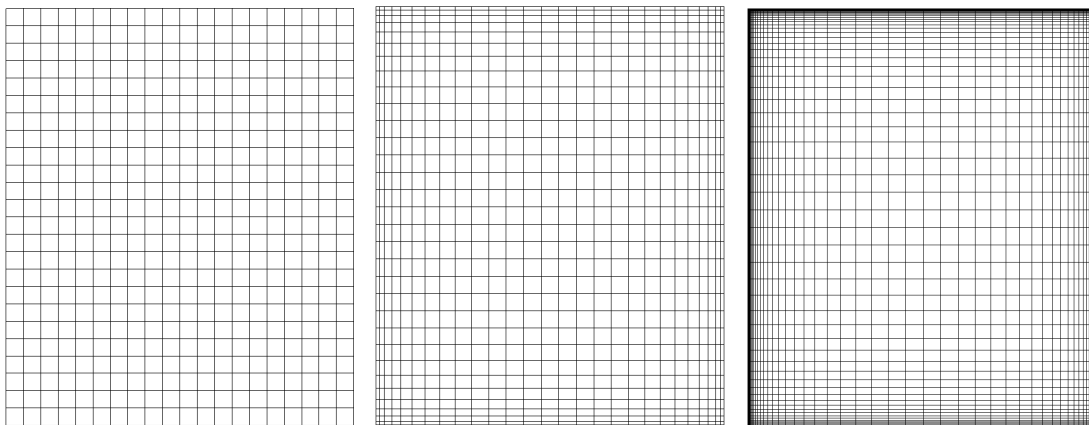


Figure 6.4: On the left, the outlet of MESH-1; on the middle, the outlet of MESH-2; on the right, the outlet of MESH-3. These three meshes represents the three different wall refinement that were adopted.

6.6 and 6.7.

	$N^\circ$ Nodes	$N^\circ$ Elements	$\Delta y_1 = \Delta y_{end}$	$y_{max}^+$	$R_{y,1} = R_{y,end}$
MESH-1	30K	33k	5mm	>500	2
MESH-2	52k	56k	1mm	400	1.5
MESH-3	103k	110k	1mm	400	1.5
MESH-4	759k	783k	$8\mu m$	4	1.1
MESH-5	1.51M	1.55M	$8\mu m$	4	1.1
MESH-6	3.03M	3.10M	$8\mu m$	4	1.1

Table 6.5: Mesh Details: part 1.

To better understand the parameters introduced in table 6.5,6.6 and 6.7, refer to figure 6.6. The process behind this mesh independence study was driven by results: total pressure profile are extracted

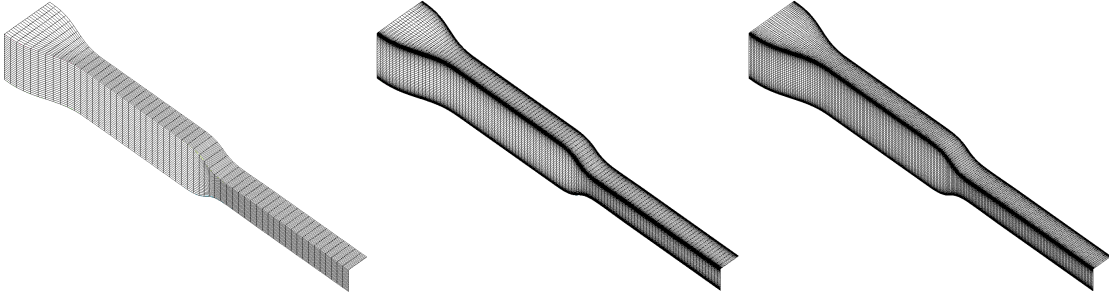


Figure 6.5: On the left, the stream-wise refinement of both MESH-1 and MESH-2; in the middle, the refinement of both MESH-3 and MESH-4; on the right, the stream-wise refinement of MESH-6.

	$N^\circ$ Nodes along x	Nodes along y	Nodes along z	$\Delta z_1 = \Delta z_2$
MESH-1	61	25	21	5mm
MESH-2	61	32	28	1mm
MESH-3	118	32	28	1mm
MESH-4	118	88	75	$8\mu\text{m}$
MESH-5	232	88	75	$8\mu\text{m}$
MESH-6	462	88	75	$8\mu\text{m}$

Table 6.6: Mesh Details: part 2.

as soon as the simulation finishes and results are immediately compared with results coming from previous mesh. Starting from MESH-1, a trial mesh, the initial idea was to refine the the mesh close to the wall, just by a little, and little difference was found (MESH-2). From this, the stream-wise direction was refined, by halving the step  $\Delta x$ : considerable difference was found (MESH-3). After such difference, the attention moved to the  $y^+$ : according to the consideration done before, a  $y^+$  of less than 5 was required, and this led to MESH-4 which has a superior wall refinement, both in terms of number of nodes and distribution of nodes (see the stretch ratio  $R$ ). After this, a non-very relevant difference was found, although the boundary layer this time was fully resolved. Since when halving the discretization step  $\Delta x$  lead to a shift of the pressure profile, the stream-wise refinement influence was further investigated in MESH-5 and MESH-6. A convergence of the pressure profile was noticed which was not that much different from the previous profiles.

In order to assess mesh independence, first one should run the simulations for long enough until they all converge to the correct value. Since the non-linear system of equation is resolved iteratively on CFX, one should use **monitors point** within the domain and see how properties (such as pressure value) change at each iteration. Since the pressure is usually the variable that takes longer to converge, the pressure was monitored at at mid-height section, exactly where the measurements are performed. In figure 6.7 the pressure value at the monitor point for each iteration is displayed: around iteration number 250, the solution have all converged. In figure 6.8, the total pressure profile are compared, whereas on figure 6.9 the velocity profile are compared: the results are extrapolated at **mid-section** ( $z = W/2$ , with  $W$  being the width). In table 6.8, some parameters are shown to highlight the mesh independence of the results, such as the free-stream Mach number, the boundary layer thickness, the displacement thickness, the momentum thickness and the shape factor  $H$ . Some of their definition, in case of a **wall-bounded compressible flow**, is shown hereafter (see [1]):

$$\delta_2 = \int_0^{\delta_{99}} \left( 1 - \frac{\rho u}{\rho_\infty U_\infty} \right) dy \quad (6.3)$$

$$\delta_3 = \int_0^{\delta_{99}} \frac{\rho u}{\rho_\infty U_\infty} \left( 1 - \frac{u}{U_\infty} \right) dy \quad (6.4)$$

$$H = \frac{\delta_2}{\delta_3} \quad (6.5)$$

	BL along x	$\Delta x_{max}$	BL along y	$\Delta y_{max}$	BL along z	$\Delta z_{max}$
MESH-1	BiGeometric	32mm	Biexponential	5mm	Biexponential	5mm
MESH-2	BiGeometric	16mm	Biexponential	5mm	Biexponential	5mm
MESH-3	BiGeometric	16mm	Biexponential	5mm	Biexponential	5mm
MESH-4	BiGeometric	16mm	Biexponential	5mm	Biexponential	5mm
MESH-5	BiGeometric	8mm	Biexponential	5mm	Biexponential	5mm
MESH-6	BiGeometric	4mm	Biexponential	5mm	Biexponential	5mm

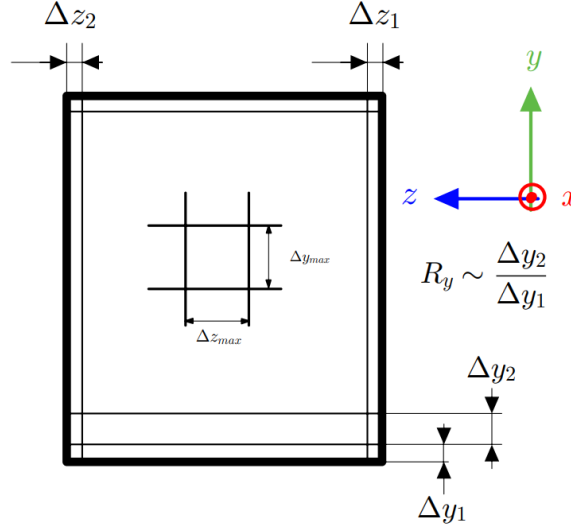
Table 6.7: Mesh Details: part 3. Note that BL stands for *Bunching Law*.

Figure 6.6: Meshing parameters displayed in a simplified way. The square in the figure refers to the OUTLET.

From table 6.8 the convergence of the results looks clearer. Note that in the wind tunnel the actual free-

	$M_\infty$	$\delta_{99}$	$\delta_2$	$\delta_3$ (or $\theta$ )	$H$
MESH-1	0.512	16.80mm	0.80mm	0.67mm	1.18
MESH-2	0.513	16.45mm	1.16mm	0.91mm	1.27
MESH-3	0.515	7.93mm	0.80mm	0.63mm	1.27
MESH-4	0.515	5.90mm	0.91mm	0.62mm	1.47
MESH-5	0.515	5.52mm	0.87mm	0.59mm	1.47
MESH-6	0.515	5.53mm	0.86mm	0.59mm	1.47

Table 6.8: Comparison between meshes-

stream Mach number that is measured at the measurement section is 0.505, which means that the relative error is less than 0.2% and the absolute error, in terms of velocity, is over-predicting the velocity profile of  $\approx 3$  m/s. Despite this, notice that the stream-wise refinement that was implemented in MESH-3 shows a great improvement in the boundary layer with the same wall refinement of MESH-2 (a drop of more than half in  $\delta_{99}$ ). Differently, notice that when moving from a  $y^+ = 400$  of MESH-3 to  $y^+ = 4$  of MESH-4, the change in boundary layer properties is not that consistent. In fact, when further refining along the stream-wise direction, no great benefit can be achieved in terms of improvement of the numerical results. Moreover, the shift of the free-stream total pressure with respect to MESH-6 goes from 200Pa for MESH-1 and MESH-2 down to 20Pa for MESH-3 and MESH-4 (MESH-5 differs of only 2Pa). Therefore, in order to keep the computational cost low with good accuracy in the results, MESH-4 was chosen as *operative mesh*.

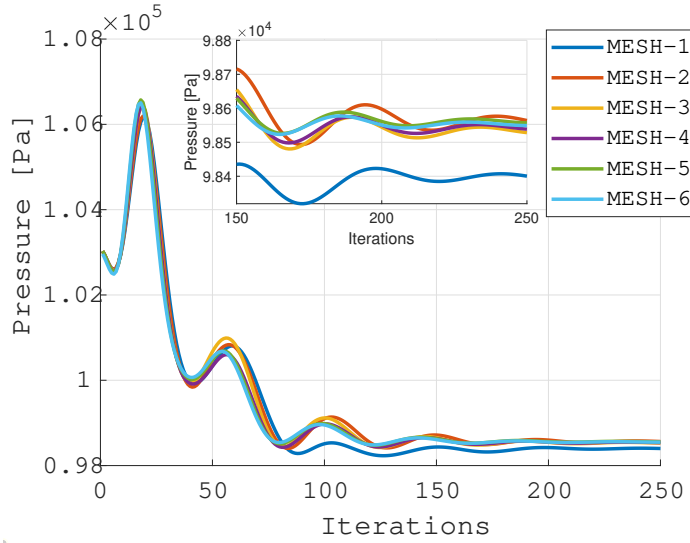


Figure 6.7: Pressure at monitor point.

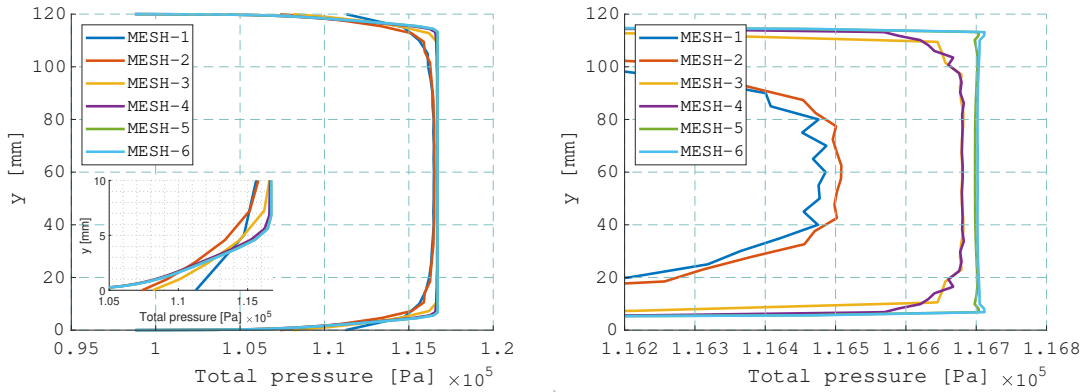


Figure 6.8: Total pressure profile: on the left, the overall profile with a small magnification close to the lower wall; on the right, a stretch is showed to highlight the stream-wise difference in free stream total pressure.

To this point, the mesh independence study is complete, though leaving open the discussion on the choice of the turbulence model. In fact, all simulations for the mesh independence study have been done with SST turbulence model. In figure 6.10 the numerical results are compared with the experimental measurements, obtained with a Pitot tube at the exact same position. From figure 6.10, two main things can be spotted:

1. The first is the shift in the free-stream total pressure (highlighted in the right picture with  $\Delta p$ );
2. The second is the blockage effect on the upper side (cleared in the left picture), that leads to an apparently thicker boundary layer.

Moreover, from experiments, the thickness of the boundary layer results to be approximately  $10\text{mm}$ , which is almost twice the measured value for MESH-6 ( $5.53\text{mm}$ ). Although the blockage effect cannot be really avoided due to the experimental setup, a further step will be now taken in order to address the difference in boundary layer thickness by trying out different turbulence model also according to some references from the literature.

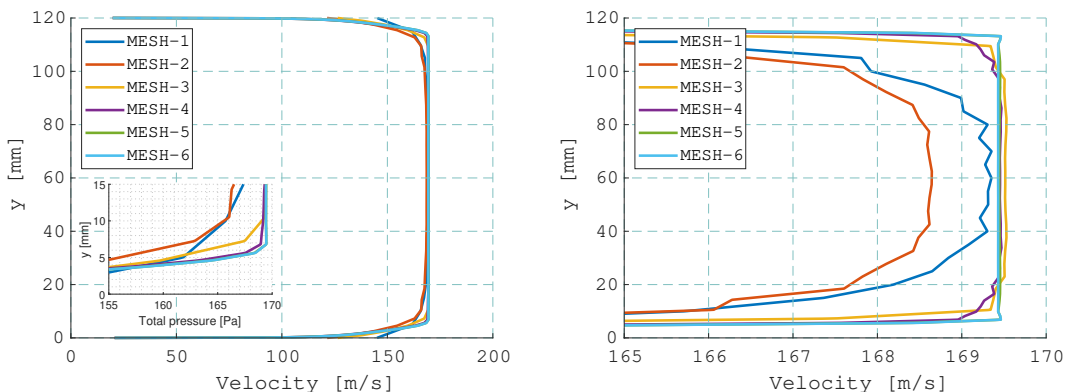


Figure 6.9: Velocity profile: on the left, the overall profile with a small magnification close to the lower wall; on the right, a stretch is showed to highlight the stream-wise difference in free stream velocity.

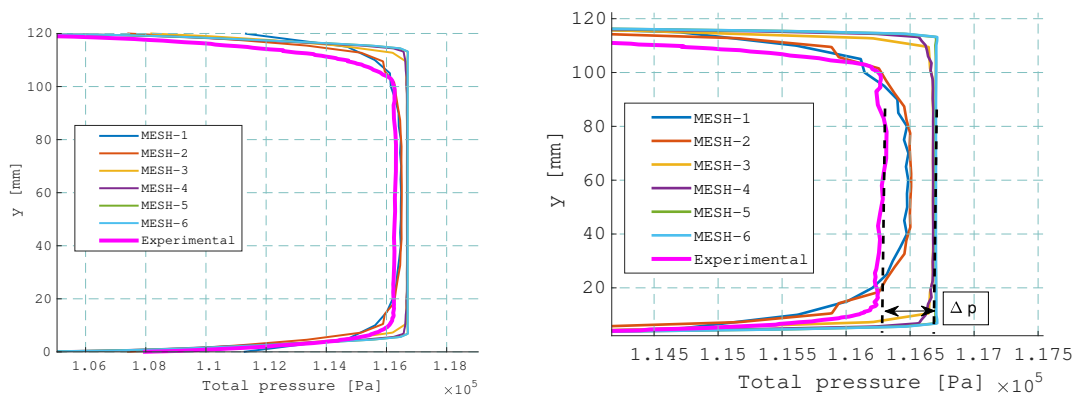


Figure 6.10: Comparison of numerical simulation with experimental results. On the left, the total pressure profile; on the right, a higher magnification.

## 6.4 INFLUENCE OF THE TURBULENCE MODEL

Given the appropriate mesh, the question of which turbulence model to choose arises. Considering now **MESH-4**, in figure 6.11 are shown the velocity contours for  $u$ ,  $v$  and  $w$ , whereas figure 6.12 provides with the streamline indicating the corner flows. Note that despite the corner flows occupy very large portions of the wind tunnel (main corner flow occupies one fourth of cavity area), the relative values of  $v$  and  $w$  that provoke the curvature of the mean flow are very low. Basically, when comparing  $v$  and  $w$  with  $u$  one can see that their values are much lower. As an example, if one was to compare the specific kinetic energy associated with  $v$  and compare it with  $u$ , the result in terms of ratio  $R$  of the two kinetic energies is:

$$R = \frac{1/2v^2}{1/2u^2} \sim \left( \frac{5 \text{ m/s}}{105 \text{ m/s}} \right)^2 \approx 2.3e-3 \equiv 0.23\%$$

For the scope of this section, different turbulence models were implemented. Although the results are quite similar in terms of contour of  $u$ ,  $v$  and  $w$ , the streamlines are changing quite a lot. Figure 6.13 shows the streamline in case of different turbulence models, respectively  $k - \varepsilon$ , RNG  $k - \varepsilon$  and *GEKO*. The reason for these three specific turbulence models are the following:

- $k - \varepsilon$  is the most dated turbulence model and although one might think that it behaves bad only with adverse pressure gradients, it also overpredicts Reynolds stresses thus, together with the wall function (always used by ANSYS independently of the  $y^+$ ), providing a significantly different results;



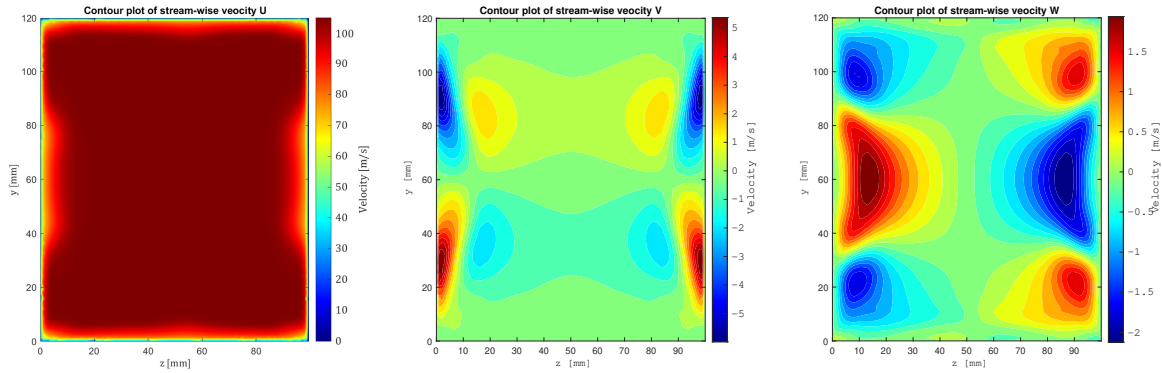
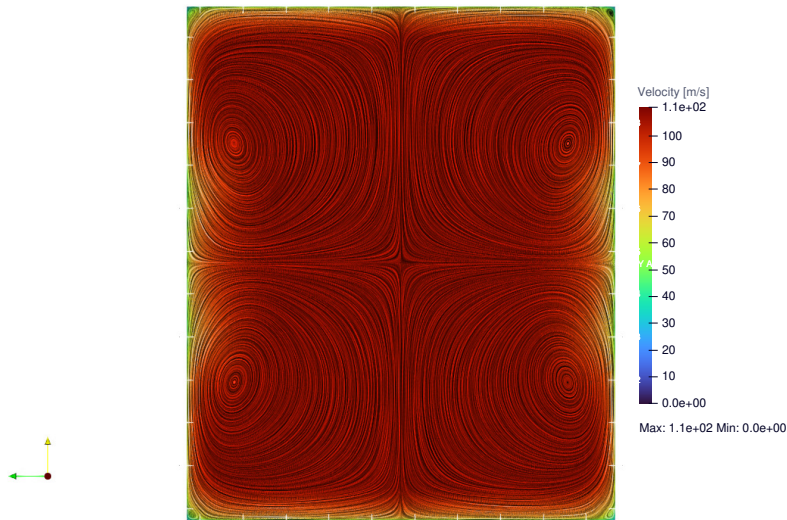
Figure 6.11: From the left, velocity contour of  $u$ ,  $v$  and  $w$ .

Figure 6.12: Streamline in case of SST.

- RNG  $k - \varepsilon$  is based on the re-normalization of exact transport equation for  $k$  and  $\varepsilon$ , which aims at providing better estimation of the eddy viscosity (the reason why this turbulence model was used is that it was tested in the literature from [51] and provided good results);
- Lastly, the GEKO turbulence model was used since it's a new turbulence model implemented at ANSYS (see [16]) which tries to overcome a series of problem of classical models by implementing correction coefficients (in this case the corner correction was activated with a value of  $C_{CORNER} = 0.9 \div 1.0$ ).

If looking at the three different figures, it's clear that  $k - \varepsilon$  and RNG  $k - \varepsilon$  show some similarity. Both have great secondary flows just attached to the upper and lower wall (the ones occupying one fourth of cross section). Different vortical structures can still be found: while for  $k - \varepsilon$  such structure consists in a two main recirculation regions (one on top and one on the bottom wall), for RNG  $k - \varepsilon$  it's possible to see four non-symmetric recirculation, with the right-side recirculations ( $z > W/2$ ) being almost double in size. Moreover, RNG  $k - \varepsilon$  presents small corner flows exactly at the corners, coherently with SST, but completely different from  $k - \varepsilon$  that doesn't show anything. Very differently, GEKO doesn't show these

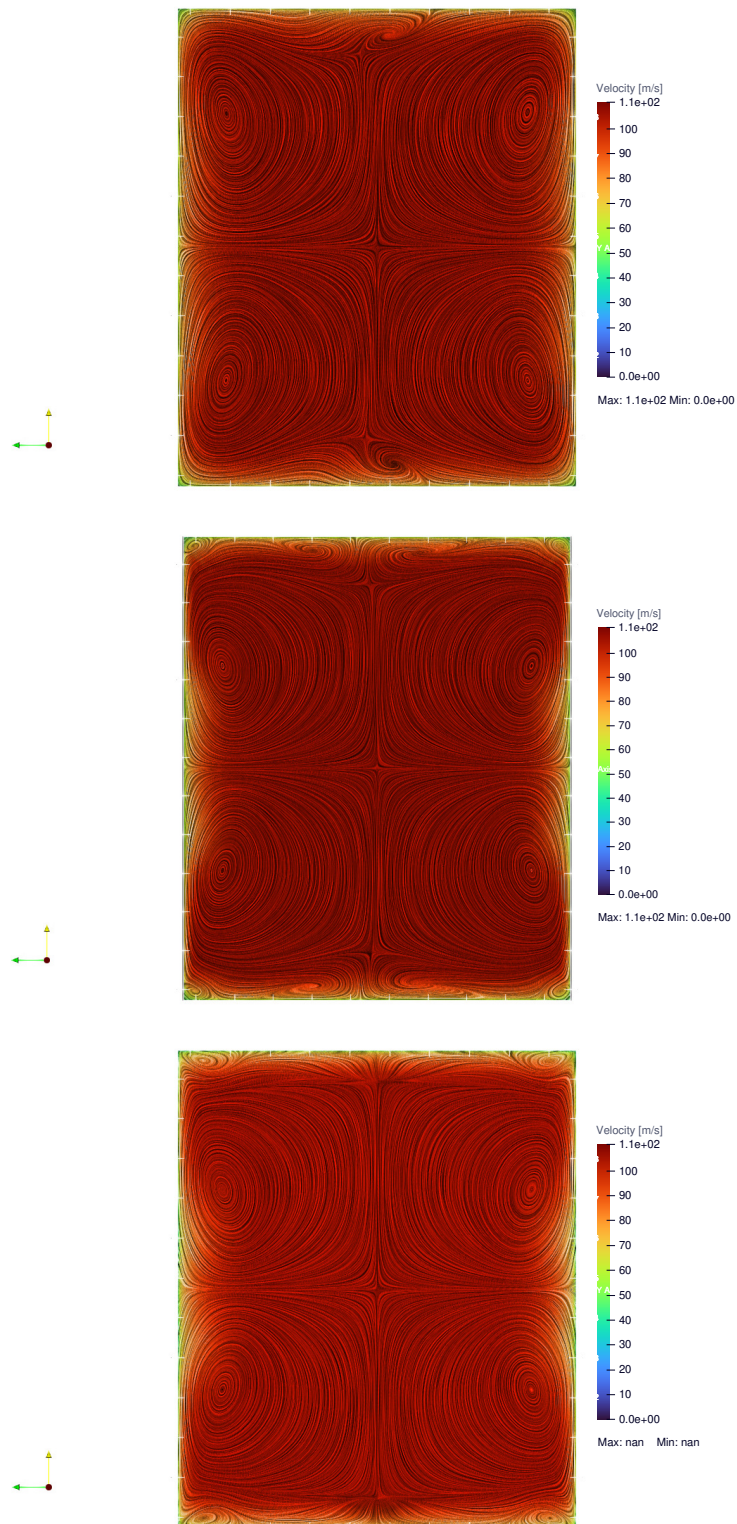


Figure 6.13: Streamline at the measurement section: from the top,  $k - \epsilon$ , RNG  $k - \epsilon$  and GEKO ( $C_{CORNER} = 1$ ).

MESH-4	$\delta_{99}$	$\delta_2$	$\delta_3$	$H$
SST	5.90mm	0.91mm	0.62mm	1.47
$k - \varepsilon$	6.72mm	0.90mm	0.65mm	1.40
RNG $k - \varepsilon$	5.76mm	0.86mm	0.61mm	1.40
GEKO $C_{corner} = 0.9$	6.12mm	0.91mm	0.62mm	1.46
Experimental	$\sim 10$ mm	NaN	NaN	NaN

Table 6.9: Comparison between turbulence models and experiments.

vortical structures, and the main secondary flows are reduced in size with respect to the SST ones, mainly because they leave space to the small corner flows very close to the walls which occurs to be bigger than SST, thus reducing the space available for the main secondary flows. The GEKO turbulence model that is suggest by the ANSYS engineers [43] for squared geometries seems to be the one that resembles the most the SST. Although we aimed at choosing the definitive turbulence model, such choice is not really easy. In figure 6.14 the three turbulence models are compared with the experimental measurements, and in table 6.9 more details are presented to highlight the differences. Although we are missing specific

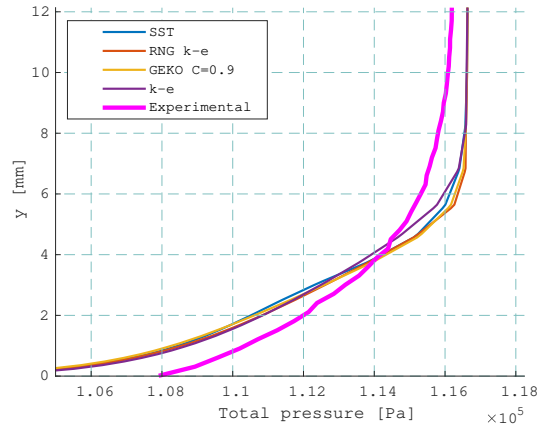


Figure 6.14: Comparing turbulence models with experimental measurements (in terms of total pressure profile).

measurements of  $\delta_2$  and  $\delta_3$  since only total pressure is measured, still a noticeable difference can be spotted with respect to the experimental data when it comes to the boundary layer thickness  $\delta_{99}$ . Therefore, the turbulence model choice is not significantly improving the comparison. In the next section, the results will be further analyzed.

	$\delta_{99}$	$\delta_2$	$\delta_3$
SST on MESH-4	5.90mm	0.91mm	0.62mm
Sigfrids (see [1])	NaN	1.33mm	0.94mm

Table 6.10: Comparison with previous PIV measurements [1].

## 6.5 RESULTS AND DISCUSSION

To this point, different meshes were tried out and different turbulence models as well. The results though don't seem to match properly with the experimental data. The first unresolved problem concerns the shift of the free-stream total pressure (of around  $400Pa$ ) which has been showed in figure 6.10. To this day, the reason for that shift seems to be related to a bad calibration of the Pitot tube, since theoretically speaking there shouldn't be changes in the free-stream total pressure. Basically, if the total pressure upstream at the inlet is  $116.67kPa$  (table 6.4), then such value should remain constant along the stream-wise direction: this is true for the numerical cases, but the four hundreds Pascal shift in the measurements suggests that the calibration procedure should be revised. Despite that, which can be simply solved by shifting manually the profile, the major problem remains the different thickness in the boundary layer. Having a good prediction of this value is in fact an important aspect of this work, not only to have a valid steady state setup to use but especially because the results of the steady state serve as input for the unsteady analysis of the cavity, and from the literature review chapter it has already been stated that the boundary layer plays a significant role concerning the dynamics of the Rossiter's mode both in terms of frequency and amplitude.

If one goes back to table 6.9, it is possible to see that the boundary layer in case of the pure  $k - \varepsilon$  turbulence model is thicker and that it gets closer to the experimental value: it has to be accounted though that the wall treatment is different in case of the  $k - \varepsilon$  method since ANSYS CFX uses a **scalable wall function** that limits the  $y^+$  so that it never goes below a threshold value of 11.06 which coincides with the intersection point of sub-viscous region and log-law region (see figure 5.3), leaving so the sub-viscous region unresolved. The RNG method seems to provide a results that is coherent, with a certain degree of error, with the SST value. The GEKO turbulence model instead differs a bit: this is related to the choice of the  $C_{corner}$  coefficient which has to be tuned iteratively. Such difference is intensified if we recall some literature references. César in his work [52] performed some steady state simulations at  $M = 0.85$  with a non-so different geometry leading to a boundary layer of  $5.58mm$ . Such result cannot be replicated due to different geometries, but when carrying a simulation with different boundary conditions to achieve a target Mach number at the out of 0.85, a very close value ( $5.62mm$ ) is reached meaning that the geometry itself has not that much of an impact. Thus, numerical simulations agrees when the same setup is used with slightly different geometries. Another experimental test carried by Sigfrids on the same wind-tunnel[1] showed quite different results. The results are resumed in table 6.10. As one can see, experimental results suggests always a thicker boundary layer. Note that Sigfrids used the same wind tunnel but different equipment (PIV measurements were done in the technical report [1]). Although the measurement section was not on the exact same location, still such a great difference in the boundary layer suggests that numerical setup does not represents the real one. To improve the agreement between numerical and experimental data, different approaches were tried out:

1. Extended Inlet;
2. Extended Outlet;
3. Imposing different turbulence intensity at the inlet;
4. Imposing an artificial total pressure profile through non-linear Blasius-like relation.

Note that the aforementioned approaches have the purpose to voluntarily change the numerical setup of wind tunnel so to have a better agreement with experiments: although the geometry is fairly simple and not great complication have been foreseen, it's important that one sticks to the experimental data of Hammer *et al* [24], which proved to be consistent with Sigfrids' PIV measurements [1].

### 6.5.1 EXTENDED INLET APPROACH

As the name suggests, the idea was to extend the inlet length so that the flow has more space to develop the boundary layer and is more likely to reach the desired boundary layer thickness at the measurement section. Figure 6.15 shows how this is achieved. In the preceding figure, three segments are aligned.

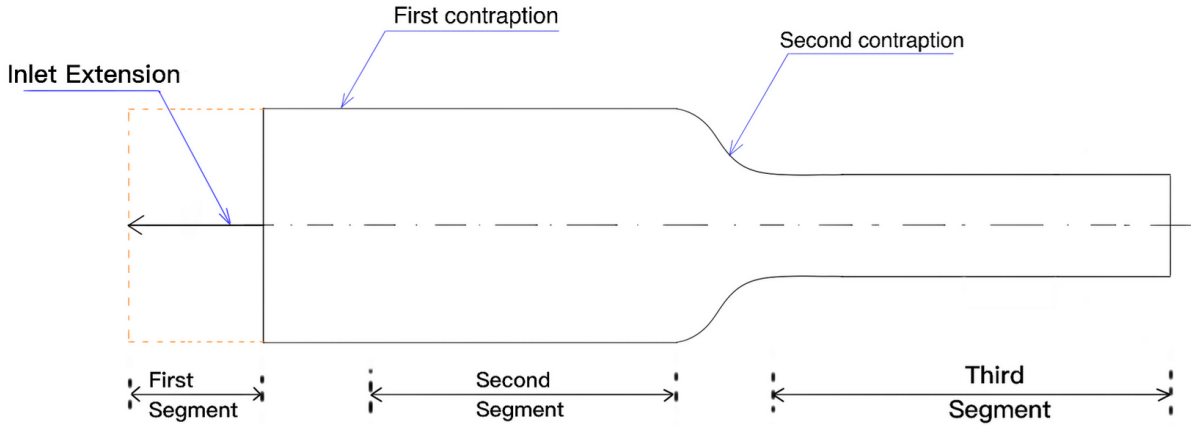


Figure 6.15: Inlet extension approach.

The scope of adding an extended inlet is to have a long enough *first segment* during which the flows can develop a certain boundary layer, which will be further enhanced by the *second segment* and *third segment*. Different simulations were carried at  $M = 0.5$ . Note that the boundary conditions that were used are exactly the same of 6.4. Technically speaking, using the same outlet pressure as the one shown in the table is wrong since assuming the same static pressure at the outlet means that we are neglecting pressure losses over the first segment, which in reality is not the case. Still, the same static pressure at the outlet is used to have a first grasp of the new boundary layer: eventually, if the results show an improvement in the  $\delta_{99}$ , then one could pursue an iterative procedure to have a reasonable outlet static pressure. Table 6.11 shows the results in terms of boundary layer thickness for different length of the first segment (the extended inlet). The boundary layer thickness  $\delta_{99}$  has been extracted as always at the measurement section and simulations have been done with SST turbulence model using MESH-4. The first segment had to be re-meshed of course, and the same uniform spacing  $\Delta x$  was used to be consistent with the existing mesh of the wind tunnel. From table 6.11, clearly many different lengths have been tried

$\Delta x_{in}$	50mm	100mm	150mm	200mm	250mm	500mm
$\delta_{99}$	6.0mm	6.0mm	6.13mm	6.13mm	6.13mm	6.13mm

Table 6.11: Boundary layer thickness  $\delta_{99}$  at the measurement section as function of the inlet extension length  $\Delta x_{in}$ . The operating conditions is  $M = 0.5$ .

but as it can be noticed the boundary layer thickness stabilizes at a certain point. More precisely, the first segment has small influence in the growth of the boundary layer thickness. When post-processing the results, it was pointed out that most of the boundary layer growth was achieved after the second contraction, after a great acceleration of the flow, leading to a substantial growth rate of  $\delta_{99}$ . Differently, the second segment (in between the two contractions) did not showed a significant boost in the growth of the boundary layer. The same applies to the first segment. Therefore, achieving the desired  $\delta_{99}$  at the measurement section requires an already thick boundary layer previous to the second contraction so that it can grow enough before the measurement section.

### 6.5.2 EXTENDED OUTLET APPROACH

This method was tried since one doubt arose when checking the velocity contour of the flow field. From figure 6.16, a magnification of the second contraction is showed: the simulation was done with  $M = 0.3$  according to SST turbulence model (see table 6.12 to check the boundary conditions). Clearly, the flow

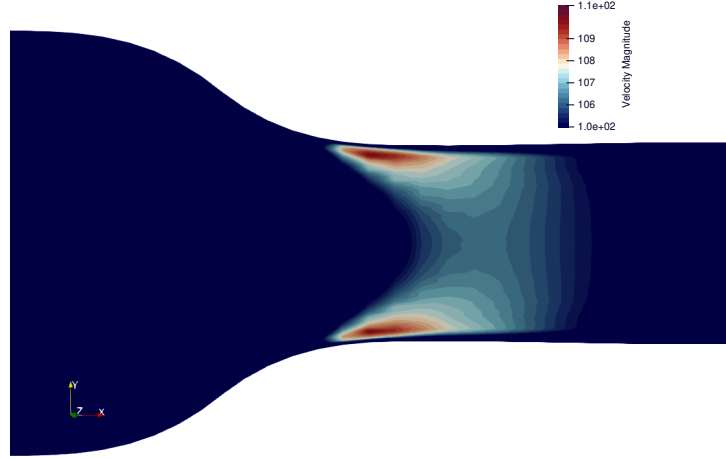


Figure 6.16: Magnification on the second contraction for  $M = 0.3$ .

Location	Type	Further details
Inlet	$p^o = 116.67 [kPa]$ $T^o = 303 [K]$	Turbulence intensity of 0.5% and 2mm length scale [49]
Outlet	$p = 109.1 [kPa]$	Static pressure all over the outlet
Walls	No-slip	Adiabatic walls

Table 6.12: Boundary conditions for the steady state analysis of wind tunnel at  $M = 0.3$ .

accelerates over the contraction but as it passes by, the flow starts decelerating. The speed reduction of around 2% (almost  $2m/s$ ) is close enough to the measurement section (see figure 4.3) and can potentially lead to wrong results when estimating the boundary layer thickness. For this reason, one might think that the outlet boundary condition is playing some important role forcing the within the domain to respect such conditions at the boundaries. Therefore, the outlet was extended in the same way it was done for the inlet, and the same approximated boundary conditions were used. The purpose is of course to define a path towards the experimental result and, if the path provides improvement, eventually investigate it deeper through an iterative procedure.

Figure 6.17 shows the outlet extension: note that again a uniform stream-wise spacing was used coherently with already existing mesh. MESH-4 was tried out and different outlet extensions were tried out. The results in terms of  $\delta_{99}$  are shown in table 6.13. Basically, the outlet extension had zero

$\Delta x_{out}$	50mm	100mm	200mm	300mm	500mm
$\delta_{99}$	5.90mm	5.90mm	5.90mm	5.90mm	5.90mm

Table 6.13: Boundary layer thickness  $\delta_{99}$  at the measurement section as function of the outlet extension length  $\Delta x_{out}$ . The operating conditions is  $M = 0.5$ .

influence. The outlet boundary conditions is not forcing the solution within the domain. The reason for that deceleration has to do apparently with a slight divergence of the wind-tunnel exactly after the second contraction, thus slightly decelerating the flow.

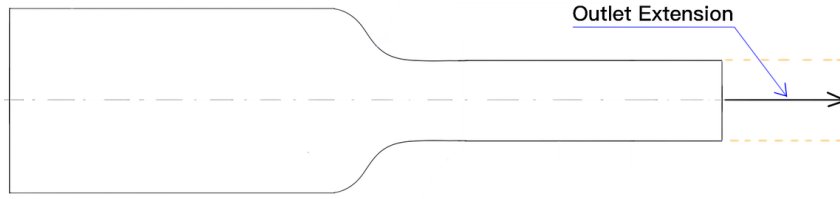


Figure 6.17: Outlet extension approach.

	$k$ [J/kg]	$\varepsilon$ [ $m^2/s^3$ ]	$\delta_{99}$ [mm]
LOW	$\sim 10^{-1}$	$\sim 10^2$	5.20mm
MEDIUM	$\sim 10^0$	$\sim 10^3$	5.2mm
HIGH	$\sim 10^1$	$\sim 10^4$	5.16mm
ENHANCED-1	$= 10^2$	$= 10^5$	7.56mm
ENHANCED-2	$= 2 \cdot 10^2$	$= 2 \cdot 10^5$	7.80mm
ENHANCED-3	$= 5 \cdot 10^2$	$= 5 \cdot 10^5$	8.80mm
ENHANCED-4	$= 10^3$	$= 10^6$	$\sim 10mm$

Table 6.14: Comparison between simulations with different turbulence intensity at the inlet.

### 6.5.3 TURBULENCE INTENSITY APPROACH

Another attempt in tuning the numerical results to be as close as possible to the experimental was tried out by manually imposing the turbulence intensity at the inlet. The turbulence intensity at the inlet was defined in terms of **turbulent kinetic energy** and **turbulent eddy dissipation** (basically the value  $k$  and  $\varepsilon$ ). By increasing the turbulence intensity at the inlet one is expecting to have a flow highly affected by disturbances such that the boundary layer is much thicker. The boundary conditions and the results (in terms of  $\delta_{99}$ ) are shown in table 6.14. Simulations are, again, carried at  $M = 0.5$ , with SST turbulence model on MESH-4. Another comparison is offered in figure6.18. The results seems quite promising, but

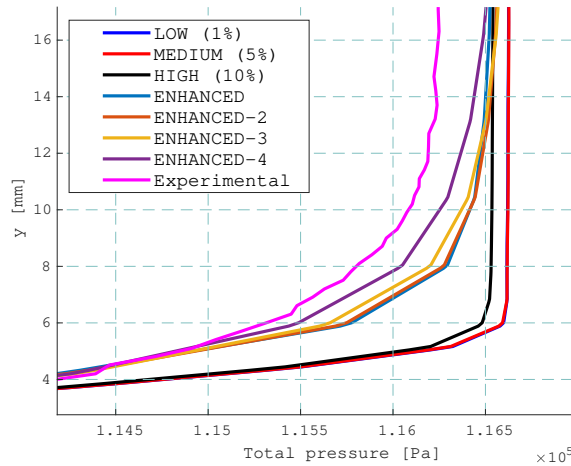


Figure 6.18: Comparison of total pressure profile for different cases of turbulence intensity.

if one tries to apply the definition of turbulence intensity and length scale according to CFX manual [46], then the results are, respectively, 69% and 30mm. They differ significantly if compared to 0.5% and 2mm measured by Vogt [49] on the same wind tunnel. Moreover, it's quite clear that having disturbances of

30mm is quite unusual, since they would be interacting with the main flow, over-predicting dissipation. When moving to the unsteady analysis, then, such dissipation will suppress any sort of acoustic feedback, therefore not showing any Rossiter mode. The result of this approach resulted thus in a fail.

#### 6.5.4 INLET PROFILE APPROACH

So far the results have always failed to compare with the experimental data. The fact that the experimental boundary layer is thick almost two times the numerical one suggest that there is something wrong in the physical setup. One important conclusion that can be derived from the extended inlet approach is that at the end of the second contraction the boundary layer starts to grow considerably, and that as long as the boundary layer previous to the second contraction is thin then there is not going to be enough room for the flow to grow its BL enough.

With that said, it has been hypothesized that exactly at the inlet, where the settling chamber ends, there could already be a mean velocity profile that is entering the wind tunnel, with a boundary layer  $\delta_{99} \neq 0$ . Such hypothesis fits the underlying statement that the boundary layer needs enough space to grow. The idea behind the extended inlet was to have an already developed boundary layer at the end of the first segment, which corresponds to the end of the settling chamber. The bad agreement with the experimental results provided by this approach were mainly related to the fact that, despite very long (0.75m) extended inlet, the boundary layer at the inlet was not thick enough. Starting from this results, a new approach was tested, which consisted in artificially imposing a velocity profile at the inlet with an arbitrary chosen boundary layer thickness. This approach can lead to an accurate results through an iterative procedure. The iterative scheme is presented in figure 6.19. More precisely, according to figure

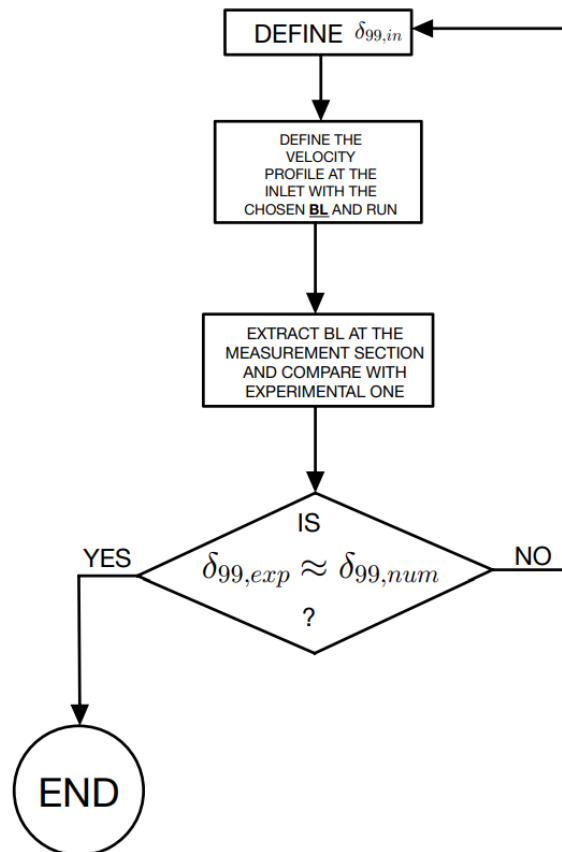


Figure 6.19: Flow chart of the iterative procedure to follow in order to get the right boundary layer at the measurement section.

6.19, if the numerical boundary layer at the measurement section is lower than the experimental one,



$\delta_{99,in}$	$\delta_{99}$	$\delta_2$	$\delta_3$
1.2mm	6.37mm	0.93mm	0.63mm
5.0mm	7.90mm	1.10mm	0.75mm
7.0mm	11.17mm	1.53mm	1.05mm
6.0mm	9.37mm	1.27mm	0.87mm
6.5mm	10.10mm	1.38mm	0.95mm
<u>Sigfrids (see [1]) / Hammer</u>	<u>10mm</u>	<u>1.33mm</u>	<u>0.94mm</u>

Table 6.15: Boundary layer properties for different  $\delta_{99,in}$ , with  $M = 0.5$ .

that the inlet boundary layer  $\delta_{99,in}$  should be increased, otherwise should be reduced.

The velocity profile that was used at the inlet was a Blasius-like velocity profile, derived according to a sinusoidal approximation. The reference formula is hereafter given:

$$u(y) = U_{\infty} \sin\left(\frac{\pi}{2} \frac{y}{\delta_{99,in}}\right) \quad (6.6)$$

There is a major problem with formula 6.6, that is the free-stream velocity at the inlet is not really known (no measurements of velocity have been done). What is known though is the average static pressure at the inlet  $p_{avg,in}$  and the free-stream total pressure ( $p_{\infty} = 116.67kPa$ ). Therefore, a total pressure profile can be imposed at the inlet, with a definition similar to equation 6.6. The Blasius-like total pressure profile that was assumed is depicted in equation 6.7:

$$p^o(y) = (p_{\infty}^o - p_{avg,in}) \sin\left(\frac{\pi}{2} \frac{y}{\delta_{99,in}}\right) + p_{avg,in} \quad (6.7)$$

Note that only the amplitude difference between free-stream total pressure and average static pressure at the inlet is multiplying the non-linear term. When  $y = 0$ , close to the wall, the velocity will be zero, and accordingly the total pressure will coincide with the average static pressure, whereas when  $y = \delta_{99,in}$ , exactly on the boundary layer limit, then the total pressure goes back  $p = p_{\infty}^o$ . Note that the boundary layer thickness is defined according to velocities, so this definition used here is apparently non coherent: still, it serves as first approach to define an inlet profile. Future work might be based on testing different profiles according to different suggestion from the literature. Figure 6.20 shows the difference in approach between the simulations carried so far (figure a) and the new simulations with the imposed profile (figure b). The new simulations are carried again with  $M = 0.5$ , SST and MESH-4, but with the modified inlet

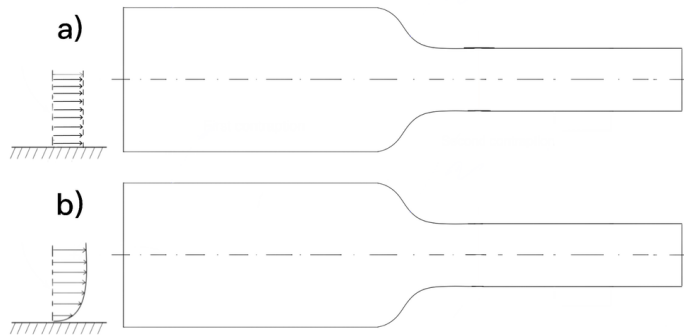


Figure 6.20:

- a) Total pressure at the inlet is constant
- b) Total pressure at the inlet follows a profile.

boundary condition. The results are displayed in table 6.15, along with some experimental data. Figure 6.21 compares the boundary layer properties with respect to the inlet boundary layer thickness. From

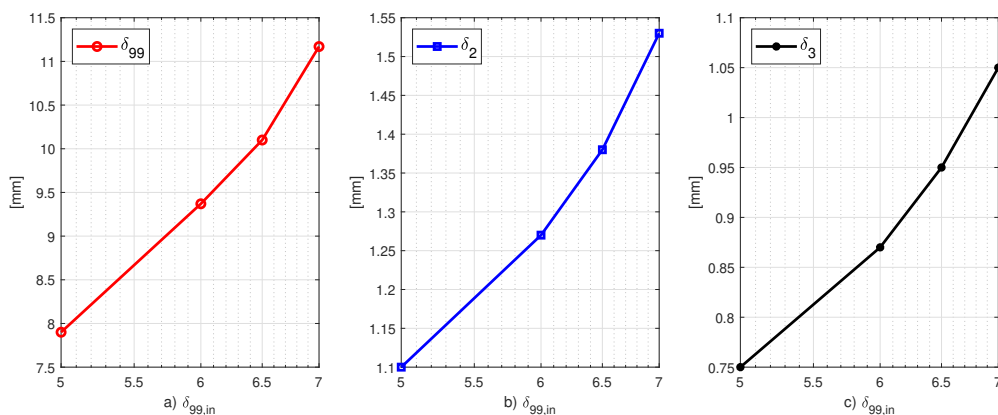


Figure 6.21: Expressing boundary layer properties as function of the inlet boundary layer thickness.

table 6.15, a good agreement can now be found between experimental data and the numerical one when the boundary layer in input  $\delta_{99,in} = 6.5mm$ . This approach serves to compare boundary layer only, but still does not justify the shift in total pressure which, as stated, is more related to the instrumentation that was used. Moreover, one should remember that this method aims at "forcing" the numerical result to be closer to the experimental one. This doesn't mean that the approach is universally accepted, but it's just a path that we followed in this discussion. To have a even better comparison, in fact, one should use both the profiles (the simulated one and the experimental one) as input for the unsteady cavity analysis and check if the new unsteady results are the same. If not, then one might conclude saying that although the two profiles are coinciding, the physics and the dynamics of the physical system are not correctly reproduced in the numerical model. Figure 6.22 shows the streamline at the measurement section: clearly, if compared to a previous simulation carried without inlet boundary layer (see figure 6.12), four non-negligible vortical structure appears, two on top and two on the bottom. It's obvious now the reason why the boundary layer gets thicker: apparently, introducing a boundary layer at the wind tunnel inlet accelerates the growth of vortical structures close to the wall. When no boundary layer was present at the inlet, no vortical structures were present on lower and top wall: they were introduced only when RNG  $k - \varepsilon$  turbulence model was chose. Such structures should be kept in mind, since they might have a great influence on the unsteady analysis.

We conclude hereafter this section presenting the results for all operating points: outlet pressure is specified as the boundary condition (since it's the only parameter that is used) and other values boundary layer properties.

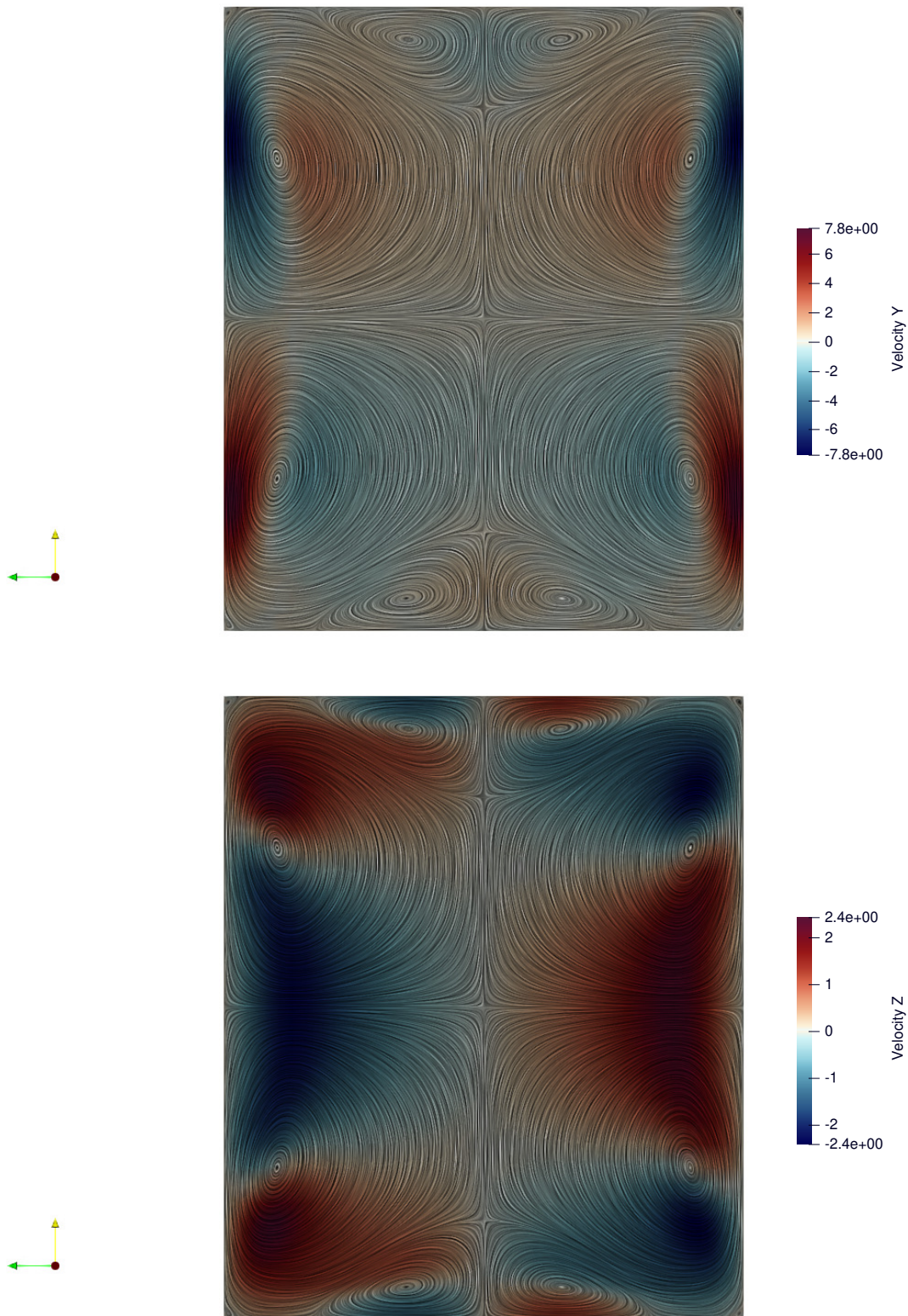


Figure 6.22: Contour plot of  $v$  and  $w$  component of velocity. Streamlines are overlapped.

## Chapter 7

# UNSTEADY ANALYSIS ON A 2-DIMENSIONAL CAVITY

### 7.1 INTRODUCTION

In the methodology chapter it has been explained why the unsteady analysis comes after the steady one. As said, now that the numerical velocity profiles have been extracted, it's time to use these velocity profiles as inlet boundary condition for the shortened domain and perform the unsteady analysis. Although the domain size was reduced by a lot by taking out the whole wind tunnel, performing 3D unsteady simulations is still prohibitive from a computational point of view. The simplified 2D geometry of the cavity overcome this issue. This simplified approach was used for two main reason:

1. Define a meshing procedure, and validate it through the mesh independence study;
2. Decide additional parameters with fast feedbacks.

When performing 2D unsteady analysis on a 70k element mesh for 30k time steps, the time required to solve the problem is around 20 hours (ANSYS CFX job with 20 partitions, i7-7700k and 32GB of RAM); when performing instead a 3D analysis with more than 1M elements over 10k time steps, the time required is around 10 days. For this reason, it was preferred to adopt a 2D model in order to tune the mesh and find the settings since it was much quicker to benchmark. The 2D cavity has the same characteristic geometric features of the one that should be validated, in terms of wind tunnel height, cavity depth, cavity length and downstream section, but the width is absent (one element thickness for CFX). The geometry is displayed in figure 7.1:

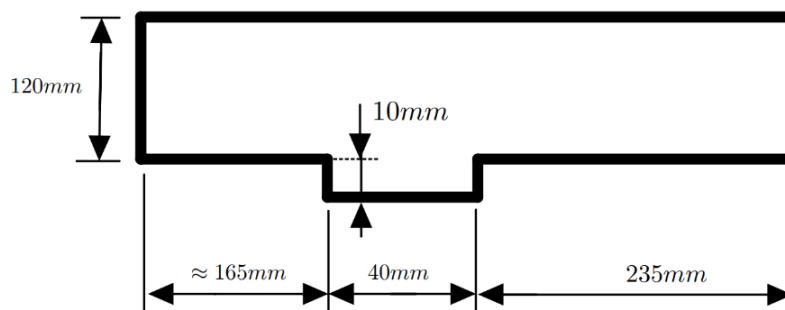


Figure 7.1: Geometry of the 2D cavity section.

## 7.2 PHYSICAL MODEL

Similarly to the steady state analysis, the governing equations are the NSF ones, in which one accounts also for the transport equation of enthalpy to consider temperature changes. The equation of state for the closure problem is given by the ideal gas equation. When it comes to the turbulence model, still a lot of studies are being done on this topic. For the scope of this work, the SST turbulence model is adopted. In the literature review chapter, it was stated that SRS (Scale Resolving Simulations) such as LES or hybrid techniques are able to accurately predict the intensity and frequency of tonal modes and intensity of the broadband noise whereas RANS models are able to predict only the former. Since this work objective is to validate the experimental results on Rossiter modes, which are tonal noises, a RANS model is used.

We want to point out that a SRS attempt was tried. On ANSYS CFX, the Hybrid model SBES (Stress-Blended Eddy Simulation) is available, which represents an improvement of an already known hybrid technique: DES (Detached Eddy Simulation). Although it seems to be the most suitable, also in terms of computational time, this direction resulted in a failure. Without going too much into the theoretical details (which one can find in [44], [45]), the hybrid SBES model blends LES Wale and SST turbulence model by applying a blending coefficient. The equation for the stress tensor is hereafter given:

$$\tau_{ij} = f_1 \tau_{ij}^{RANS} + (1 - f_1) \tau_{ij}^{LES} \quad (7.1)$$

Clearly, if  $f_1$  is equal to 1 then the stress tensor is computed accordingly to an entire RANS turbulence model, and if 0 then it's going to be computed accordingly to an LES. The way this  $f_1$  function is implemented, though, is secretary to ANSYS. Therefore, it was not really possible to understand how to properly apply this turbulence model. Many attempts were done trying to utterly refine the mesh, but it turned out that the  $f_1$  value was equal to 1 all over the domain, therefore solving the problem using only SST. For this reason, we decided to not spend more time on this direction and to switch completely to the standard SST.

The sets of NSF equations represents an elliptic problem: boundary conditions must be ensured all over the domain. Table 7.1 shows the boundary conditions: refer to figure 7.2 to see the different locations.

Location	Type	Further details
Inlet	Velocity Profile	Low turbulence and <i>non-reflective boundary</i> .
Outlet	Static pressure	Static pressure all over the outlet and <i>non-reflective boundary</i> .
Walls	No-slip	Adiabatic walls
Sides	Symmetry	It's an assumption.

Table 7.1: Boundary conditions for the unsteady analysis.

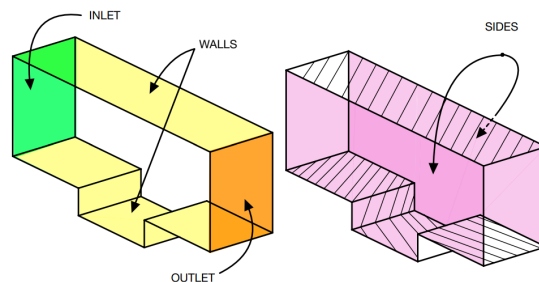


Figure 7.2: Schematic view of the boundary conditions.

Note that for the outlet, the static pressure that was imposed was coherent with pressure tap PL3, downstream the whole facility (wind tunnel and cavity section). Note also that the geometry seems to be 3D, but along the third dimension ( $z$ ), only one element is present.

### 7.3 MESH INDEPENDENCE STUDY

The purpose of this section is to try out different meshes and see if they are able to capture Rossiter mode.

Given the 2D geometry shown in figure 7.1, the meshing direction are only 2: the stream-wise direction and the depth-wise direction. For the depth-wise, basically the  $y$ -direction, from the literature, it is suggested to consider a  $y^+ \leq 1$  for aeroacoustics applications. Although this might seem reasonable, it is not very practical mainly for the CFL condition. By recalling equation 5.34, if  $\Delta x_{min}$  is extremely small and the velocity is much higher then the condition on the time step  $\Delta t$  are very prohibitive. In the literature, the trend has always been that of that of keeping the Courant less than 1. In this case, the approach is quite different: since for the scope of this work ANSYS CFX is adopted, which is an implicit solver, no constraints are present when it comes to the time step  $\Delta t$  (see reference [46]). Still, different meshes are going to be used also including wall functions with high  $y^+$  values to check the validity of the results. One of the mesh-constraints that is optimal is to keep elements with an aspect ratio as close as possible to 1 exactly at leading and trailing edge of the cavity. This allows in fact to avoid non-physical solutions, such as the one reported in figure 7.3. For what concerns the stream-wise direction, a suggested

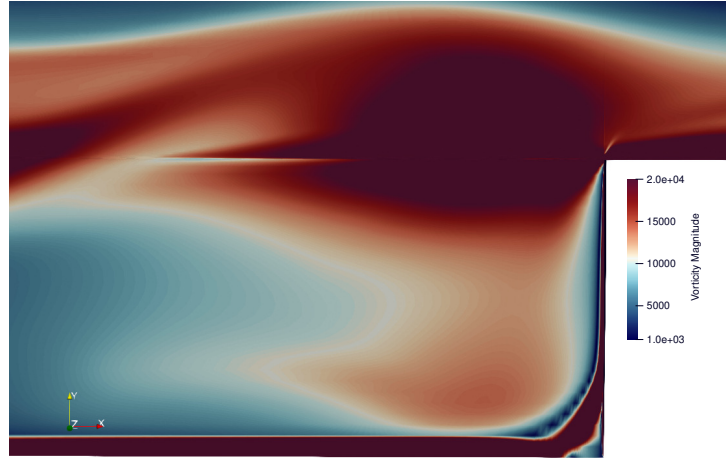


Figure 7.3: Non-physical vorticity field at leading edge of the cavity due to non isotropic elements (aspect ratio  $\sim 1$ ): the vortex roll-up is "compromised" by the error introduced by the mesh elements.

formula from GKN Aerospace was used, precisely:

$$\Delta x = \frac{\lambda}{30} \quad (7.2)$$

With  $\lambda$  being the *wavelength* of the acoustic wave that one wants to capture. The definition of wavelength is:

$$\lambda = \frac{c}{f} \quad (7.3)$$

Where  $c$  is the speed of sound and  $f$  is the frequency. Although the suggested formula seems pretty straightforward, some things must be pointed out. First of all, the spectrum of a FFT presents different frequencies. The idea is to choose a frequency that is high enough so that the mesh is able to capture it: as a consequence, smaller frequencies are also captured (this approach is theoretically, practically it's not guaranteed that a different mesh will capture the same physics). In case of cavity acoustics, if one remembers the Rossiter mode equation, the frequency varies with the operating point ( $M$ ). From the work of Hammer [24], the maximum frequency that was measured is around  $f = 5kHz$ . The second problem concerns the flow speed, which should be considered together with its direction. From this, equation 7.3 is modified into equation 7.4:

$$\lambda = \frac{c \pm u}{f_{max}} \quad (7.4)$$

To explain the  $\pm$  sign, one should consider the relative speed of the acoustic waves ( $c$ ) with respect to the flow speed ( $u$ ). If the waves are travelling counter-flow (against the flow), then the sign is negative, and this is exactly what happens in the upstream section. If instead the waves are travelling along with the flow, the sign is positive, exactly like downstream the cavity. Above the cavity, the the  $u$  velocity won't be considered. Clearly, when  $M = 0.8$ , the difference  $c - u$  gets very small, and the discretization step  $\Delta x$  can go down to micrometers, drastically increasing the number of elements. The current situation is the one shown in figure 7.4: This so far is the theoretical approach. From a practical point of view, instead,

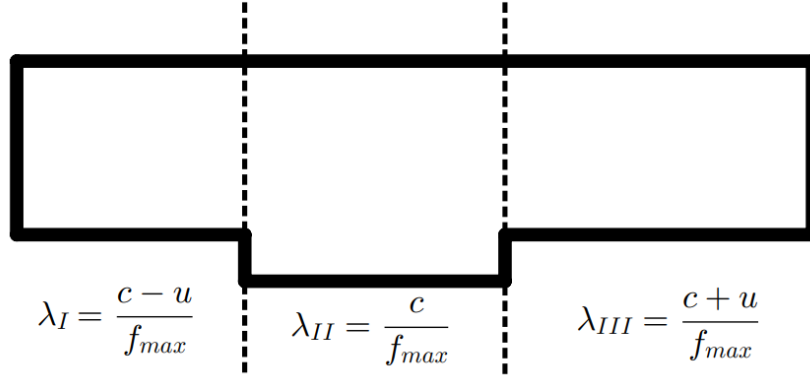


Figure 7.4: Different wavelengths according to the position: theoretical approach.

it was agreed with the company partner to choose another meshing technique. Instead of having a very fine stream-wise step  $\Delta x$  on the upstream section, the discretization step between cavity and upstream region was switched: in the new configuration, the very small  $\Delta x$  is adopted in the cavity (so to capture the complex dynamics of the flow) whereas the upstream uses the basic  $c/f_{max}$  formula. For simplicity, the same value has been considered for the downstream part. See figure 7.5 to better understand the changes. Note that the  $\Delta x$  won't be uniform because close to the cavity walls, in order to keep the aspect

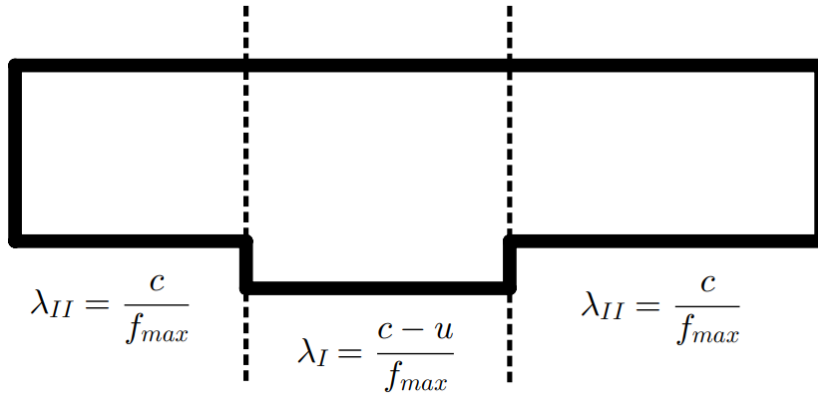


Figure 7.5: Different wavelengths according to the position: practical approach.

ratio of the elements as close to unity as possible, the space discretization should get denser. This of course increases the number elements, but it's a necessary trade-off that would keep the physics consistent (already displayed in figure 7.3). It was mentioned in the steady state chapter that the speed of sound is dependant on the operating point (see table 6.3): we arrived at the point where the ideal grid size  $\Delta x$  is dependant on the Mach both for the frequency and the sound speed. The approach that is pursued is to consider the operating point that would require the finest mesh and use it also for the least-restrictive cases. In this way less time is spent on the meshing procedure, although more time is going to be spent in computational time. Still along the  $y$  direction, after the consideration done on the wall treatment (the

$y^+$ ), it is important to define a maximum  $\Delta y_{max}$  in accordance with acoustic wavelength. Such value was imposed to be equal to  $\lambda_{II}/30$ , where  $\lambda_{II}$  is proportional to  $c$ . This is important since when changing the stream-wise step  $\Delta x$  one must change also the  $\Delta y$  step. In this way, having isotropic meshes in the volume allows the acoustic wave to travel without much distortion.

For the following mesh convergence study, different multi-block structured meshes were tested. They are respectively:

1. MESH-1-2D, which represents a trial mesh, with a stream-wise refinement four times bigger ( $\lambda/4$ ) than the one initially proposed ( $\lambda/30$ ), using a wall-function;
2. MESH-2-2D, a mesh that represents an improvement in the stream-wise direction if compared to MESH-1-2D, with the same wall-treatment of MESH-1-2D;
3. MESH-3-2D, which improves the wall-treatment of MESH-2-2D, but uses the same stream-wise refinement;
4. MESH-4-2D refines again along  $x$ , but uses again a wall function;
5. MESH-5-2D uses as stream-wise refinement the value suggested by the company partner ( $\lambda/30$ ), and keeps using a wall function.
6. MESH-6-2D uses a  $y^+ < 1$  with the suggested  $\Delta x$  value ( $= \lambda/30$ );
7. MESH-7-2D uses the same approach of MESH-6-2D but instead of using a Poisson distribution for the nodes, it operates a BiExponential distribution (denser closer to the walls).

The details of the meshes are given in table 7.2 and table 7.3. Note two main aspects:

1. As mentioned, the stream-wise refinement  $\Delta x$  is linked to the  $\Delta y_{max}$  value, so when the stream-wise component is refined then it's correct to expect an increase of nodes along  $y$ ;
2. Despite the isotropic elements in the volume, to avoid the non physical solutions showed in figure 7.3 one must ensure that the element close to trailing and leading edge must be isotropic as well (which is done by having  $\Delta x_{wall} = \Delta y_1$  and  $R_{y,1} = R_x$ ).

	$N^\circ$ Nodes	$N^\circ$ Elements	$\Delta y_1$	$y^+$	$R_{y,1}$	$\Delta x (= \Delta y_{max})$
MESH-1-2D	5k	7k	0.2mm	58	1.1	$\lambda/4$
MESH-2-2D	11k	16k	0.2mm	58	1.1	$\lambda/8$
MESH-3-2D	21K	327k	$2\mu\text{m}$	0.58	1.1	$\lambda/8$
MESH-4-2D	23K	34k	0.2mm	58	1.1	$\lambda/15$
MESH-5-2D	42K	63k	0.2mm	58	1.1	$\lambda/30$
MESH-6-2D	84K	125k	$2\mu\text{m}$	0.58	1.1	$\lambda/30$
MESH-7-2D	136K	203k	$2\mu\text{m}$	0.58	1.1	$\lambda/30$

Table 7.2: 2D Mesh Details: part 1.

In figure 7.6 are shown some of the meshes. From figure 7.6, clearly the upper wall of the wind tunnel has not the same refinement of the lower wall, where the  $y^+$  for MESH-7-2D goes below 1. This choice was dictated by the fact that imposing a greater refinement on the upper wall would increase the number of elements of the whole domain but with low effect on the overall physics that is being simulated since those elements (on the upper wall) are way too far from the cavity, at the bottom. Thus it's not really relevant refining the mesh in that region. Note also that MESH-7-2D and MESH-6-2D although similar have different nodes because different nodes bunching law was used: MESH-6-2D uses a Poisson type of distribution and MESH-7-2D a BiExponential.

With the mesh details provided, the different meshes were tried at  $M = 0.4$ . The idea of this mesh independence study is to extract the the pressure history during the whole simulation, to extract the data and to perform a Fourier Analysis on this signal: the values of the frequencies are used to determine if



	$N^o$ Nodes along x	Nodes along y	Nodes along y - Cavity	$R_x$
MESH-1-2D	89	24	17	1.1
MESH-2-2D	125	37	17	1.1
MESH-3-2D	190	48	19	1.1
MESH-4-2D	194	55	17	1.1
MESH-5-2D	236	85	35	1.1
MESH-6-2D	336	100	55	1.1
MESH-7-2D	426	145	35	1.1

Table 7.3: 2D Mesh Details: part 2.

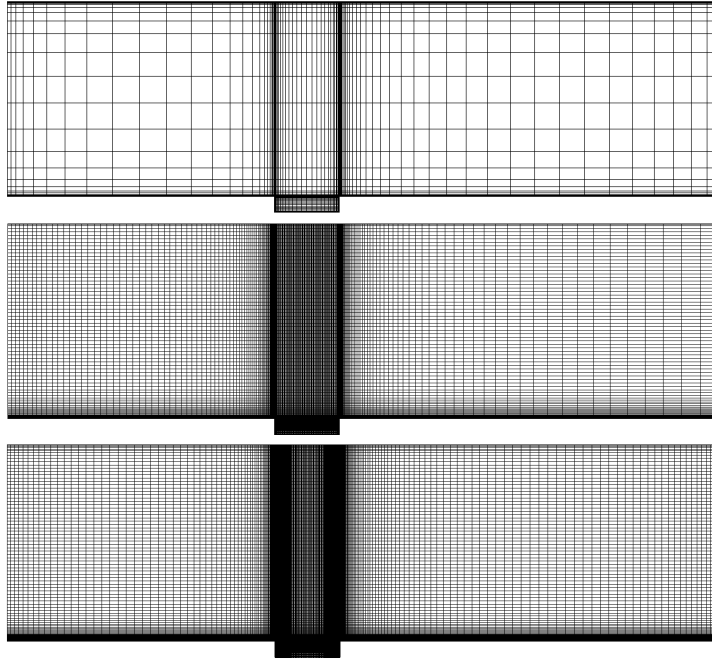


Figure 7.6: MESH-1-2D, MESH-5-2D and MESH-7-2D.

either the meshes have converged or further refinement are required. The monitor in question are displayed in figure 7.7. The reason for Monitor 2 is that it is located exactly at the exact same position of the kulite pressure transducer in the experimental setup (see Hammer *et al* [24]), thus allowing comparison with experiments. The Fourier Analysis (see **APPENDIX A - SIGNAL ANALYSIS** for the theoretical background) was done in **MATLAB**. When it comes to the FFT, the results are also affected by sampling frequency  $f_s$ , which for the numerical simulations coincides with:

$$f_s = \frac{1}{\Delta t} \quad (7.5)$$

where  $\Delta t$  is the time step that was used for the unsteady simulation. The effect of the sampling frequency is investigated in the following sections, whereas for the mesh independence study the idea was to pick twenty points for period of the highest frequency (associated with  $M = 0.8$ ). Since the highest frequency is  $5kHz$ , the time-step according to this definition happens to be  $\Delta t = 10^{-5}s$ . Theoretically, the longer the simulated time (overall unsteady time), the more accurate the results: this, however, can be tricky since simulations can get very long and this goes against the initial idea of the fast benchmarking. The simulations are carried using SST turbulence model, as previously mentioned.

Figure 7.8 shows the pressure evolution in time for all the meshes, and something interesting can already be noticed. From the time evolution, some comments can be done:

- Coarser meshes need more time to present a lock-in frequency if compared to finer meshes, the



Figure 7.7: Monitor points location.

latter requiring around  $10ms$  to reach a sort of fluid-induced resonance frequency;

- When coarse meshes are used along with wall functions (MESH-1-2D, MESH-2-2D and MESH-4-2D), the amplitude of the oscillations are up to two order of magnitude lower than the amplitude of the refined meshes, with resolved boundary layer;

The second comment is going to be clearer when looking at the FFT. For what concerns the first comment instead, it is important to implement it straight away in the FFT. The idea is to take the pressure evolution in time and cut-out the initial transient regime, before the oscillations settle in and get locked at a frequency (steady state-like regime). Getting rid in fact of the initial transient phase allows to get smoother FFT plots, highlighting only the necessary peaks. In figure 7.9 one can see the cleaner FFT compared to the more noisy one, depending on the transient phase. After this consideration, the total simulated time is set to  $120ms$  so that the first  $20ms$  could be excluded leaving therefore  $100ms$  to be post processed with the FFT. Table 7.4 schematized the setup of the simulations for this mesh independence study. The FFT for all the meshes are compared in figure 7.10. Referring to the FFT-plot just shown,

$M$	$\Delta t$	$f_s = 1/\Delta t$	$t_{tot}$	Samples	Monitor
0.4	$1e-05s$	$100kHz$	$0.12s$	$1e4$	Monitor 2

Table 7.4: General overview of the unsteady analysis.

it's clear that:

1. First, the very coarse meshes show low values of amplitudes, almost two order of magnitude lower if compared to more refined meshes;
2. Some frequencies are associated with peaks, meaning that the lock-in that was mentioned is occurring at those frequencies, therefore being coherent with what was said at the beginning (Mach 0.4 allows to see some frequencies);
3. Despite removing the initial transient phase, MESH-2-2D still shows a very noisy behaviour;
4. Meshes that uses wall functions show relatively lower values of amplitude if compared to fully resolved boundary layer meshes (the latter being MESH-3-2D, MESH-6-2D and MESH-7-2D).

From now on, using the same nomenclature that was used by Hammer *et al* [24], the frequencies associated with the highest peak are called **dominant**, the second highest instead **secondary** and the third highest as well **tertiary**. From figure 7.10, starting from MESH-4-2D, the dominant frequency are all the same ( $\sim 3kHz$ ), whereas for coarser meshes the dominant frequency is much lower. Exception made for MESH-3-2D that doesn't use a wall function and agrees with the result of the refined meshes. More interestingly, coarser meshes show are barely able to capture the higher frequency mode; symmetrically, the refined meshes present a noisy behaviour around the lower frequency mode, therefore not capturing any frequency. From this observations, being able to pick-up a mesh is not an easy task since the results are suggesting that the physics of the system are mesh-dependant. This is should not be the case, that's why a mesh independence study is performed. Figure 7.11 shows better the difference. Moreover, more refined meshes are able to spot the multi-harmonics of their dominant mode, which is not possible for

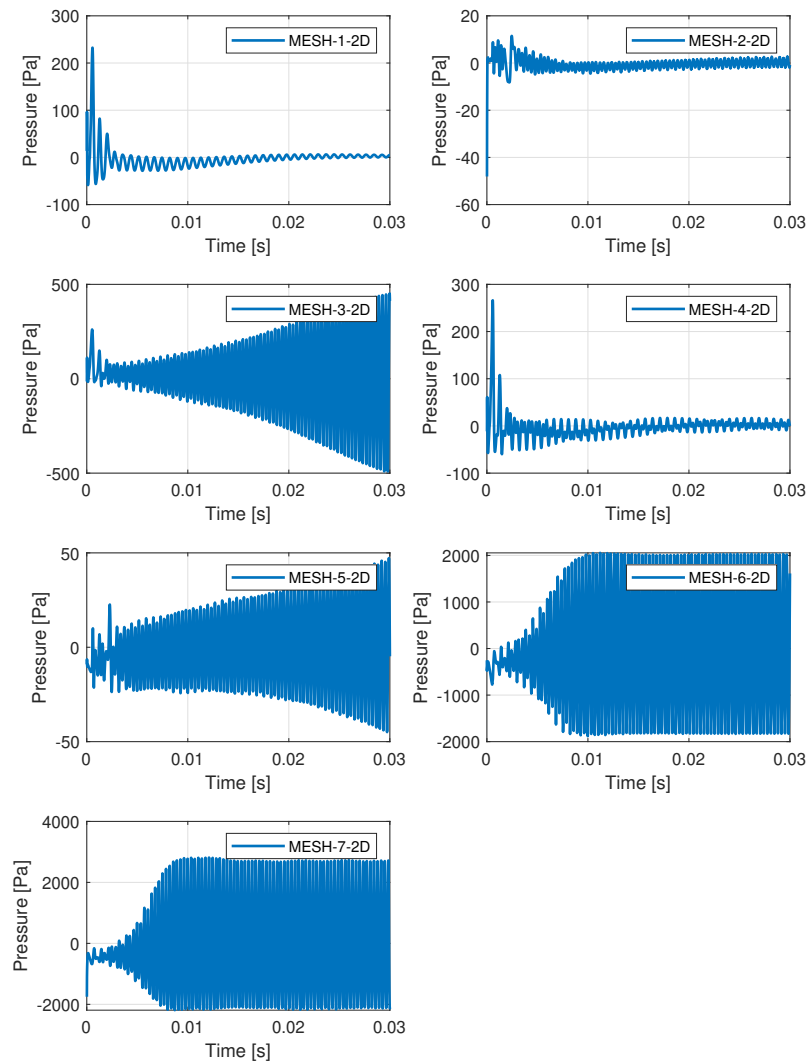


Figure 7.8: Time history of pressure at Monitor 2, for the different meshes, with  $M = 0.4$  and  $\Delta t = 1e-5s$ . Only the first 30ms are displayed. The mean value has been subtracted from each set of data.

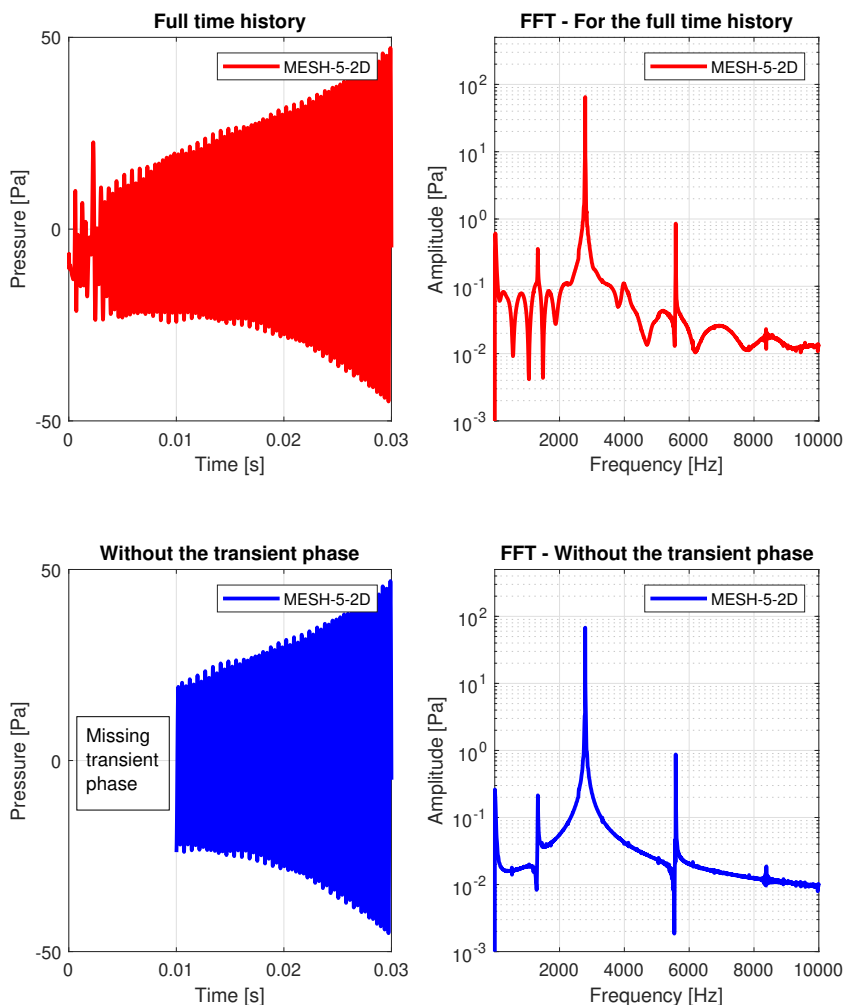


Figure 7.9: Comparing FFT with the transient phase and without it.

coarser meshes. To decide which mesh should be used, one can notice that when a wall function is used (MESH-1-2D, MESH-2-2D, MESH-4-2D and MESH-5-2D), the lower frequency mode is always captured. Wall functions are used whenever the meshes are too coarse, therefore they represent a model which tries to better represent the boundary layer without giving up in accuracy. Technically, a rigorous approach should aim at resolving the boundary layer and this is done when  $y^+ < 5$ . For this reason, the aforementioned meshes should be discarded. According now to the last meshes left, the most refined MESH-7-2D has also to be discarded due to the higher degree of refinement (the non-physical pressure and vorticity field appears, shown in figure 7.3). Between the two left-meshes, MESH-6-2D is used. The main reason being the stream-wise discretization step that coincides with the value suggested by the company partner. Nonetheless, one should keep in mind the result provided by MESH-3-2D since it could present a possible path for 3D unsteady analysis. In table 7.5 the overall results are presented as function of the mesh. Instead of using low frequency mode and high frequency mode, in the next figure (7.12) the Rossiter mode are introduced for  $M = 0.4$  along with the experimental results. Note that Rossiter formula does not provide amplitude, therefore only an horizontal straight line is presented. Discarding the coarse meshes could be a wrong idea since, apparently, their dominant frequency coincides with first Rossiter mode. That's not really the case though since experimentally, the first mode is not captured. Therefore

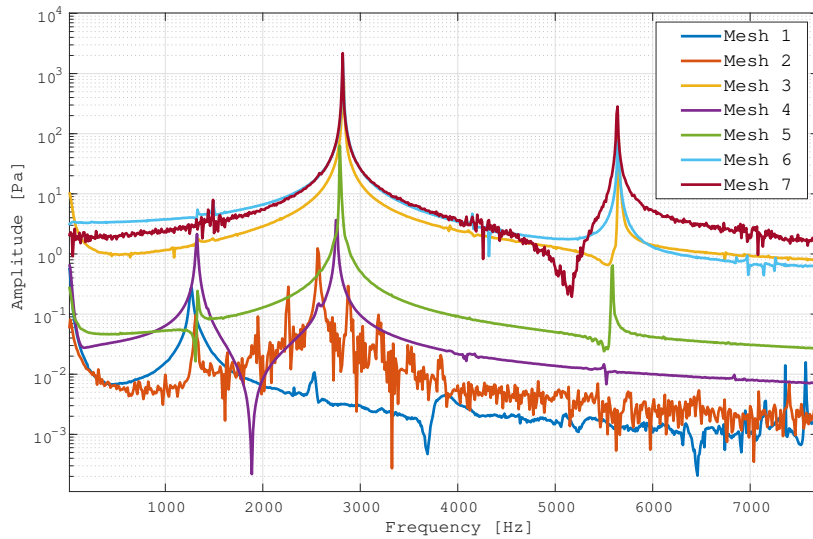


Figure 7.10: FFT for all the meshes. Details to compute the FFT are given in table 7.4.

	Low freq. $f_{low}$ [Hz]	Amplitude $f_{low}$ [Pa]	High freq. $f_{high}$ [Hz]	Amplitude $f_{high}$ [Pa]
MESH-1-2D	1270	0.27	NaN	NaN
MESH-2-2D	1312	0.1	NaN	NaN
MESH-3-2D	NaN	NaN	2830	838
MESH-4-2D	1325	2.15	2750	3.6
MESH-5-2D	1330	0.24	2790	63
MESH-6-2D	NaN	NaN	2820	1869
MESH-7-2D	NaN	NaN	2820	2186

Table 7.5: Results of the mesh independence study: low frequency stands for the lower frequency mode measured by coarser meshes whereas high frequency stands for the higher frequency modes measured by refined meshes.

discarding the coarse meshes is a good choice since they are predicting the wrong physics. The second Rossiter mode is accurately predicted by the refined meshes: actually, the mesh that was discarded seems has a 0% error when it comes to predicting the frequency: this is true if  $M = 0.400$ , but numerically and experimentally the measured Mach was  $M = 0.401 \div 0.403$ . For what concerns the discussion of the experimental data, refer to Hammer *et al* ([24]). In this work we focus the attention on how the simulated data differs from the experimental one. Difference can be spotted both in terms of amplitude and frequency. Difference in frequency can be addressed to the constant  $\kappa$ , ratio between vortex velocity and flow velocity, or to the simple limitation of the theoretical model. Difference in amplitude are instead more delicate. The reason being that from the simulation point of view, the unsteady simulation starts from a steady RANS. From an experimental point of view, the wind tunnel is progressively increasing it's speed ranging from  $M = 0.3$  to  $M = 0.8$ . According to the authors of [24], when transitioning across operating points, lock-in would occur with a specific frequency at a specific operating point and, such lock-in, would persist for a while before a new frequency takes over. New frequency's amplitude might therefore be affected by the previous modes. According to the authors, the experimental investigation of Rossiter mode was extremely sensitive: sometimes they would occur and others not. Using therefore the amplitude therefore is not recommended. Still in figure 7.12, the full circle and the dashed one represents respectively the second and third harmonics of the simulated second Rossiter mode. Table 7.6 shows the relative errors of the meshes with respect to the theoretical values and to the experimental one.

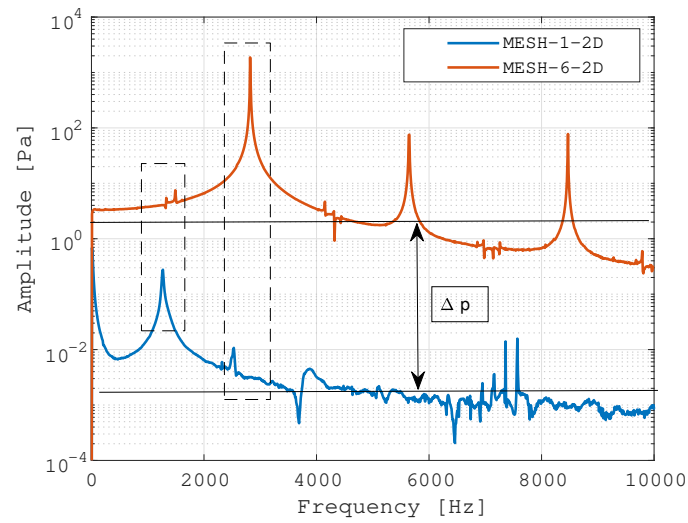


Figure 7.11: Comparing coarse with fine mesh: the dashed rectangles aim at showing the difference in the dominant mode, the  $\delta p$  aims at showing the difference in the average pressure amplitude.

	$f_{1,num}$ [Hz]	Rel. Error Rossiter 1 (= 1341Hz)	Rel. Error Experimental (=NaN)	$f_{2,num}$ [Hz]	Rel. Error Rossiter 2 (= 2790Hz)	Rel. Error Experimental (2647Hz)
MESH-1-2D	1270	5.2%	NaN	NaN	NaN	NaN
MESH-2-2D	1312	2.0%	NaN	NaN	NaN	NaN
MESH-3-2D	NaN	NaN	<b>Correct</b>	2830	1.4%	6.9%
MESH-4-2D	1325	1.2%	NaN	2750	1.4%	4.9%
MESH-5-2D	1330	0.8%	NaN	2790	0%	5.4%
MESH-6-2D	NaN	NaN	<b>Correct</b>	2820	1.1%	6.5%
MESH-7-2D	NaN	NaN	<b>Correct</b>	2820	1.1%	6.5%

Table 7.6: Comparing Numerical, Experimental and theoretical values for Rossiter mode. The coefficient  $\kappa$  is 0.66.

In the table, the value ”**Correct**” stands for the correct physics, since the meshes are not showing the first Rossiter mode.

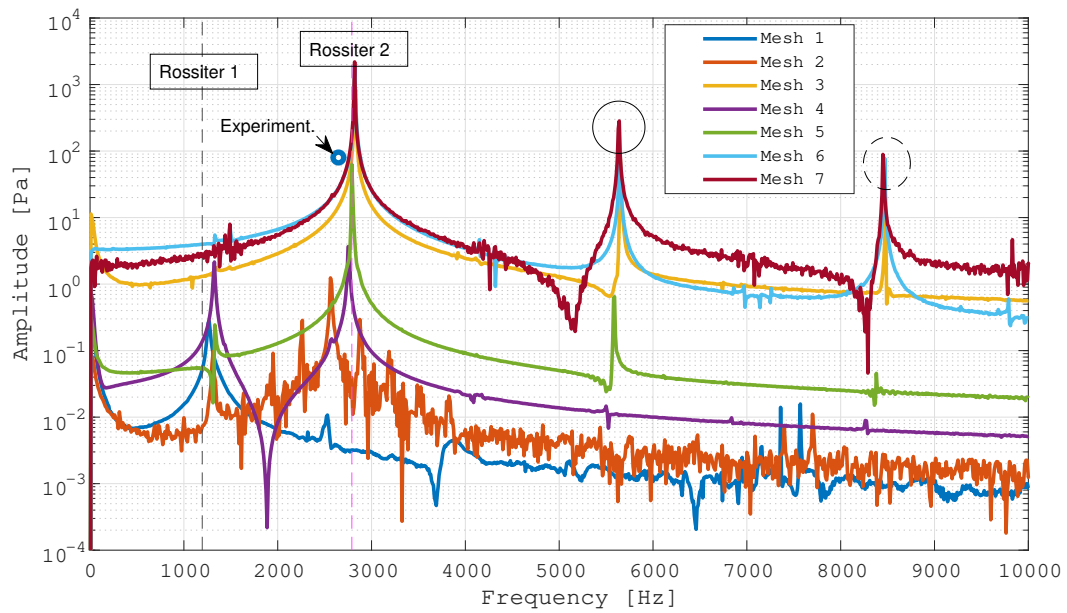


Figure 7.12: Comparison of mesh independence study with Rossiter theoretical modes frequency and experiments.

## 7.4 PARAMETERS AND SETUP

After having assessed all the meshes, the attention moves now to all the parameters that might play a relevant role in determining the Rossiter mode. The factors that are here are mainly two:

1. Influence of the time step  $\Delta t$ ;
2. Influence of the velocity profile that is used as input.

### 7.4.1 TIME STEP INFLUENCE

The time-step that is used for the unsteady simulations affects mainly two parts of the whole validation procedure:

1. The first aspect concerns the physics of the system;
2. Secondly, the FFT is influenced indirectly through the sampling frequency  $f_s$ .

Since an implicit solver is used, no problem concerning stability arises. If one was to use explicit schemes, then the CFL condition should be respected and the Courant number should ideally be kept below 1.

When it comes to the physics, if the time step is too high then the complex dynamics that are going on are not fully captured by the solver. Having a small time step allows to capture the full feedback loop of the phenomena, but having it too low would be impractical from a computational stand point. From the FFT point of view, one should keep in mind that the frequency resolution  $\Delta f$  in the frequency domain is defined as:

$$\Delta f = \frac{f_s}{N} \quad (7.6)$$

with  $f_s$  being the sampling frequency and  $N$  the number of samples. All our simulations are solved using a total length of simulation of  $120ms$ , of which the first 20 are removed to avoid the transient phase. At a sampling frequency of, say,  $100kHz$ , during  $100ms$  one has  $10k$  samples allowing therefore for a frequency resolution of  $10Hz$ , which is not too coarse but brings some accuracy-related limitations.

In the following section, different  $\Delta t$  are tried out at  $M = 0.7$  with MESH-6-2D to see what's the influence of the time step. The simulations were done keeping the same length of simulations. By recalling equation 7.7:

$$\Delta f = \frac{\Delta t^{-1}}{t_{tot} \Delta t^{-1}} = \frac{1}{t_{tot}} \quad (7.7)$$

Having the same total length of simulation means having the same frequency resolution in all the cases. For the scope of this section, eight different time steps are investigated. The results are shown in figure 7.13. Clearly, from the plot, some of the sampling frequencies ( $= 1/\Delta t^{-1}$ ) are not suitable for the frequencies. For example, the bigger time step  $\Delta t = 7.5e - 5s$  isn't picking anything. Note that the mesh is the same for all cases, but when simulating with coarser time step, the complex vortex roll-up (see later) is not properly captured. Thus, no feedback loop can occur due to the loss of information in the pressure field that happens from time step to time-step. Just for sake of clarity, with loss of information we are referring to the fact that by adopting a time step, say, of  $7.5e - 5s$  and by considering at  $M = 0.7$  a vortex velocity of  $150m/s$ , then after one time-step this vortex has already moved more than  $10mm$ , one fourth of cavity length. If we were to capture the cavity dynamics with only four "screenshots" per cycle (vortex generation, vortex roll-up and vortex impingement), then this will obviously affect the acoustic feedback. No lock-in occurs physically and no frequencies are captured.

As the time-step gets smaller and smaller, the frequencies starts to appear. Already for  $\Delta = 2.5e - 5s$ , a good description of the spectrum is obtained, being moreover coherent with with the experimental data. In fact, for  $M = 0.7$ , experimentally the only frequency that was captured was the first Rossiter Mode, making it the dominant one. The numerical solution is not different in that: the dominant frequency is the first Rossiter mode, whereas the second Rossiter mode is not even appearing (see plot). Differently from experiments though, a new frequency is picked in between and is indicated in the plot with a dotted circle, the latter appearing for  $\Delta t = 2.5e - 6s$ . Despite that, multi-harmonics of first Rossiter mode and the dotted-circle mode are occurring. The results are all displayed in table 7.7. Before moving ahead, it's important to stress out again the strong sensitivity of the amplitude on the test condition. The authors of



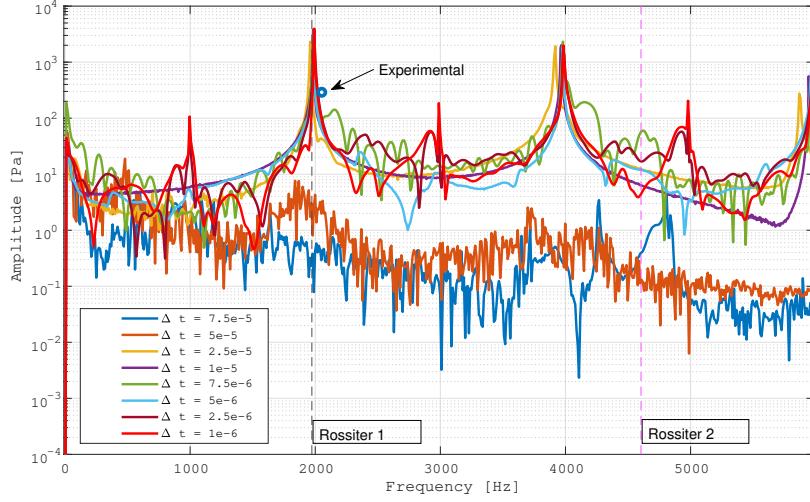


Figure 7.13: Comparing FFT for different sampling frequency, at  $M = 0.7$ . Monitor 2 is displayed.

	$f_{1,num}$ [Hz]	Rel. Error Rossiter 1 (= 1973Hz)	Rel. Error Experimental (= 2052Hz)	$f_{2,num}$ [Hz]	Rel. Error Rossiter 2 (= 4604Hz)	Rel. Error Experimental (=NaN)
$\Delta t = 7.5e - 5s$	NaN	NaN	NaN	NaN	NaN	NaN
$\Delta t = 5.0e - 5s$	NaN	NaN	NaN	NaN	NaN	NaN
$\Delta t = 2.5e - 5s$	1959	< 1%	4.5%	NaN	NaN	NaN
$\Delta t = 1.0e - 5s$	1983	< 1%	3.4%	NaN	NaN	NaN
$\Delta t = 7.5e - 6s$	1990	< 1%	3%	NaN	NaN	NaN
$\Delta t = 5.0e - 6s$	1990	< 1%	3%	NaN	NaN	NaN
$\Delta t = 2.5e - 6s$	1990	< 1%	3%	NaN	NaN	NaN
$\Delta t = 1.0e - 6s$	1992	< 1%	2.9%	NaN	NaN	NaN

Table 7.7: Comparing different  $\Delta t$ . Simulations were carried at  $M = 0.7$ , with MESH-6-2D. The coefficient  $\kappa$  is equal to 0.66.

[24] provided the all the details of the experiments, and the way the different operating point were tested. In one of the data collection provided, it was interesting to notice that when moving to higher Mach number, the frequency resulted to be lower and the amplitude much higher. In table 7.8 For instance,

0,68		0,7		0,72	
Freq. [Hz]	Ampl. [kPa]	Freq. [Hz]	Ampl. [kPa]	Freq. [Hz]	Ampl. [kPa]
2107	0,54	2052	0,29	2008	1,25
4239	0,27	4210	0,23	4230	0,29
		4254	0,26		

Table 7.8: Experimental data: frequency and amplitude for  $M = 0.68$ ,  $M = 0.70$  and  $M = 0.72$ .

when moving from  $M = 0.68$  to  $M = 0.70$ , theoretically the frequency should increase: according to Rossiter equation, it should go from 1940Hz to about 1970Hz. Practically, the opposite is occurring. The frequency is reduced. When moving instead from  $M = 0.70$  to  $M = 0.72$ , not only the frequency keeps halving, but the amplitude of the dominant mode for  $M = 0.72$  is now six times the amplitude of the dominant mode for  $M = 0.70$ . It should be clear that such Rossiter mode are extremely sensitive to the flow condition. A lot of research is still ongoing on this topic, and justifying this behaviour goes unluckily into the future work section.

### 7.4.2 INLET PROFILE INFLUENCE

All the simulations that have been carried so far have all been performed using the numerical velocity profile from the simple model, basically the profile that does not match the experimental one. It is now time to see if the approach that was investigated in the steady state chapter provides a suitable profile for the unsteady simulations. In fact, the conclusion of that chapter was that despite numerical data and experiments agreed well after introducing a boundary layer at the inlet, one should still remember that the model has been changed with the purpose of matching the numbers. This doesn't say though that the physics are the same. Note that in such 2D approach, the secondary flows and additional vortical structures that were present in the 2D cross section (see figure 6.22) are completely neglected: in fact, by extracting only a velocity profile along the height at mid-width position, the information are extracted along a curve and the two-dimensional secondary flows are lost.

For the scope of this section, three different profiles are analyzed:

1. The numerical profile from the simple model (called **NORMAL** case);
2. The numerical profile when a boundary layer is introduced at the inlet of the wind tunnel (called **MODIFIED** case);
3. The experimental profile that was measured (called **EXPERIMENTAL** case).

Ideally, one should expect the last two cases to coincide, since the numerical profile with the inlet boundary layer thickness led to  $\delta_{99} = 10.10mm$ , which is close to the experimental one. Moreover, since the two-dimensional secondary flows are neglected, one could think that the dynamics are going to be affected only by the boundary layer properties. In figure 7.14 the three profiles are compared with the theoretical Rossiter mode and the experimental value. The experimental value is highlighted with a dashed vertical line: its amplitude is instead marked with a square. Note that this comparison was done for  $M = 0.5$ . The results are summarized in table 7.9.

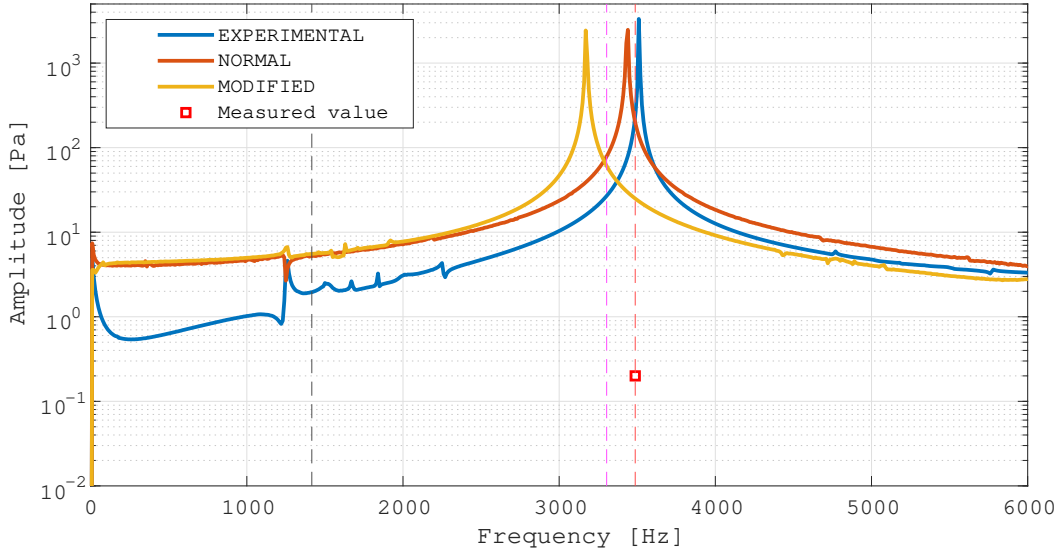


Figure 7.14: Comparing the FFT when different velocity profiles are used. The operating condition is  $M = 0.5$  and the time step that have been used is  $\Delta t = 1e - 05s$ .

Some comments can be done based on the results. Looking at table 7.9, differently from what we expected, despite matching the boundary layer thickness with the experimental one, the results from the FFT are far off. If comparing the results from the **EXPERIMENTAL** profile and the **MODIFIED** profile, there is a difference in the frequency of  $340Hz$  that is not negligible. The difference in frequency between the **NORMAL** case and the **EXPERIMENTAL** is  $170Hz$ , half the previous case. For this reason, from now on, all the simulation are performed using the simple model without introducing a boundary layer at the inlet.

	$f_{1,num}$ [Hz]	Rel. Error Rossiter 1 (= 1416Hz)	Rel. Error Experimental (=NaN)	$f_{2,num}$ [Hz]	Rel. Error Rossiter 2 (= 3304Hz)	Rel. Error Experimental (= 3487Hz)
NORMAL	NaN	NaN	NaN	3340	1.0%	4.2%
MODIFIED	NaN	NaN	NaN	3170	4.0%	9.1%
EXPERIMENTAL	1260	11%	NaN	3510	6.2%	<b>0.6%</b>

Table 7.9: Comparing different profiles at the inlet. Simulations were carried at  $M = 0.5$ , with MESH-6-2D and  $\Delta t = 1.0e - 5s$ . The coefficient  $\kappa$  is equal to 0.57.

If comparing the EXPERIMENTAL profile case then with the experimental measurements, one finds out that the relative error is very when looking at the frequency. Moreover, the EXPERIMENTAL profile seems to capture something that is close to the first Rossiter mode. From Hammer [24], no first Rossiter mode are measured through the kulite transducers. When looking deeply though at all the experimental data, something can be spotted around that frequency. In table 7.10, new data is reported from the experiments. As one can notice, for  $M = 0.497$  (almost 0.5), many frequencies appear: among them, one

$M = 0.549$		$M = 0.497$		$M = 0.451$	
Freq. [Hz]	Ampl. [kPa]	Freq. [Hz]	Ampl. [kPa]	Freq. [Hz]	Ampl. [kPa]
3583	0.016	245	$\sim 0$	226	$\sim 0$
		1388	$\sim 0$	1295	$\sim 0$
		3492	$\sim 0$	3132	$\sim 0$
		5015	$\sim 0$		

Table 7.10: Experimental data: frequency and amplitude for  $M = 0.549$ ,  $M = 0.497$  and  $M = 0.451$ .

looks like the first Rossiter mode. Despite the amplitude being extremely low ( $\sim 10^{-2}Pa$ ), they are still captured. When looking at the FFT of figure 7.14, in a very similar way the numerical simulation shows a weak peak at around 1260Hz. Although they look close, it is wrong stating that they refer to the first mode. Still, it's worthy noticing that the experimental profile lead to a peak that was not revealed by the numerical profiles.

After the mesh independence study, from which MESH-6-2D was picked as reference mesh, two more variables have now been fixed:

- The time step to be used, respectively  $\Delta t = 1.0e - 5s$ , since provides very good results with reduced computational cost;
- The profile to be used, respectively the NORMAL case where, instead of importing a boundary layer thickness at the wind tunnel inlet, the simplified boundary conditions are applied to extract the velocity profile (see table 6.4).

## 7.5 RESULTS AND DISCUSSION

After having established a framework that supports the 2D unsteady simulation, all the operating point must now be investigated. Most of them have already been presented, since many topics have been covered over the last pages, such as  $M = 0.4$  investigated for all meshes,  $M = 0.5$  investigated with different profiles and  $M = 0.7$  investigated for different time steps. In this section, all the results are shown all over again and compared more in detail with the experimental measurements. Some insights are given on the dynamics and concluding remarks close the chapter.

Starting from 7.20a up to figure 7.20f (at the end of this section), all the FFT referring to different operating points are displayed: the results are all collected in table 7.11.

		Numerical	Theoretical	Error [%]	Experimental	Error [%]
<b>M = 0.3</b>	Rossiter 1 [Hz]	<u>Not Picked</u>	946	NaN	Not Measured	Ok!
	Rossiter 2 [Hz]	2270	2209	2.7%	Not Measured	Not ok!
<b>M = 0.4</b>	Rossiter 1 [Hz]	<u>Not Picked</u>	1196	NaN	Not Measured	Ok!
	Rossiter 2 [Hz]	2820	2790	1.1%	2647	6.5%
<b>M = 0.5</b>	Rossiter 1 [Hz]	<u>Not Picked</u>	1416	NaN	Not Measured	Ok!
	Rossiter 2 [Hz]	3380	3304	2.2%	3487	3.1%
<b>M = 0.6</b>	Rossiter 1 [Hz]	1820	1610	12.4%	Not Measured	Not ok!
	Rossiter 2 [Hz]	<u>Not Picked</u>	3757	NaN	Not Measured	Ok!
<b>M = 0.7</b>	Rossiter 1 [Hz]	1980	1780	11.2%	2052	3.5%
	Rossiter 2 [Hz]	<u>Not Picked</u>	4155	NaN	4210	Not ok!
<b>M = 0.8</b>	Rossiter 1 [Hz]	1990	1929	3.2%	1912 - 1964	4.1% - 1.3%
	Rossiter 2 [Hz]	4420	4502	1.8%	4583	1.8%

Table 7.11: Results for different operating points, along with theoretical and experimental value (and relative errors). MESH-6-2D,  $\Delta t = 1.0e - 5s$ , NORMAL profile and SST turbulence model. The coefficient  $\kappa$  is equal to 0.57.

### Mach = 0.3

In case of  $M = 0.3$ , experimentally nothing is measured. All the kulite transducers did not picked up any frequency in all the tests. The results are quite different for the numerical case, where the second Rossiter mode is picked up. A second frequency is also measured, but it basically represents the second harmonic of the second Rossiter mode. When looking at the vorticity contour, such as the ones shown in figure 7.15, it is clear that the feedback loop is weak: the shear layer is bridging over the whole cavity, impinging the very last part of the leading edge. In figure 7.15c, a small portion of fluid is detached from the shear layer at the very end: its impingement on the leading edge should be theoretically responsible for the acoustic feedback that is generated, thus the second Rossiter mode. The shear layer does mild oscillations, going at maximum  $\approx 2mm$  above the cavity.

### Mach = 0.4

For what concerns  $M = 0.4$ , that was already investigated during the mesh independence study, the numerical results agree very good with the experiments. First of all, the first Rossiter mode is not picked neither numerically nor experimentally. Actually, if one checks figure 7.20b, a very small and noisy behaviour can be noticed around the first mode, but is still too low to be regarded as a mode. The second Rossiter mode, now, is picked both from the experiments and the numerical simulations. Moreover, they agree very well also in terms of frequency, with only a 1.1% error. More frequencies are picked but the remaining ones are only second and third harmonics of the second mode. From the shear-layer point of view, they behave similarly to Mach 0.3: small amplitude oscillations of the shear layer past the cavity mouth. If we were to compare some of this results with previous ones in the literature, a good agreement can be found with Gloerfelt [25] saying that shear layer mode occur for low  $L/\delta_2$  ratio: more specifically, a shear layer mode (Rossiter Mode) occurs for  $L\delta_2 \approx 60$  and a *wake mode* occurs for

very high values of  $L\delta_2$ , such as  $\sim 6000$ . In this case, the ratio  $L/\delta_2$  is more or less 30 which suggest shear layer mode.

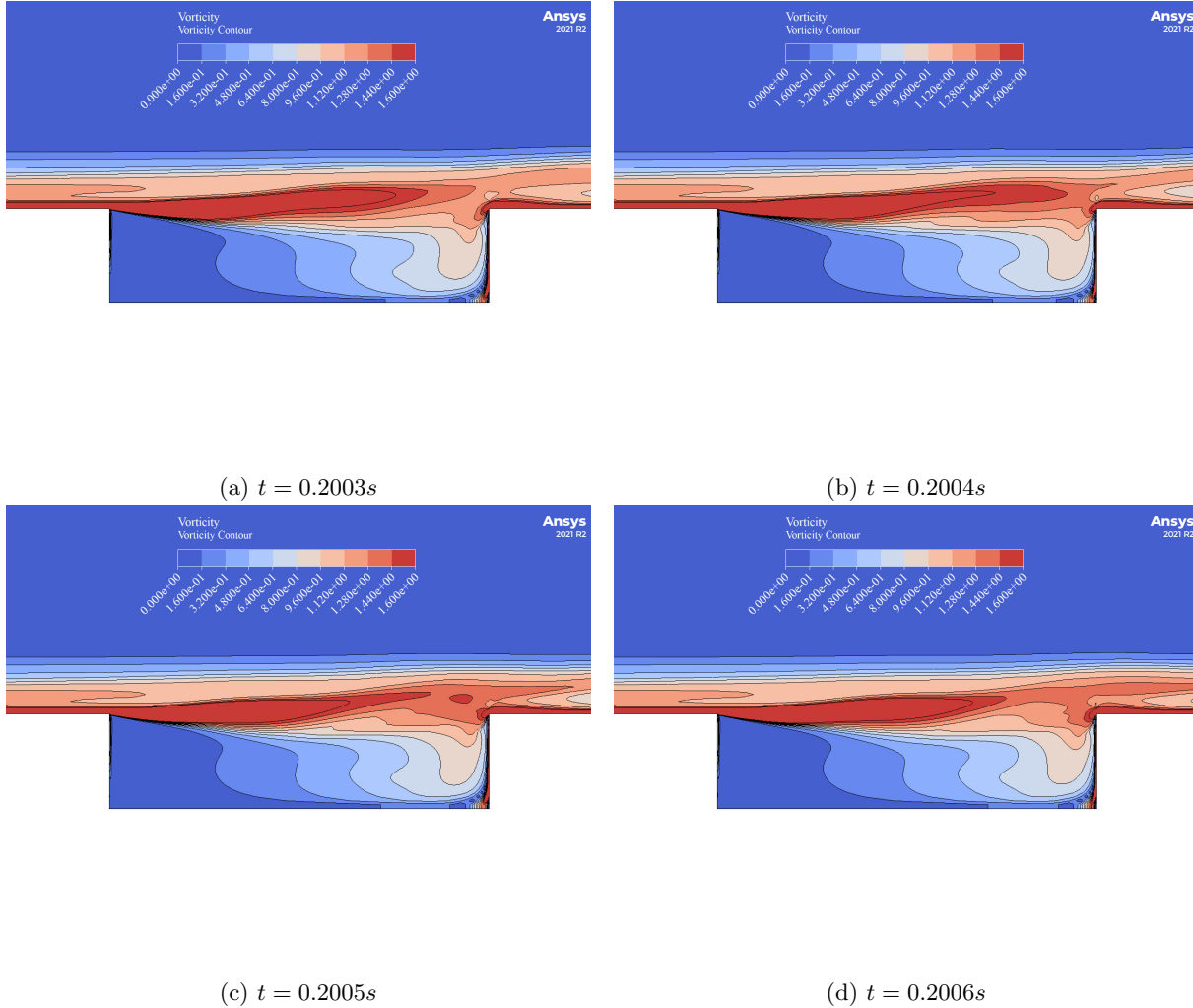


Figure 7.15: Vorticity Contour for  $M = 0.3$  for four different time-steps. The dimensionless vorticity is defined as  $\omega D/U_\infty$ .

### Mach 0.5

Also this case has already been visualized during the profile dependence study. A very good agreement is found in relation to the experimental results. The first Rossiter mode it not captured neither experimentally nor numerically, leading to a good start. The second Rossiter mode, which happens to be the dominant one in the experimental results, is captured in the numerical simulation and is the dominant as well. The dynamics in this case are the same, in the sense that still a shear layer mode is captured, although the intensity of the vortices are much higher. For instance, if one was to plot the dimensionless vorticity contour, the vortex shedding would now be much more clear: see figure 7.16. From the contour plots, it is clear the vortex formation, vortex roll-up and vortex impingement. Technically, something similar should occur also for  $M = 0.3$ , although from 7.15 it's not that clear.

### Mach = 0.6

In this case, a not-so-good agreement is reached with the experiments. In fact, from an experimental point of view, both first and second Rossiter mode are not picked up. Numerically, instead, something

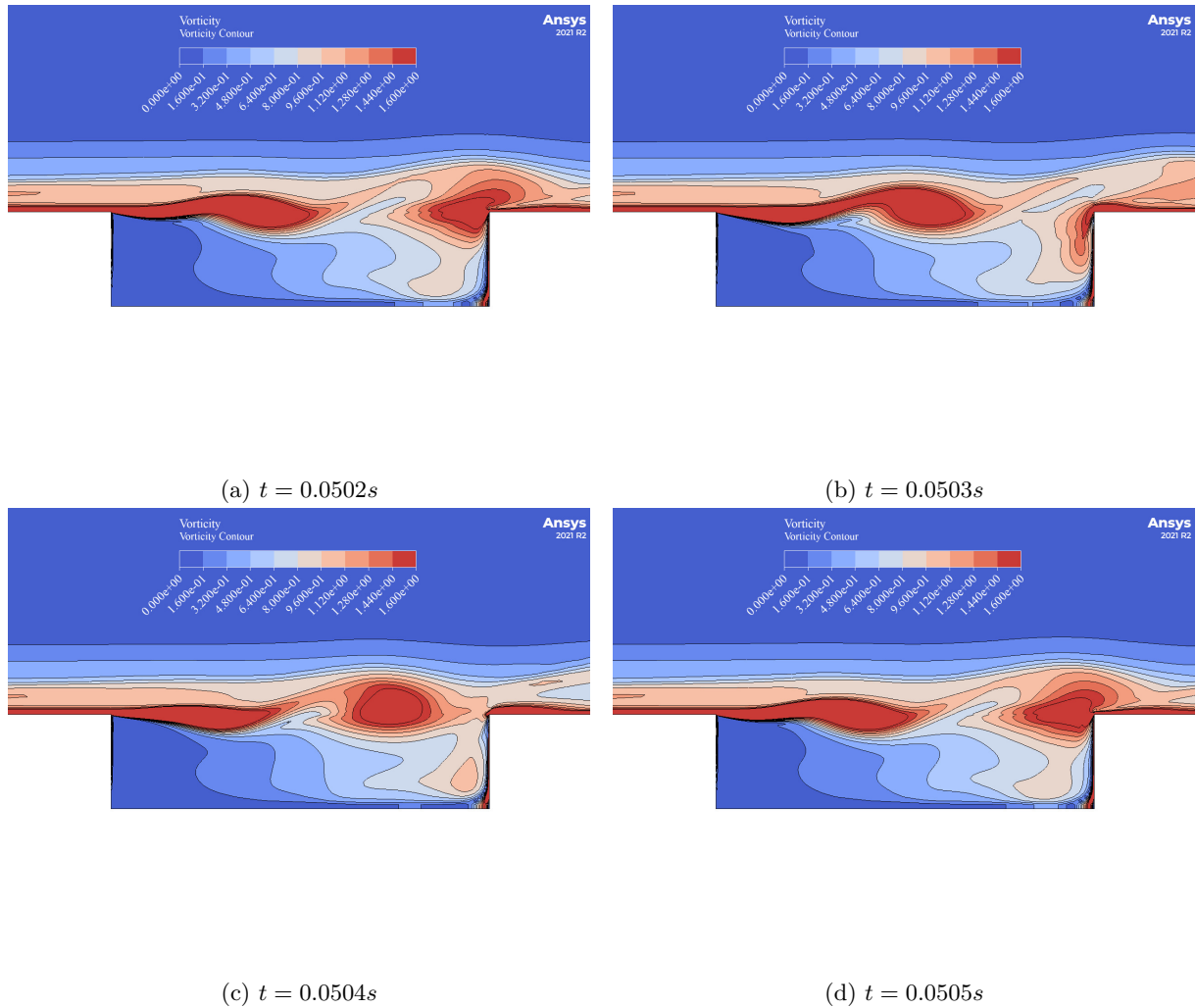


Figure 7.16: Vorticity Contour for  $M = 0.5$  for four different time-steps. The dimensionless vorticity is defined as  $\omega D/U_\infty$ .

that seems similar to the first Rossiter mode is picked up. This does not mean necessarily that it's the first Rossiter mode since 10% relative error is found. The simulated frequency that seems to resemble the second Rossiter mode in figure 7.20d is instead the second harmonics of the first mode. Experimentally, a much higher frequency is captured, of around  $5729Hz$ : the possible explanation for this frequency could either be the third harmonics of the first Rossiter mode or eventually even the third Rossiter mode. The values are showed in table 7.12. The same frequencies have been computed using  $\kappa = 0.52$  and  $\kappa = 0.66$  (see Mach=0.7 section to understand).

### Mach = 0.7

For  $M = 0.7$ , the overall physics are well captured by the numerical simulation. Both numerics and experiments are locked it at the first Rossiter mode (this operating point is the only one that experimentally locks in at the frequency of the first Rossiter mode), which is a good result, suggesting that the dynamics are changing. The results though are quite different from the expected value, with a relative error of more than 10% but finds good agreement with the experimental value (3.5% error). All the other frequencies that can be seen from figure 7.20e are all multi-harmonics of the first Rossiter mode. One of the possible reasons for the disagreement with the experimental results could be associated with the value of  $\kappa$  in the Rossiter formula (equation 3.5). This value expresses the ratio between the propagation

	Mode	Frequency [Hz]	Mode ( $\kappa = 0.52$ )	Mode ( $\kappa = 0.66$ )
<b>M=0.6</b>	Rossiter 3	5905	5510	6572
	Rossiter 1 #3	5460	4508	5377
	Experimental		<b>5729</b>	

Table 7.12: Comparison for  $M = 0.6$  with higher order frequencies: Rossiter 1 # 3 indicates the third harmonics of the first Rossiter mode.

speed of the vortices  $u_v$  and the free stream velocity  $U_\infty$ , and in this work, coherently with the work from Hammer [24], it is always assumed to be 0.57. Experimentally, this ratio has been seen to vary within a range  $0.57 \div 0.66$ . Experimentally computing this value is not an easy task, but from a numerical point of view it can be done quite easily. First thing to consider is that the vortices are associated with low pressure: figure 7.17 shows a snapshot of the dimensionless vorticity contour and the pressure amplitude contour. As one can see, the position of the vortex coincides with the low-pressure region.

By tracking that vortex using monitor points, and by assuming that the lowest pressure is associated with the core of the vortex, then one can detect the time that it takes to the vortex to jump from monitor to monitor. In figure 7.18a one can see the pressure valleys from three monitors (respectively at  $x = 27mm$ ,  $x = 32mm$  and  $x = 38mm$  starting from the trailing edge). When computing the vortex velocity with  $M = 0.7$  and considering this approach, it turns out that the ratio  $\kappa$  is smaller than 0.52, smaller than the actual used value of 0.57. When computing the new Rossiter mode, it turns out that the theoretical frequencies are even further from the experimental and numerical one. In table 7.13 the frequencies are showed. In case instead one was to consider the high pressure region (the small red contour on the left of figure 7.17a) and monitor its travelling speed, then a much higher speed is obtained ( $166m/s$  if compared to the  $100m/s$  of the vortex speed), thus leading to a  $\kappa = 0.66$  that finds better agreement with experiments and simulations (see figure 7.18b). Although this new value seems promising, it is not fully understood what's the meaning behind that region: from figure 7.17b, this high pressure region seems to fall exactly before the vortex roll-up, in a region of transition between the shear detached boundary layer and the vortex.

	$\kappa$	Rossiter 1 [Hz]	$\varepsilon_{num}$	$\varepsilon_{exp}$	Rossiter 2 [Hz]	$\varepsilon_{num}$	$\varepsilon_{exp}$
<b>M = 0.7</b>	0.57	1781	10%	13%	4155		
	0.52	1666	16%	19%	3888	<b>NOT MEASURED</b>	
	0.66	1973	<1%	4%	4604		

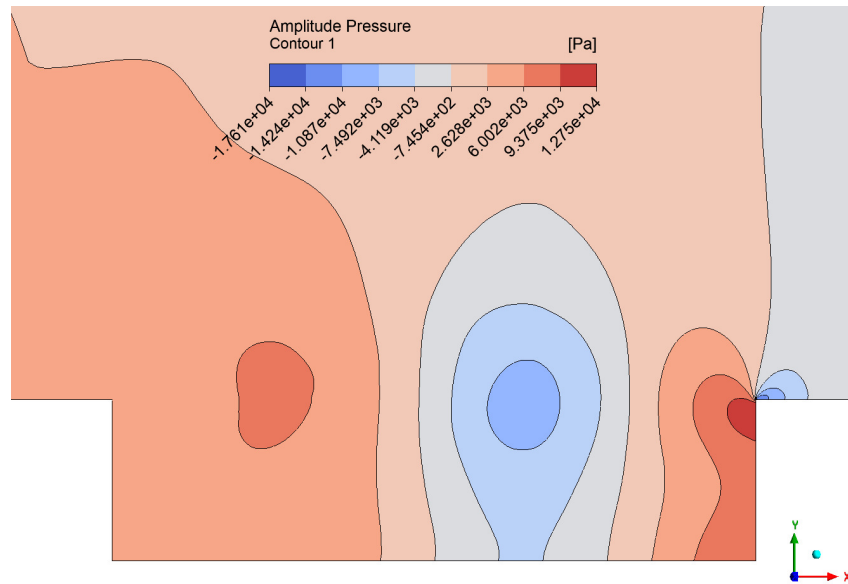
Table 7.13: Comparing numerical and experimental results with the predicted value by Rossiter formula for different  $\kappa$ .  $\varepsilon_{num}$  stands for the relative error with respect to the numerical predicted frequency;  $\varepsilon_{exp}$  stands for the relative error with respect to the measured experimental frequency.

### Mach = 0.8

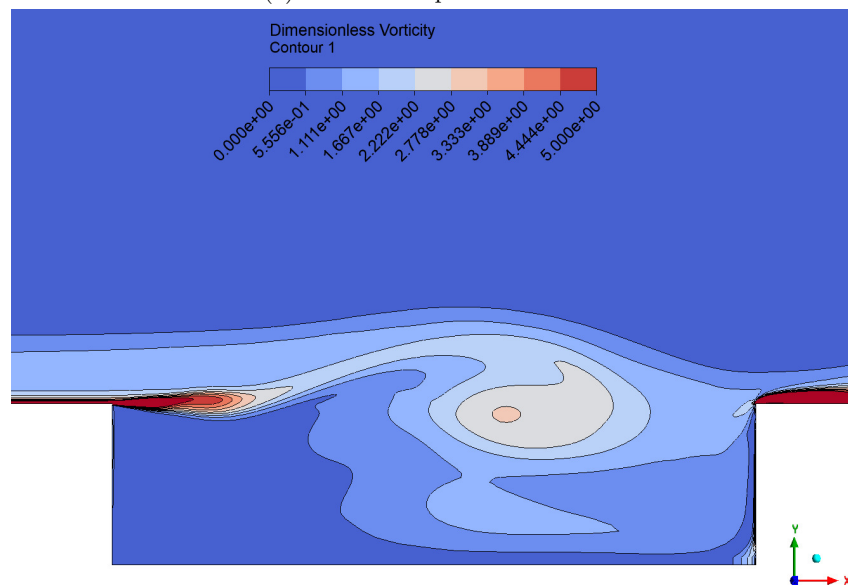
Although the initial transient regime has been removed, the FFT remains noisy. In this case, a good agreement between numerical and experimental data is found, to a certain degree. In fact, when it comes to the first two Rossiter modes, they are both predicted quite accurately. However, experimentally and numerically, within the range of frequencies that goes from first Rossiter mode and second Rossiter mode, other frequencies are picked up. In table 7.14 all the numerical and experimental frequencies are reported.

	Type	All the frequencies [Hz]				
<b>M=0.8</b>	Experimental	1912	1964			4583
	Numerical		1990	2440	3980	4420

Table 7.14: All the measured frequencies (experimentally and numerically) for  $M = 0.8$ .



(a) Pressure amplitude contour.



(b) Dimensionless vorticity contour.

Figure 7.17: Pressure amplitude contours 7.17a and dimensionless vorticity contours 7.17b for  $M = 0.7$ , at same time step.



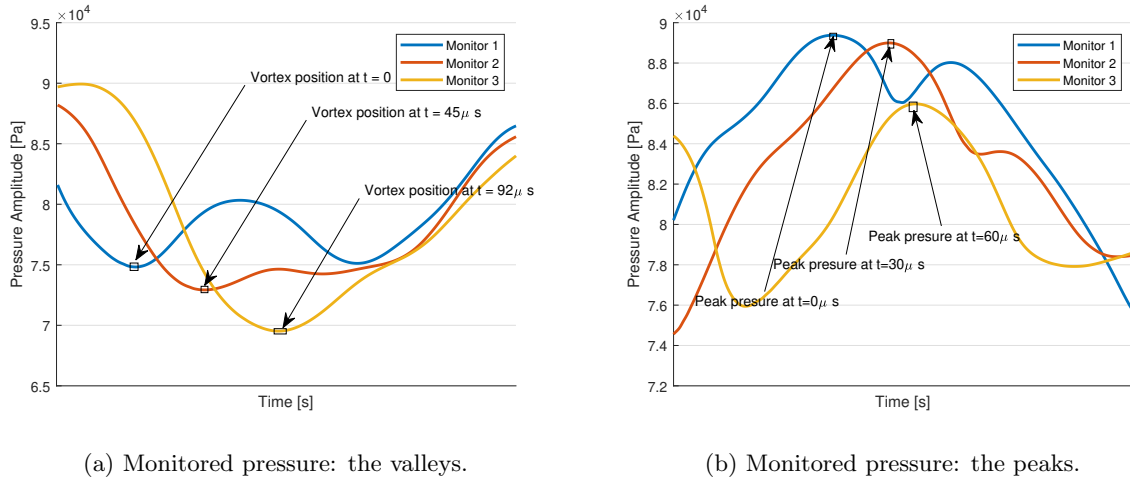


Figure 7.18: Pressure history measured by monitors: since the monitor position is known, by taking the peaks/valleys it's possible to extract the vortex velocity.

In table 7.14, the experimental row refers to all the experimentally measured frequency, whereas numerical refers to all the numerically simulated frequencies. The values have been associated in columns based on their closest value: for instance, the experimental value 1964 was associated with 1990 since is the closest one, but this does not mean that they refer to the same mode of oscillation. In fact, the value 1912 Hz could refer to the first Rossiter mode as well as the numerical value 1990 Hz, whereas the experimental 1964 Hz could refer to anything else. Excluding the second Rossiter mode that finds good agreement with the experimental value (40 Hz of difference), two new frequencies are picked during the simulations that did not showed up in the experiments. These are respectively:

- $f = 2440$  [Hz];
- The second harmonics of the first Rossiter mode  $f = 3980$  [Hz].

The reason for the 2440 frequency is not known. Following the same procedure as did by Hammer *et al* [24], the half-wavelength and quarter-wavelength resonator are introduced to show if this frequencies coincide with the picked one (the formulas are given in equation 2.4 and 2.5); moreover, the depth-resonance also presented by Block [7] was used. The results are shown in figure 7.19: clearly, none of them is suitable to describe the 2440 Hz frequency.

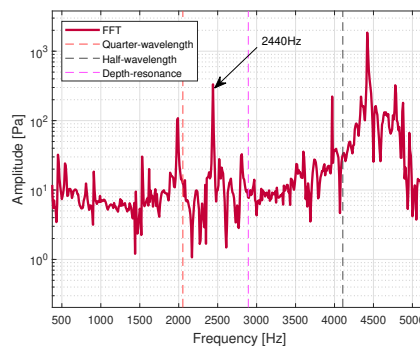
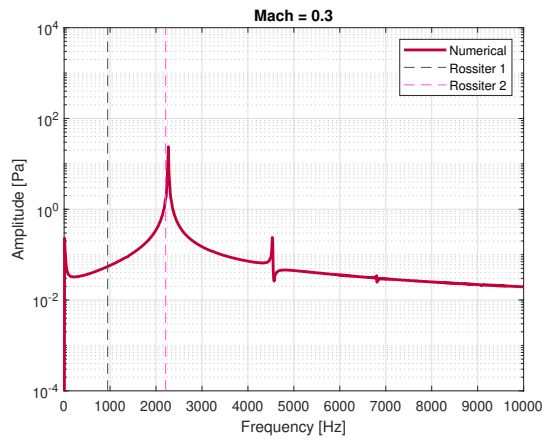
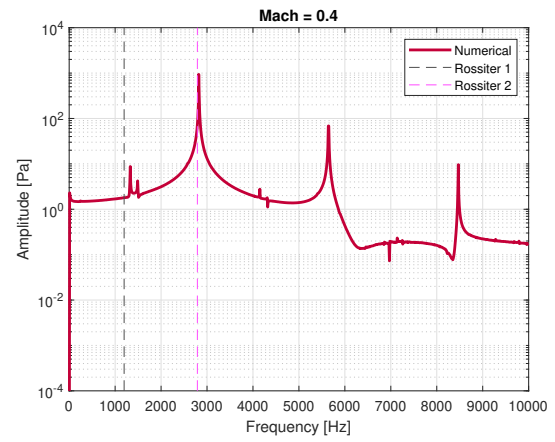


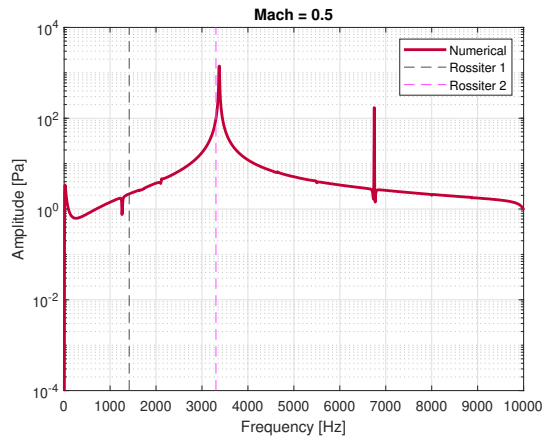
Figure 7.19: FFT for  $M = 0.8$ : comparing the 2440 Hz frequency with other models.



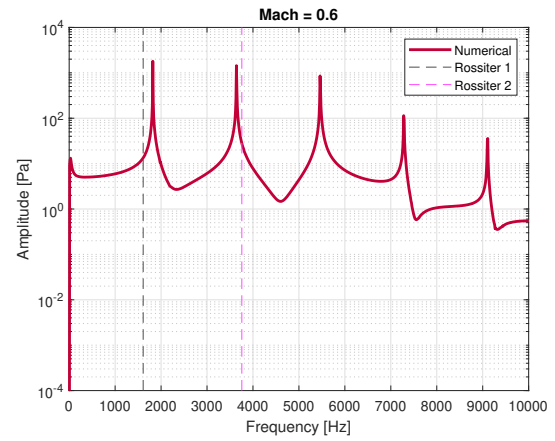
(a) FFT for  $M = 0.3$ : MESH-6-2D, NORMAL profile and  $\Delta t = 1.0e - 5s$ .



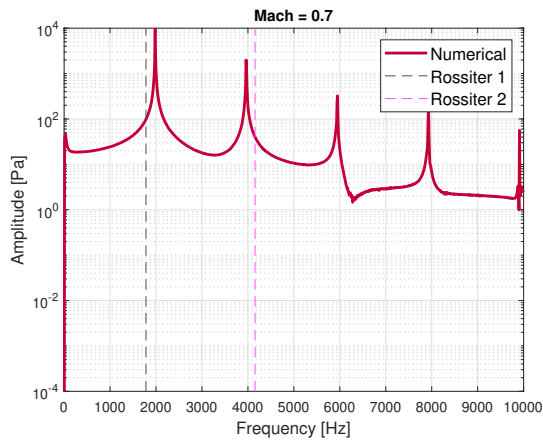
(b) FFT for  $M = 0.4$ : MESH-6-2D, NORMAL profile and  $\Delta t = 1.0e - 5s$ .



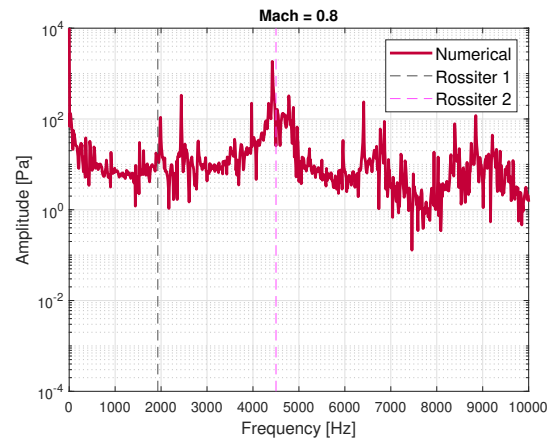
(c) FFT for  $M = 0.5$ : MESH-6-2D, NORMAL profile and  $\Delta t = 1.0e - 5s$ .



(d) FFT for  $M = 0.6$ : MESH-6-2D, NORMAL profile and  $\Delta t = 1.0e - 5s$ .



(e) FFT for  $M = 0.7$ : MESH-6-2D, NORMAL profile and  $\Delta t = 1.0e - 5s$ .



(f) FFT for  $M = 0.8$ : MESH-6-2D, NORMAL profile and  $\Delta t = 1.0e - 5s$ .

Figure 7.20: FFTs for all operating points

## 7.6 CONCLUDING REMARKS

The unsteady 2D analysis has showed some good results and other time it didn't proved to be as effective. Considering that four out of six operating points were correctly predict from a physics point of view (the right Rossiter mode were measured) and that for the other two some mistakes were done, this works proved to be quite reliable and accurate nearly 70% of the times. Considering the simplified approach both in terms of turbulence model and two-dimensional simplification, the results lies the basis and defines the work-frame under which future simulations needs to be performed. Again, it's important to stress out that predicting amplitude represents still a strong limitations for various reasons, mainly:

- Strong sensitivity of the numerical results on the turbulence model (see [11]);
- Strong sensitivity of the experimental results on the setup and influence from previous operating point during the transition.

To have good numerical results in terms of amplitude, the experiments should first provide reliable data regarding the amplitudes.

Moreover, having a good understanding of the empirical coefficient  $\kappa$  and  $\gamma$  (the latter not being investigated) may result in better comparison of the Rossiter mode and the experimental data.

We conclude this chapter showing a final plot in which the theoretical Rossiter mode are compared with the experimental and numerical values in a  $St - M$  plot (Strouhal-Mach): figure 7.21.

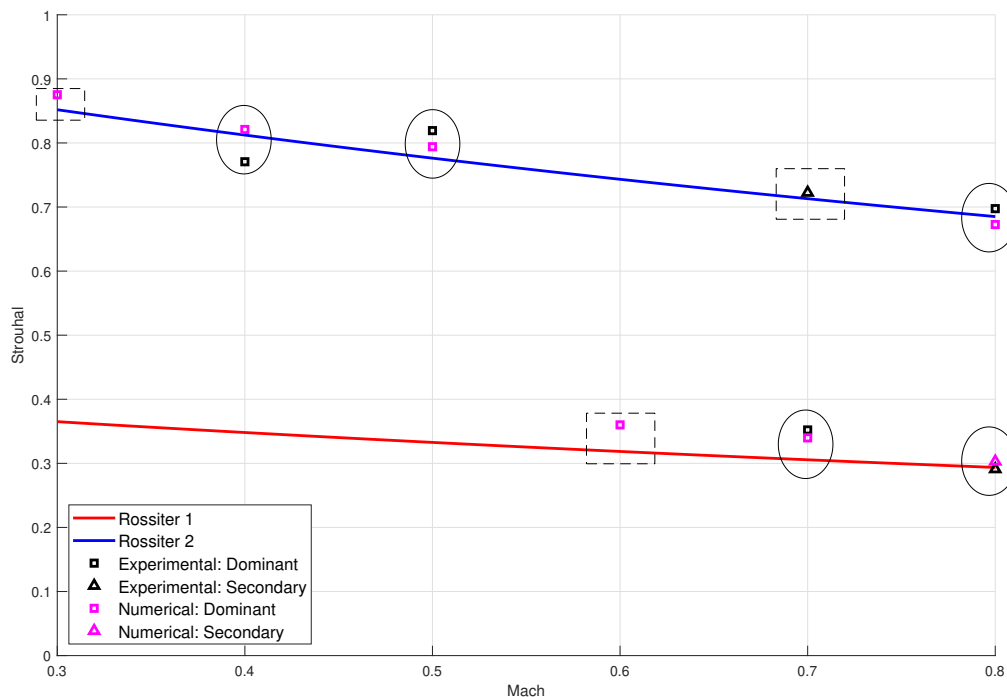


Figure 7.21: Comparison of experimental Strouhal number and numerical one: in black the experimental points and in magenta the numerical ones (square stands for dominant and triangle stays for secondary).

From the figure, the black circles highlight the similarity between numerical and experimental Strouhal number, whereas the dashed square points out the difference. Those are the differences that must be investigated in the future.

## Chapter 8

# CONCLUSION

The main objective of this work was the numerical validation of experimental data from a KTH wind tunnel facility ([24]) concerning the so-called Rossiter mode. The objective of numerical prediction is to substitute experimental measurements in initial development stages for swift determination and fast benchmarking of the cavity model. To optimize computational resources and time, two-different geometries were used, one for the wind tunnel only and one for the cavity section only, the latter being further simplified into a 2D model. Moreover, still related to limited time and resource, RANS and URANS models were used.

The wind tunnel analysis showed a non-ideal agreement with the experiments when a simple model with simple boundary conditions was used, despite the different turbulence model that were used after an extensive literature review. Changing the model, by extending the inlet or outlet, or even by enhancing the turbulence intensity at the inlet, proved to be not as effective as imposing a total pressure profile at the inlet of the wind tunnel. This, lastly, provided good results that found good agreement with the experiments. Although this seemed to work, the 2D unsteady analysis showed that still a lot of work must be done to properly define the wind tunnel model. This steady analysis, performed on the wind-tunnel, provided an insight to possible reason and future work that would eventually lead to the definition of a more appropriate system.

The unsteady analysis, main focus of this work, was performed using a 2D cavity model for the following two reasons:

- Lie the basis for unsteady analysis;
- Able to provide fast results.

The main obstacle when it comes to the unsteady analysis of the cavity was the length of the simulations: going straight to a 3D unsteady analysis, which was also attempted, proved to require at least ten days worth of computations. Since this work represents the early stage of future development for CFD simulations of the cavity, finding out iteratively the best setup was simply too time consuming and not feasible. A 2D approach solved this problem, allowing an analysis of the setup (in terms of boundary conditions, models, time steps) on much faster results. One of great results. This helped, for example, to test the numerical profile that used to match the experimental one. The latter, although promising in the steady simulation, provided frequencies with a much greater error than the simple numerical profile derived from the simple model. The extensive mesh independence study revealed that the stream-wise stepping  $\Delta x$  suggested by the company partner was effective in capturing Rossiter mode: interestingly, using coarser meshes and wall functions provided valid results. The overall result of the unsteady analysis proved to be effective, quantitatively, 70% of the time, providing promising results in terms of frequency. The numerical evaluation of the  $\kappa$  constant was not really effective: two values of  $\kappa$  based on two vortex-like region of the flow provided very different results, with one of them being very close to the experimental one. The main limitation of this work, as stated, was the determination of the amplitude of such frequencies due to its high sensitivity both from a numerical and experimental point of view. Figure 7.21 finally shows the general overview of the unsteady simulation in a clear way.

## Chapter 9

# FUTURE WORK

The fairly simplified model that were used for the scope of this work offer a lot of room for improvement, ranging from the very initial steady analysis to the very last step of the unsteady one

First of all, the steady analysis revealed that the only way to match experimental and numerical profiles were by manually imposing an artificially created total pressure profile: the idea was to impose a boundary layer thickness at the very inlet of the wind tunnel. The profile that was used was based on some assumptions, since a Blasius-like profile was imposed based on the total pressure instead of the velocity. In the future, two different approaches may be analyzed:

1. First, different and more accurate velocity profile should be imposed at the very inlet trying to have a more uniform boundary layer at the measurement section (which was not the case of this work since some vortical structures appeared to increase  $\delta_{99}$ , see figure 6.22);
2. Second, the settling chamber should be included in the domain and discretized as well, so that the full facility is considered and no room for errors/assumptions is given.

Different turbulence models have been tested in this work. Nonetheless, the last approach (imposed artificial profile) was carried using only a SST turbulence model. Trying to see the different combinations of inlet boundary layer - profile type - turbulence model will shed more light and will eventually support the unsteady analysis. The following suggestions should afterwards all be confirmed with an unsteady simulation. In fact, implementing alternative solution in the steady wind tunnel does not mean reproducing with high fidelity the dynamics that are occurring in the cavity. This was the case, for example, when the numerical profile that corresponded to the experimental one was incorporated in the unsteady analysis, resulting in a frequency that exhibited a higher error compared to the experimental value.

For what concerns the unsteady simulations, a lot of work must be done, starting from the very approach. First, 3D model should be considered with the same turbulence models and boundary conditions to see how they compare with the 2D cavity. From this point of view, the mesh convergence study performed in this work might be helpful: one of the insight that was given, in fact, was that coarser stream-wise step could have been employed ( $\lambda/15$  instead of  $\lambda/30$ ), or even wall functions. When moving to the 3D analysis, analyzing the impact of the secondary flows and vortical structures that are developed due to the squared wind tunnel can shed some light also in the choice of the turbulence model for the wind tunnel. If, for instance, one notice that the asymmetric vortical structures that forms close to the walls of the wind tunnel with the  $k - \varepsilon$  (see figure 6.13) improves the results in the cavity section, then it's worthy having a discussion on the effect of the secondary flows.

Another aspect to be investigated in the unsteady simulations is the effect of the turbulence model. In this work, only SST was investigated, although the SBES was attempted. Definitely, a future task should aim at implementing hybrid methods URANS/LES, or eventually try a full LES. References have been given in the unsteady analysis that explain the mesh requirements of these models. Nonetheless, the literature is full of examples that show differences and similarities between URANS and LES: they can represent a starting point to argue the need of LES.

Finally, the procedure that was proposed in this work should find validation or improvements with different cavity's aspect ratio, or different geometry. This would allow to ultimately define a final frame-work

under which all simulations would converge ideally to the experimental results, regardless of geometry and cavity type.

# Chapter 10

## APPENDIX A - SIGNAL ANALYSIS

### 10.1 INTRODUCTION

The reason for this appendix is to introduce the reader to some basic concepts of signal analysis, since the post-processing of the numerical results heavily relies on these topics. More precisely, the pressure signals that is being extracted at the monitored point is analyzed in the *frequency domain* through a discrete Fourier Analysis. The main reference is [53].

### 10.2 FOURIER ANALYSIS

An harmonic function can be re-written as linear combination of basic harmonic functions, such as sine and cosine, of fundamental frequency  $\Omega_0$ . Given the generic harmonic function  $f(t)$  of period  $T_0$  and fundamental frequency  $\Omega_0 = 2\pi/T_0$ , the Fourier series of  $f(t)$  can be written as:

$$f(t) = a_0 + \sum_{k=1}^{\infty} (a_k \cos(k\Omega_0 t) + b_k \sin(k\Omega_0 t)) \quad (10.1)$$

where:

$$a_0 = \frac{1}{T_0} \int_0^{T_0} f(t) dt \quad (10.2)$$

$$a_k = \frac{2}{T_0} \int_0^{T_0} f(t) \cos(k\Omega_0 t) dt \quad (10.3)$$

$$b_k = \frac{2}{T_0} \int_0^{T_0} f(t) \sin(k\Omega_0 t) dt \quad (10.4)$$

Equation 10.1 says that the periodic function  $f(t)$  can be written as a combination of infinite harmonics functions with frequencies being multiple of the fundamental frequency  $\Omega_0$ ; equations 10.3 and 10.4 indicates the relative weight of the  $k$ -th harmonics of the fundamental one ( $\Omega$ ).

Contextualizing this into the cavity acoustic case, the relative weights will be higher when these multi-harmonics coincide with the Rossiter modes, since the pressure in the monitored point is changing coherently with these frequencies, therefore other frequencies are should have a small contribution in the overall signal (a part from noise or numerical errors).

Although expression 10.1 is easier to understand, from a numerical point of view the exponential form is preferred. This is based on Euler identity:

$$\cos(k\Omega_0 t) = \frac{1}{2} (e^{ik\Omega_0 t} + e^{-ik\Omega_0 t}) \quad (10.5)$$

$$\sin(k\Omega_0 t) = \frac{1}{2i} (e^{ik\Omega_0 t} - e^{-ik\Omega_0 t}) \quad (10.6)$$

By substituting the two expressions in the first formulation of the Fourier series (eqn. 10.1), one has equation 10.7:

$$f(t) = a_0 + \sum_{k=1}^{\infty} \frac{a_k - ib_k}{2} e^{ik\Omega_0 t} + \sum_{k=1}^{\infty} \frac{a_k + ib_k}{2} e^{-ik\Omega_0 t} \quad (10.7)$$

Generally, a new term is introduced, namely  $F_k$ :

$$F_k = \frac{a_k - ib_k}{2} \quad (10.8)$$

Which ultimately leads to this definition of the Fourier Series, which is:

$$f(t) = \sum_{k=-\infty}^{+\infty} F_k e^{ik\Omega_0 t} \quad (10.9)$$

Everything said so far applies if  $f(t)$  is a periodic function with fundamental frequency  $\Omega_0$ . The signal that are measured in the monitors are far more complex than that. Figure 10.1 shows a simple example of that: In that case one wants to extend the Fourier series also to non-periodic functions, which can be

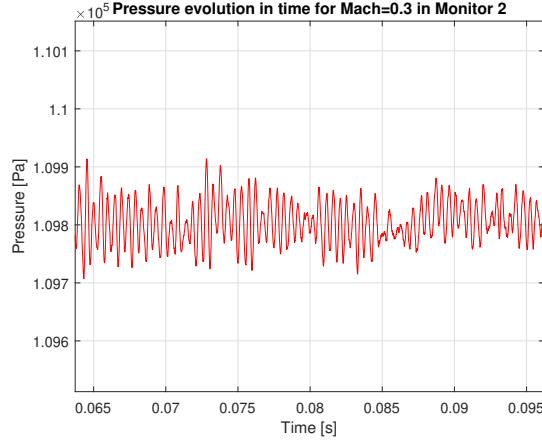


Figure 10.1: Pressure signal measured at the second monitor point.

interpreted functions of period  $T_0 \rightarrow \infty$ . Expression 10.9 can be written as:

$$f(t) = \frac{1}{T_0} \sum_{k=-\infty}^{+\infty} (F_k T_0) e^{ik\Omega_0 t} \quad (10.10)$$

By defining  $k\Omega_0$  as  $\Omega_k$ , indicating the  $k$ -th harmonic, and  $\Omega_0$  being the *frequency resolution*, defined as:

$$\Omega_0 = \Delta\Omega = \Omega_{k+1} - \Omega_k \quad (10.11)$$

Then one has:

$$f(t) = \frac{1}{2\pi} \sum_{k=-\infty}^{+\infty} (F_k T_0) e^{i\Omega_k t} \Delta\Omega \quad (10.12)$$

As mentioned,  $T_0$  is approaching  $\infty$ : if so, considering that  $\Omega_0 \propto T_0^{-1}$ , then  $\Delta\Omega \rightarrow d\Omega$ . Finally, by calling also  $F_k T_0$  as  $F(\Omega)$ , one has this continuous representation of the Fourier series, also called **inverse Fourier transform**, since allows to move from the frequency domain to the time domain:

$$f(t) = \frac{1}{2\pi} \int_{-\infty}^{\infty} F(\Omega) e^{i\Omega t} d\Omega \quad (10.13)$$



By doing some manipulation to the previous formulas, the **direct Fourier transform** is achieved which allows to move from the time domain to the frequency domain:

$$F(\Omega) = \int_{-\infty}^{+\infty} f(t)e^{-i\Omega t} dt \quad (10.14)$$

We highlight the essence of the Fourier Transform, which mainly aims at extrapolating the frequencies and the relative harmonics from a signal, as well as their amplitudes. Something that is also worthy mentioning is the **Parseval theorem**: the energy associated to a signal is the same if either computed in the time domain or frequency domain. From a mathematical point of view, this can be written as:

$$\int_{-\infty}^{\infty} (f(t))^2 dt = \int_{-\infty}^{\infty} |F(\Omega)|^2 d\Omega \quad (10.15)$$

An important practical consequence of the Parseval theorem from a CFD point of view is that if one is interested in highlighting the Rossiter mode, then a long enough simulation is required to capture such frequencies. Of course, according to the mathematical formulation, achieving a simulation that goes from  $t \rightarrow -\infty$  to  $t \rightarrow +\infty$  is not practical. In figure 10.2 the pressure signal is plotted for the first 5'000 time-steps, with its relative Fourier Transform (a simple FT); on figure 10.3 instead the pressure signal is taken for 50'000 time-steps, and the Fourier Transform are compared on the right. From figure

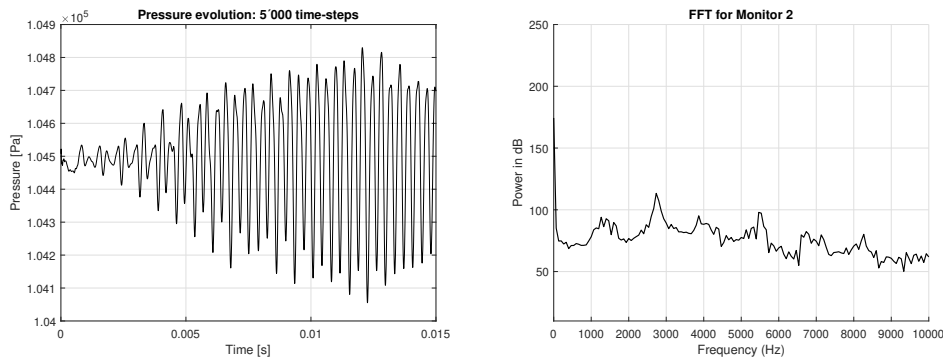


Figure 10.2: On the left, pressure signal for Mach= 0.4 at monitor 2 position for the first 5'000 time-steps; on the right, the Fourier transform for the displayed signal.

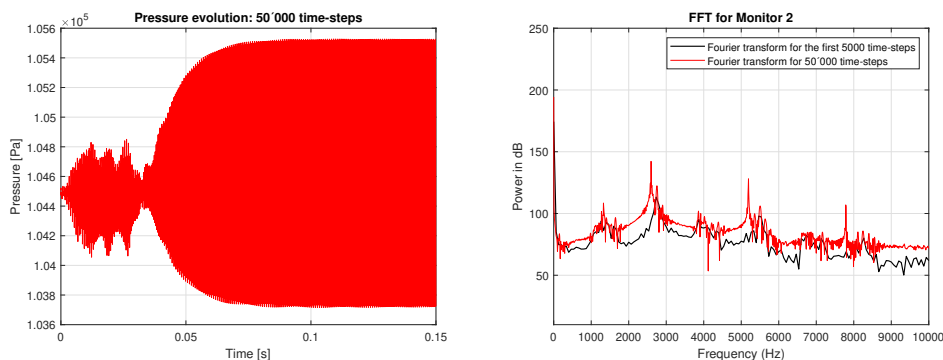


Figure 10.3: On the left, pressure signal for Mach= 0.4 at monitor 2 position for 50'000 time-steps; on the right, the Fourier transform for the displayed signal (compared with the previous Fourier transform).

10.3 it's clear that the longer the simulation the more accurate will be the frequency estimated in the frequency domain. This is not something that is always achievable due to computational resources and time-availability. So far, the Fourier transform was introduced for **continuous** functions. In reality, one

has a discrete signal: pressure is measured at a certain **sampling frequency** over time. Ideally, if this sampling frequency was  $\infty$  then one could have a continuous representation of pressure over time. Since the sampling frequency are finite, one should resort to a discrete formulation of the Fourier Transform based on the samples that one has.

The *Discrete Fourier Transform* (DFT) rises from two main issues:

1. There is no such thing as continuous signals;
2. It's not possible to carry measurements from  $t \rightarrow -\infty$  to  $t \rightarrow +\infty$ .

In reality, one has a finite number of samples to deal with. Instead of having  $f(t)$  one has  $f_n(t) = f(n\Delta t)$  with  $\Delta t$  being the *sampling period*.

Given  $N$  samples, the DFT is defined as:

$$F_k = \frac{1}{N} \sum_{n=0}^{N-1} f_n e^{-i2\pi k \frac{n}{N}} \quad (10.16)$$

where  $F_k$  denotes the weight of the  $k$ -th harmonics with respect to the given frequency resolution  $\Omega_0 = \Delta\Omega$ . The frequency resolution (the distance between  $F_{k+1}$  and  $F_k$  then its only function of the sampling frequency  $f_s$  and number of samples  $N$ , according to relation 10.17:

$$\Delta f = \frac{\Delta\Omega}{2\pi} = \frac{f_s}{N} \quad (10.17)$$

There are two important properties underlying equation 10.16:

1. The series of  $F_k$  is periodic by  $N$ , so that if one considers  $F_{\bar{k}}$  with  $\bar{k} = k + N$ , then one has:

$$F_{\bar{k}} = \frac{1}{N} \sum_{n=0}^{N-1} f_n e^{-i2\pi \bar{k} \frac{n}{N}} = \frac{1}{N} \sum_{n=0}^{N-1} f_n e^{-i2\pi k \frac{n}{N}} e^{-i2\pi N \frac{n}{N}}$$

and if one applies Euler identity, so that  $e^{-i2\pi n} = \cos(2n\pi) - i \sin(2n\pi) = 1$ , then it is clear that  $F_{\bar{k}} = F_k$ , which implies the periodicity of the coefficients of the DFT;

2.  $F_k$  coefficients are symmetric with respect to the first  $N/2$  samples, so that if one wanted to compute the  $F_k$  coefficients from 0 to  $N - 1$  then it's enough to compute the first  $N/2$  and calculate their complex conjugate to calculate the remaining  $N/2$ .

In this work, the DFT will also be referred as FFT (*Fast Fourier Transform*). The main reason being that its numerical implementation follows the algorithm proposed by Cooley & Turkey [54] in 1965. The computational time required for this algorithm to perform the DFT is proportional to  $\frac{N}{2 \log_2 N}$ , making the Fourier transform very fast to be computed.

# References

- [1] T. Sigfrids, *Hot wire and PIV studies of transonic turbulent wall-bounded flows*. PhD thesis, Mekanik, 2003.
- [2] E. Naudascher, *Flow-induced vibrations: an engineering guide*. Routledge, 2017.
- [3] <https://newt.phys.unsw.edu.au/jw/Helmholtz.html>.
- [4] D. Rockwell and E. Naudascher, “Review—Self-Sustaining Oscillations of Flow Past Cavities,” *Journal of Fluids Engineering*, vol. 100, pp. 152–165, 06 1978.
- [5] V. Sarohia, *EXPERIMENTAL AND ANALYTICAL INVESTIGATION OF OSCILLATIONS IN FLOWS OVER CAVITIES*. California Institute of Technology, 1975.
- [6] A. Roshko, “Some measurements of flow in a rectangular cutout,” tech. rep., CALIFORNIA INST. OF TECH PASADENA, 1955.
- [7] P. J. Block, “Noise response of cavities of varying dimensions at subsonic speeds,” tech. rep., NASA Langley Research Center Hampton, VA, United States, 1976.
- [8] H. H. Heller, S. E. Widnall, and W. Jones, “Water-table visualization of flow-induced pressure oscillations in shallow cavities for simulated supersonic flow conditions,” *The Journal of the Acoustical Society of America*, vol. 55, no. 2, pp. 439–439, 1974.
- [9] K. Ahuja and J. Mendoza, “Effects of cavity dimensions, boundary layer, and temperature on cavity noise with emphasis on benchmark data to validate computational aeroacoustic codes,” tech. rep., Georgia Tech Research Inst. Atlanta, GA, United States, 1995.
- [10] M. Barone, B. Qawasmeh, and M. Wei, “Low-dimensional modeling for spatially developing free shear layers,” *47th AIAA Aerospace Sciences Meeting including the New Horizons Forum and Aerospace Exposition*, 01 2009.
- [11] N. Suhs, “Unsteady flow computations for a three-dimensional cavity with and without an acoustic suppression device,” in *11th Applied Aerodynamics Conference*, p. 3402, 1993.
- [12] S. Sadiq and M. I. Sabir, “Cavity acoustics analysis—an extensive comparison of turbulence model coefficients,” in *2011 IEEE Symposium on Underwater Technology and Workshop on Scientific Use of Submarine Cables and Related Technologies*, pp. 1–7, IEEE, 2011.
- [13] M. Mesbah and S. Majidi, “Numerical identification of flow-induced oscillation modes in rectangular cavities using urans,” *Journal of Applied Fluid Mechanics*, vol. 13, no. 2, pp. 703–713, 2020.
- [14] D. N. Liliedahl, F. L. Carpenter, and P. G. Cizmas, “Prediction of aeroacoustic resonance in cavities of hole-pattern stator seals,” *Journal of engineering for gas turbines and power*, vol. 133, no. 2, 2011.
- [15] C. Shieh and P. Morris, “Comparison of two-and three-dimensional turbulent cavity flows,” in *39th aerospace sciences meeting and exhibit*, p. 511, 2001.
- [16] F. Menter, R. Lechner, and A. Matyushenko, “Best practice: generalized k- $\omega$  two-equation turbulence model in ansys cfd (geko),” *ANSYS Germany GmbH*, 2019.

- [17] B.-T. Chu and L. S. Kovásznyai, “Non-linear interactions in a viscous heat-conducting compressible gas,” *Journal of Fluid Mechanics*, vol. 3, pp. 494–514, 1958.
- [18] A. Aleksentsev, A. Sazhenkov, and S. Sukhinin, “Acoustic resonance phenomena in air bleed channels in aviation engines,” *Journal of Applied Mechanics and Technical Physics*, vol. 57, pp. 971–978, 2016.
- [19] <https://www.energy.kth.se/heat-and-power-technology/current-projects/cavity-acoustics-and-rossiter-modes-care-1.928726>.
- [20] A. Srivastava and A. J. Meade, “Application of machine learning techniques for classification of cavity flow and resonance,” *Journal of Aircraft*, vol. 51, no. 5, pp. 1642–1647, 2014.
- [21] K. Zhao, P. Okolo, E. Neri, P. Chen, J. Kennedy, and G. J. Bennett, “Noise reduction technologies for aircraft landing gear—a bibliographic review,” *Progress in Aerospace Sciences*, vol. 112, p. 100589, 2020.
- [22] R. Morita, Y. Uchiyama, F. Inada, and S. Takahashi, “Considerations in steam piping design for prevention of an acoustic resonance at a closed side branch,” in *Pressure Vessels and Piping Conference*, vol. 57977, p. V004T04A031, American Society of Mechanical Engineers, 2017.
- [23] K. Nusser and S. Becker, “Numerical investigation of the fluid structure acoustics interaction on a simplified car model,” *Acta Acustica*, vol. 5, p. 22, 2021.
- [24] S. Hammer, J. Fridh, and M. Billson, “Experimental investigation of rossiter modes for an open box cavity with adjustable depth,” in *Turbo Expo: Power for Land, Sea, and Air*, vol. 84928, p. V02CT35A008, American Society of Mechanical Engineers, 2021.
- [25] X. Gloerfelt, “Cavity noise,” *VKI lecture series*, vol. 3, 2009.
- [26] E. Naudascher, “From flow instability to flow-induced excitation,” *Journal of the Hydraulics Division*, vol. 93, no. 4, pp. 15–40, 1967.
- [27] D. Rockwell, “Oscillations of impinging shear layers,” *AIAA journal*, vol. 21, no. 5, pp. 645–664, 1983.
- [28] D. Rockwell and E. Naudascher, “Review—Self-Sustaining Oscillations of Flow Past Cavities,” *Journal of Fluids Engineering*, vol. 100, no. 2, pp. 152–165, 1978.
- [29] R. Blevins, *Flow-induced Vibration*. Krieger Publishing Company, 2001.
- [30] C. Perrot-Minot, E. Mignot, R. Perkins, D. Lopez, and N. Riviere, “Vortex shedding frequency in open-channel lateral cavity,” *Journal of Fluid Mechanics*, vol. 892, p. A25, 2020.
- [31] J. Rossiter, “Wind-tunnel experiments on the flow over rectangular cavities at subsonic and transonic speeds,” *Ministry of Aviation*, 1964.
- [32] H. Plumblee, J. Gibson, and L. Lassiter, *A theoretical and experimental investigation of the acoustic response of cavities in an aerodynamic flow*, vol. 61. Flight Dynamics Laboratory, Aeronautical Systems Division, Air Force Systems . . . , 1962.
- [33] C. K. Tam and P. J. Block, “On the tones and pressure oscillations induced by flow over rectangular cavities,” *Journal of Fluid Mechanics*, vol. 89, no. 2, pp. 373–399, 1978.
- [34] W. K. Blake, “Mechanics of flow-induced sound and vibration. volume 1 general concepts and elementary source. volume 2-complex flow-structure interactions,” *Aplikace Matematiky, Applied Mathematics*, vol. 1, 1986.
- [35] K. Krishnamurty, “Acoustic radiation from two-dimensional rectangular cutouts in aerodynamic surfaces,” tech. rep., NATIONAL ADVISORY COMMITTEE FOR AERONAUTICS, 1955.

- [36] S. M. Grace, W. G. Dewar, and D. E. Wroblewski, "Experimental investigation of the flow characteristics within a shallow wall cavity for both laminar and turbulent upstream boundary layers," *Experiments in fluids*, vol. 36, pp. 791–804, 2004.
- [37] M. Gharib and A. Roshko, "The effect of flow oscillations on cavity drag," *Journal of Fluid Mechanics*, vol. 177, pp. 501–530, 1987.
- [38] X. Gloerfelt, C. Bailly, and D. Juvé, "Direct computation of the noise radiated by a subsonic cavity flow and application of integral methods," *Journal of sound and vibration*, vol. 266, no. 1, pp. 119–146, 2003.
- [39] S. Lawson and G. Barakos, "Review of numerical simulations for high-speed, turbulent cavity flows," *Progress in Aerospace Sciences*, vol. 47, no. 3, pp. 186–216, 2011.
- [40] S. Arunajatesan and N. Sinha, "Hybrid rans-les modeling for cavity aeroacoustics predictions," *International Journal of Aeroacoustics*, vol. 2, no. 1, pp. 65–93, 2003.
- [41] L. Davidson, "Fluid mechanics, turbulent flow and turbulence modeling," 2015. Lecture Notes from Chalmers.
- [42] L. Davidson, "An introduction to turbulence models," 2022. Lecture Notes from Chalmers.
- [43] F. Menter, R. Lechner, and A. Matyushenko, "Best practice: Rans turbulence modeling in ansys cfd," *ANSYS Inc.: Canonsburg, PA, USA*, 2021.
- [44] F. R. Menter, "Best practice: scale-resolving simulations in ansys cfd," *ANSYS Germany GmbH*, vol. 1, 2012.
- [45] F. Menter and M. Kuntz, "Development and application of a zonal des turbulence model for cfx-5, ansys, cfx-validation report," *Technical report*, 2003.
- [46] C. Ansys *et al.*, "Theory guide," *Ansys Inc*, 2021.
- [47] B.-T. Chu and L. S. Kovásznyai, "Non-linear interactions in a viscous heat-conducting compressible gas," *Journal of Fluid Mechanics*, vol. 3, no. 5, pp. 494–514, 1958.
- [48] H. Schlichting and K. Gersten, *Boundary-layer theory*. springer, 2016.
- [49] D. Vogt, *Experimental investigation of three-dimensional mechanisms in low-pressure turbine flutter*. PhD thesis, KTH Royal Institute of Technology, 2005.
- [50] E. Brundrett and W. Baines, "The production and diffusion of vorticity in duct flow," *Journal of Fluid Mechanics*, vol. 19, no. 3, pp. 375–394, 1964.
- [51] G. Mompean, "Numerical simulation of a turbulent flow near a right-angled corner using the speciale non-linear model with rng  $k-\varepsilon$  equations," *Computers & Fluids*, vol. 27, no. 7, pp. 847–859, 1998.
- [52] C. Lucio, "Design of a high subsonic nozzle for a transonic linear cascade operating at near stall conditions," 2021.
- [53] A. Fasana and S. Marchesiello, *Meccanica delle Vibrazioni*. CLUT Editrice, 2006.
- [54] J. W. Cooley and J. W. Tukey, "An algorithm for the machine calculation of complex fourier series," *Mathematics of computation*, vol. 19, no. 90, pp. 297–301, 1965.